State-Insensitive Traps for Caesium Atoms

Piyaphat Phoonthong

A thesis submitted to the University College London
in partial fulfilment of the requirements for the
degree of Doctor of Philosophy

Department of Physics and Astronomy
University College London
February 2012

I, Piyaphat Phoonthong, confirm that the work presented in this thesis is my own. Where information has been derived from other sources, I confirm that this has been indicated in the thesis.

Signed ..... Date .....

Abstract

State-insensitive traps are an important tool for precision spectroscopy. In these traps both the ground and excited state of the relevant atomic transition are shifted by the same amount. To obtain state-insensitive trapping, a specific trapping wavelength - called the "magic wavelength" - must be used. This thesis describes state-insensitive trapping of caesium atoms, as realised by using a trapping laser beam at the magic wavelength of 935.6 nm. Two different experimental setups were realised and characterised.

The first set of experiments provided the characterisation of a single-well state-insensitive trap, produced by using the laser beam from a Ti-sapphire laser. The trap lifetime was determined as a function of the trap depth, with the largest lifetime of 203 ms measured for a trap depth of 2.4 mK. Further improvement in the trap lifetime was obtained by applying a depumper laser beam, which prepared the atoms in the lower ground state. This suppresses hyperfine changing collisions, and the lifetime was increased to 3.6 s as a result. Ultimately, the lifetime was limited by the pointing instability of the dipole trap beam and the background gas collisions.

A second experimental setup was then realised, to reduce the background gas collisions, which is the limitation of lifetime in the first setup. Furthermore, the imaging system was upgraded to reduce the background noise, and a MOPA system was used to produce the state-insensitive trap. In a second set of experiments, a single-well trap and a 1D optical lattice were compared to evaluate the suppression of two-body collisions in the 1D lattice case.

To my family

Acknowledgements

The past four and a half years have been the most important years of my life. I would like to take this opportunity to express my gratitude to all those who supported and inspired me through out my PhD.

First of all, I would like to acknowledge my supervisor Prof. Ferruccio Renzoni. I have been very fortunate to work in his group where I had the opportunity to learn about laser cooling and trapping. He was always able to give me suggestions and motivation when I encountered problems with my experiment.

Next, I would like to thank Peter Douglas for teaching me the basic knowledge about the experiment. During my first year, I shared the office with Martin Brown, Vyacheslav Lebedev, Lyubomir Petrov and Arne Wickenbrock. Later, Nihal Abdul Wahab, Mukaddes Meliz Metbulut, Philip Christoph Holz, Yuval Rubin, Michal Hemmerling, Soliman Edris and Cosimo Lovecchio joined our group. These people have been great to work with, and also to enjoy a beer after work. I would like to give a special thanks to Arne Wickenbrock for proof reading my thesis, for many useful discussions about my experiment, and even for providing an invitation letter for the Schengen visa application.

A complex experiment requires a lot of mechanical and electronic components, so I thank Rafid Jawad for building a lot of the equipment and helping me solve some electronics problems. I thank also John Dumper for building some mechanical parts for the experiment.

Outside UCL, I also have to thank all members of the Thai society: Supattra Boonyawatana, Kanockul Manathanya, Kobpong Khomson, Rujaya Palattanavit, Suphannada Limpanonda, Piangor Pattayakorn, Thuttai Keeratipongpaiboon, Arnunchanog Sakondhavat and Kampree Sethaputra for sharing a great time in the United Kingdom. Thanks to Varomyalin Tipmanee for being a good flat-mate and Pruet Kalasuwan

from Bristol for useful discussions about quantum computers.

For financial support, I would like to thank the Royal Thai Government and the National Institute of Metrology Thailand for a scholarship. Thanks to all the staff at the office of educational affairs for supporting all the documents I need.

On a more personal note, I would like to thank my parents Vichai and Sumana Phoonthong, and also my brother Natthapol Phoonthong for their love and encouragement through the 28 years of my life. Last but not least, I would especially like to thank my girlfriend Anongrat Kaewbamrung for standing by me when I feel discouraged and downhearted.

Contents

List of Figures

List of Tables

Chapter 1

Introduction

Over the last three decades, laser cooling and trapping has opened up several new fields of research in atomic physics. The interaction of light and matter can be divided into two parts: the radiation pressure and the dipole force. While radiation pressure forms the basis of most cooling schemes, the dipole force can provide a trapping potential. This thesis documents the construction of the apparatus and the experiments with caesium atoms in a state-insensitive dipole trap.

Laser cooling

In 1975, Hänsch and Schawlow [1], and Wineland and Dehmelt [2] gave the earliest idea for laser cooling by using radiative forces to reduce the thermal velocity of atoms. This force is related to the momentum transfer in spontaneous emission known as Doppler cooling. Three years later, the first laser cooling experiments were realised with charged particles by two groups: Wineland et al. reported the cooling of a magnesium ion in a Penning trap [3], and Neuhauser et al. cooling a barium ion [4]. For neutral atoms, optical molasses, which uses radiation pressure of counterpropagating laser beams to slow down atoms, was demonstrated in 1985 [5]. A breakthrough of laser cooling was the invention of the "*Magneto-Optical Trap*"(MOT) in 1987. It provides both cooling and confinement by a velocity and position dependent photon scattering rate [6]. Currently, MOTs are the first step to prepare high density samples of cold atoms for research in atomic physics.

Optical traps

Even before the advent of laser cooling, Letokov proposed a scheme for using laser light in order to trap particles in 1968 [7], which makes use of the dipole force experienced by an atom in an oscillating electric field [8]. The interaction between the dipole moment of an atom and the light field causes an energy shift called the AC Stark shift or light shift. In contrast to the scattering force, which acts in the same direction as the laser beam, the dipole force is generated in the direction of the gradient of the laser intensity. In 1986, the first optical trap was achieved with sodium atoms by loading the atoms from an optical molasses into a tightly focussed near resonance laser beam [9]. Later in 1993 after the development of the MOT, the first result with a far off resonance trap (FORT) was published [10]. This optical trap had a large red detuning of around 65 nm from the atomic resonance and achieved a lifetime of about 200 ms. The results in [10] show that a larger detuning can increase the lifetime of the trap as it is inversely proportional to the scattering rate. In addition, spontaneous photon scattering leads to heating in the trap and causes decoherence of the atomic sample.

Nowadays, optical traps are widely used in many areas of research, for example in Bose Einstein Condensation [11], precision spectroscopy [12–14] and trapping and manipulating single atoms [15–18].

State-insensitive Traps

In general, different atomic energy levels experience different light shifts. The corresponding transition frequencies are therefore altered in the presence of an oscillating electric field. A state-insensitive trap is an optical trap where the two states of a given transition are equally shifted. The transition frequency is therefore the same as in free space. The specific wavelength of the trapping beam required to achieve state-insensitive trapping is called the *Magic Wavelength*, which can be calculated from the AC Stark shift for a multi-level atom. This kind of trap was first proposed for a Sr optical clock by Hidotoshi Katori in 1999 [19].

One advantage of the AC Stark shift cancellation is a reduction in measurement uncertainty for high precision spectroscopy and in frequency standards. Over the last decade, the magic wavelength for several atoms has been calculated and experimentally verified as shown in table 1.1.

Atom	λ_m (nm)	Transition	Ref.
Sr	813.428(1)	${}^1S_0 \rightarrow {}^3P_0$	[20–22]
Yb	759.35(2)	${}^1S_0 \rightarrow {}^3P_0$	[22, 23]
Hg	362.5(3)	${}^1S_0 \rightarrow {}^3P_0$	[22, 24]
Mg	470(10)	${}^1S_0 \rightarrow {}^3P_0$	[22, 25]
Rb	811.5	$5S_{1/2}$ (Microwave transition)	[26]
Cs	935(4)	$6S_{1/2} \rightarrow 6P_{3/2}$	[27, 28]

Table 1.1: List of the atomic magic wavelengths (λ_m) which were calculated and experimentally verified.

The strontium, ytterbium, mercury and magnesium atoms are of interest as the application of frequency standards. In addition, the state-insensitive trap is of benefit to electromagnetically induced transparency (EIT). EIT is a phenomenon in a three level system that reduces the absorption of a medium. It can be described as an optical pumping into a coherent superposition of two ground states when two coherent laser sources are tuned to a common excited state [29, 30]. The linewidth of EIT features can be extremely narrow, and is therefore useful in metrology. However, various effects can broaden the spectral linewidth, for example: collisional broadening, stray magnetic fields and lack of interrogation time.

In [31], the linewidth reduction by increased interrogation time was experimentally realised with different pulse lengths of the probe beam. The narrowest linewidth of 4 kHz was measured with a 100 μs pulse while atoms were held in a CO_2 dipole trap. The state-insensitive trap can provide long interrogation time without the differential energy shift, which can increase the linewidth of the EIT feature. Finally, in an optical lattice with an average site occupation below one, collisional broadening can be ignored.

Thesis overview

In chapter 2, I describe the theoretical concepts of laser cooling and trapping underlying our experiment, and also the AC Stark shift calculation to determine the wavelength required for a state-insensitive trap. Chapter 3 presents a description of the design and setup of my experiment including the laser system, the optical phase-locked loop, the vacuum system and the imaging system. The state-insensitive trap is characterised in chapter 4 where the relevant loss mechanisms are investigated. Chapter 5 shows how the experiment can be upgraded to increase the lifetime in the dipole trap. The loss mechanisms of a single focussed beam and a 1D optical lattice dipole trap are investigated and compared. Finally, in chapter 6, conclusions are presented together with an outlook for future research.

Chapter 2

Laser cooling and trapping

The interaction of light and atoms produces a force leading to the cooling and trapping of atoms. There are two important forces playing a role: the scattering force and the dipole force. Generally, the thermal velocity of atoms can be reduced by the scattering force. On the other hand, confinement of atoms can be provided by the dipole force.

In this chapter, I start with a description of laser cooling caused by a velocity dependent force, and follow on by introducing the theoretical concepts of the Magneto-Optical Trap. After that, I describe an atom in an electric field following the Lorentz approach, and then introduce the time-dependent perturbation theory for an oscillating electric field (AC Stark effect). Then I present the derivation of the light shift caused by the AC Stark effect for a two-level, and then for a multi-level system. Finally, I present numerical results for specific features of our optical dipole trap, namely the trap depth and the trap frequency.

2.1 Laser cooling

The essential element of laser cooling is the momentum transfer between atom and photon. When an atom absorbs a photon from a laser, it acquires a momentum $\hbar k$ in the direction of the beam [8, 32]. Instead, for spontaneous emission, the momentum kick will be in a random direction. Over many cycles, the momentum gained during spontaneous emission averages to zero, while the momentum kicks in the direction of the laser beam add up. The result of this momentum transfer is a force

called the *scattering force, or radiation pressure force.* It is written as

$$< F_{sc} >= \hbar k \Gamma_{sc}, \tag{2.1}$$

where Γ_{sc} is the rate of photon scattering per second and $\hbar k$ is the momentum of each photon. In a two-level system, the scattering rate depends on the decay rate, or the natural linewidth of the excited state (Γ) [33]. The scattering rate is then given by:

$$\Gamma_{sc} = \frac{\Gamma}{2} \frac{\frac{I}{I_{sat}}}{1 + \frac{I}{I_{sat}} + 4\left(\frac{\Delta}{\Gamma}\right)^2}, \tag{2.2}$$

where Δ is the laser detuning from the atomic resonance, I is the laser intensity, and I_{sat} is the saturation intensity.

The scattering force is a velocity dependent force, so atoms with different momenta experience different detunings due to the Doppler effect [34]. The force on an atom moving with velocity v towards or away from laser beam is

$$F_{sc} = \hbar k \frac{\Gamma}{2} \frac{\frac{I}{I_{sat}}}{1 + \frac{I}{I_{sat}} + 4\left(\frac{(\omega_L - \omega_0 - kv)}{\Gamma}\right)^2}. \tag{2.3}$$

where ω_L is the laser frequency, ω_0 is the transition frequency, and kv is the frequency shift due to the Doppler effect. This force also depends on the intensity of the laser beam and saturates at $\hbar k \frac{\Gamma}{2}$ for high intensities ($I >> I_{sat}$).

To cool atoms, laser beams from all six spatial directions are applied. This technique is called optical molasses. It can be explained in one dimension with two counter-propagating laser beams as follows. If both beams are red-detuned and the atom is moving towards one of them, it will experience this beam with a higher frequency (blue-shifted) and the other beam with a lower frequency (red-shifted) [34]. The total force on the atom becomes [8]:

$$F_{molasses} = F_{sc}(\omega_L - \omega_0 - kv) - F_{sc}(\omega_L - \omega_0 + kv). \tag{2.4}$$

The optical molasses can be applied to further reduce the temperature of the atomic cloud. The atom can reach the low velocities regime ($kv << \Gamma$) which the force can be simplified to:

$$F_{molasses} \approx 8\hbar k^2 \frac{I}{I_{sat}} \left(\frac{\Delta}{\Gamma \left(1 + \frac{I}{I_{sat}} + 4(\frac{\Delta}{\Gamma})^2\right)^2} \right) v \equiv -\alpha v. \tag{2.5}$$

This force can be understood as a friction force which is proportional to the velocity of the atom. The sign of the force is determined by the detuning of the laser beam ($\Delta = \omega_L - \omega_0$).

To derive a final temperature, heating and cooling rates are compared. In thermal equilibrium, the heating rate due to the random recoil kick of spontaneous emission equals the cooling rate of the friction force in equation (2.5). The temperature in the steady state is then written as:

$$k_B T = \frac{\hbar\Gamma}{4} \left[\frac{1 + \frac{I}{I_{sat}} + 4\left(\frac{\Delta}{\Gamma}\right)^2}{2\frac{\Delta}{\Gamma}} \right]. \tag{2.6}$$

In the limit of low intensity ($\frac{I}{I_{sat}} << 1$) and a detuning of $\Delta = -\frac{\Gamma}{2}$, the lowest temperature obtainable by the optical molasses is then called the Doppler cooling limit [8, 32, 34].

$$T_D \approx \frac{\hbar\Gamma}{2k_B}. \tag{2.7}$$

From equation (2.7), the temperature limit only depends on the decay rate (Γ). In the case of caesium atoms, the decay rate is $\Gamma = (2\pi)5.22$ MHz which then limits the temperature to $\mathrm{T}_D = 125\ \mu$K [35]. We notice that although the force can slow down atoms to micro-Kelvin temperatures, it cannot confine the atoms, as the force is velocity dependent but not position dependent [34].

2.2 Magneto-optical trap

The magneto-optical trap (MOT) is the most widely used and robust trap for preparing cold atoms. The simplest model to explain the MOT is a one dimensional configuration for a two-level atom with a F = 0 → F′ = 1 transition.

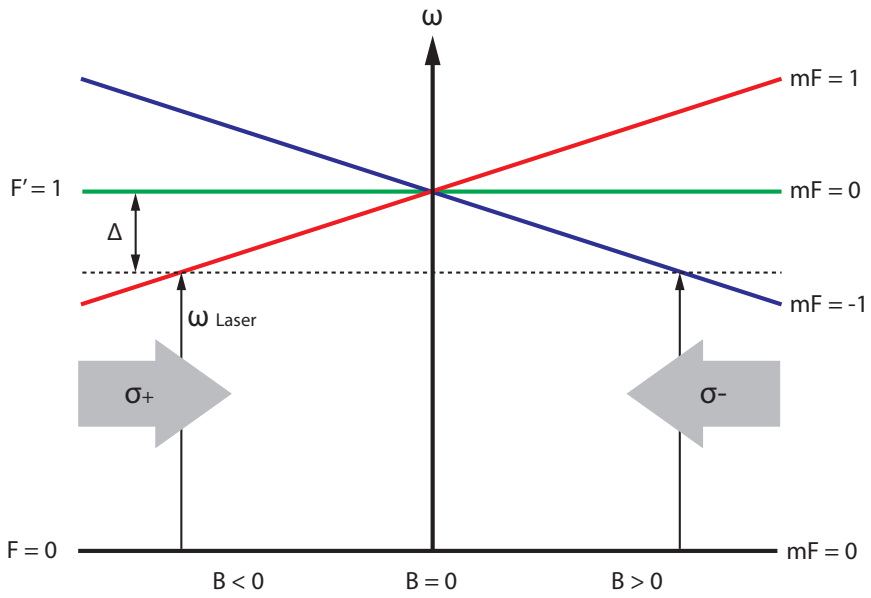

Figure 2.1: Simple model of the MOT for a two-level atom with a F = 0 → F′ = 1 transition. The laser frequency is red-detuned with respect to the atomic transition by Δ. The inhomogeneous magnetic field causes the Zeeman shift of the magnetic sublevels to depend on the position of the atoms.

Two counter-propagating laser beams with opposite circular polarisation are red-detuned from the atomic transition. A pair of coils in the anti-Helmholtz configuration supplies a magnetic field gradient. This gradient causes the Zeeman splitting of the excited state (F′ = 1) into three magnetic sublevels. This splitting depends on the position of the atoms, causing a position dependent force [8, 32].

From figure 2.1, if an atom is located to the right with respect to the zero magnetic field position, the Zeeman splitting shifts the transition F = 0 → F′ = 1 , m = -1 to be closer to the laser frequency. Consequently, the σ^- light which can only excite to the transition Δm = -1, pushes an atom positioned on the right towards the centre. The total force in a

MOT can be described as a position and velocity dependent force [7, 8]:

$$F_{MOT} = -\alpha v - \frac{\alpha\beta}{k} r, \tag{2.8}$$

where α is the damping coefficient from equation (2.5), β is the Zeeman shift and $\frac{\alpha\beta}{k}$ is the spring constant.

In a real experiment, three pairs of orthogonal laser beams are applied to confine the atoms in three-dimensions. For an alkali atom, the cycling transition is ideally from the upper ground state ($nS_{1/2}$) to the highest excited state ($nP_{3/2}$) [34]. However, off-resonance excitation can lead to a loss of the population into levels not excited by the lasers, and an additional beam (repumper laser) is required to pump atoms back into the cycling transition.

2.3 Dipole trap

Two forces should be considered to understand the working principle of a dipole trap: the scattering force and the dipole force [8, 36]. The scattering force on the atoms leads to the heating of the atoms in the dipole trap. Normally, this force can be neglected when the light field is far detuned from an atomic resonance as $F_{scatt} \propto \frac{I}{\Delta^2}$ [8, 37]. On the other hand, an electric dipole moment in an atom can be induced by the light field, which can shift the atomic energy level. This shift is called the AC Stark shift and is proportional to the light intensity, and inversely proportional to the detuning: $U_{dipole} \propto \frac{I}{\Delta}$. The dipole force can then be described as the gradient of the energy shift [37]. So a strongly focussed beam is necessary to produce the dipole force to confine atoms in the trap. Due to the dependence of the sign of the dipole force on the detuning of the light field (Δ), optical dipole traps can be classified by the sign of the detuning: red-detuned and blue-detuned traps. The atoms in a red-detuned trap are attracted to the maximum intensity while the atoms in a blue-detuned trap are expelled from the high intensity region.

2.3.1 Two-level atom

An electric field $\vec{E}$ induces an electric dipole moment of $-e\hat{r} = \alpha_0\vec{E}$ in an atom with polarisability α_0. To define the polarisability of a particle, we start with a classical picture: consider a Lorentz-atom which consists of an electron elastically bound to a nucleus with a frequency ω_0. The atom experiences the electric field, and the dynamics can be classically modelled by a driven damped harmonic oscillator [38]. The equation of motion of the Lorentz-atom is given by

$$\ddot{x} + \Gamma_\omega \dot{x} + \omega_0^2 x = -\frac{eE}{m_e}, \tag{2.9}$$

where $\Gamma_\omega = \frac{e^2\omega^2}{6\pi\epsilon_0 m_e c^3}$ [37] is the damping rate due to the dipole radiation emitted by the accelerated electron. The oscillating electric field and the displacement of the electron can be written as

$$E(t) = E_0 e^{-i\omega t} \tag{2.10}$$

$$x(t) = x_0 e^{-i\omega t}. \tag{2.11}$$

By substituting equations (2.10) and (2.11) into the equation of motion (2.9), we obtain

$$x(t) = -\frac{eE(t)}{m_e}\frac{1}{\omega_0^2 - \omega^2 - i\omega\Gamma_\omega}. \tag{2.12}$$

The oscillatory motion will produce an oscillating electric dipole moment. The resulting complex polarisability is:

$$\alpha_0 = 6\pi\epsilon_0 c^3 \frac{\Gamma/\omega_0^2}{\omega_0^2 - \omega^2 - i(\omega^3/\omega_0^2)\Gamma}, \tag{2.13}$$

where Γ is the spontaneous decay rate of the excited state, or the damping rate at resonance ($\Gamma = \left(\frac{\omega_0}{\omega}\right)^2 \Gamma_\omega$). From equation (2.13), the polarisability has two parts [37, 39]: the real part describes the dipole interaction which leads to the potential or the energy shift, and the imaginary part, i.e. the out of phase component of the oscillation, leads to the absorption of driving energy which determines the scattering force.

The interaction energy with the electric field due to the frequency dependent polarisability can be written as

$$U = -\frac{1}{2} Re(\alpha_0) \left|E\right|^2, \tag{2.14}$$

where U is the potential of the dipole trap. By substituting the real part of equation (2.13) and the field intensity $I = \frac{\epsilon_0 c}{2} \left|E\right|^2$, the energy shift becomes

$$U_{dipole}(r) = -\frac{3\pi c^2}{\omega_0^2} \left(\frac{\Gamma}{\omega_0^2 - \omega^2}\right) I(r) \tag{2.15}$$

$$U_{dipole}(r) = -\frac{3\pi c^2}{2\omega_0^3} \left(\frac{\Gamma}{\omega_0 - \omega} + \frac{\Gamma}{\omega_0 + \omega}\right) I(r). \tag{2.16}$$

The force on an atom is the gradient of the potential energy which is proportional to the real part of the polarisability (the in-phase component of the dipole oscillation):

$$F_{dipole} = -\nabla U_{dipole}(r) = \frac{1}{2\epsilon_0 c} Re(\alpha_0) \nabla I(r). \tag{2.17}$$

The imaginary part of the polarisability can cause the absorption of energy which is re-emitted as dipole radiation from the atom. The emission can also be considered as photon scattering by the atom with a rate

$$\Gamma_{sc} = \frac{1}{2\hbar} Im(\alpha_0) \left|E\right|^2. \tag{2.18}$$

Then, by replacing equation (2.18) with the imaginary part of the polarisability from equation (2.13), we obtain

$$\Gamma_{sc}(r) = \frac{3\pi c^2 \omega^3}{\hbar \omega_0^4} \left(\frac{\Gamma}{\omega_0^2 - \omega^2}\right)^2 I(r) \tag{2.19}$$

$$\Gamma_{sc}(r) = \frac{3\pi c^2}{2\hbar\omega_0^3} \left(\frac{\omega}{\omega_0}\right)^3 \left(\frac{\Gamma}{\omega_0 - \omega} + \frac{\Gamma}{\omega_0 + \omega}\right)^2 I(r). \tag{2.20}$$

For a detuning $\Delta \equiv \omega - \omega_0 << \omega_0$ and $\omega/\omega_0 \approx 1$, we can apply the rotating wave approximation to simplify the equation (2.16) and (2.20). The potential depth and the scattering rate of the two-level dipole trap

are given by

$$U_{dipole}(r) = \frac{3\pi c^2}{2\omega_0^3}\frac{\Gamma}{\Delta}I(r) \tag{2.21}$$

$$\Gamma_{sc}(r) = \frac{3\pi c^2}{2\hbar\omega_0^3}\left(\frac{\Gamma}{\Delta}\right)^2 I(r). \tag{2.22}$$

The behaviour of a two-level atom in a dipole trap can be explained on the basis of these two equations. A simple relation between the photon scattering rate and the potential depth is written as

$$\hbar\Gamma_{sc}(r) = \frac{\Gamma}{\Delta}U_{dipole}(r). \tag{2.23}$$

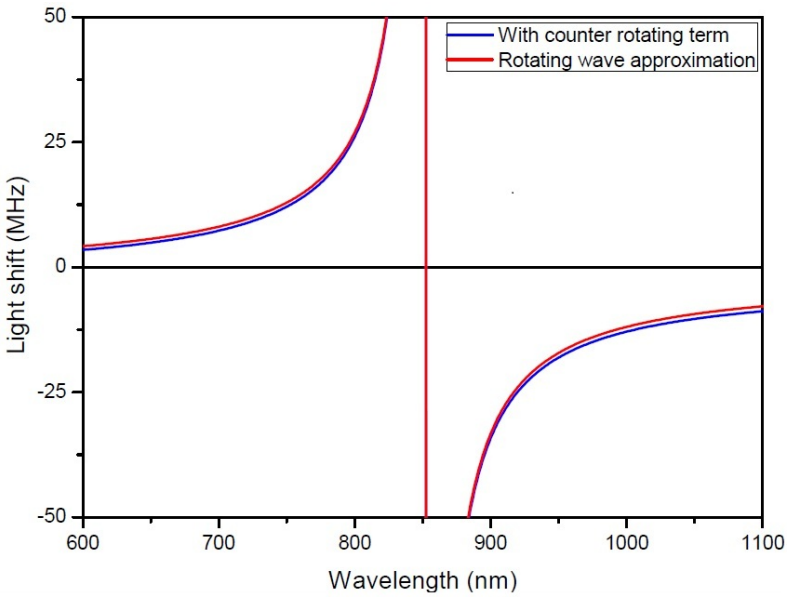

Figure 2.2: AC Stark shift of a two-level atoms vs. wavelength of the laser field. Results of a full calculation which includes the counter-rotating terms (blue line) are compared to those obtained with the rotating wave approximation (red line). Parameter of the calculation is $I_0 = 3 \times 10^9$ W/cm^2.

Figure 2.2 shows the AC Stark shift for different trap wavelengths. As we can see, the sign of the light shift changes when the trap wavelength changes from red-detuned to blue-detuned with respect to the atomic transition. The plot also illustrates the validity of the rotating wave approximation for the far-off resonance trap.

2.3.2 Multi-level atom

For a multi-level atom, the dipole potential for each individual level can be determined by taking into account the couplings to all possible levels, weighted by the appropriate transition strengths. The transition strength can be expressed in term of the *Clebsch-Gordan coefficient* (C_{ij}) [37, 39] between an initial state i and a final state j. The total energy shift for the n-level atom is obtained by summing the contributions of all possible transitions.

$$U_{dipole}(r) = \frac{3\pi c^2 \Gamma}{2} I \times \sum_n \frac{C_{ij}^2}{\omega_{ij}^3 \Delta_{ij}}. \tag{2.24}$$

In the case of an alkali with the ground state $S_{1/2}$ and the excited state $P_{1/2}$ (D_1 line) and $P_{3/2}$ (D_2 line), the total ground state energy shift can be written as [37]

$$U_{dipole}(r) = \frac{\pi c^2 \Gamma}{2} \left(\frac{2 + \epsilon g_F m_F}{\omega_{3/2}^3 \Delta_{3/2}} + \frac{1 - \epsilon g_F m_F}{\omega_{1/2}^3 \Delta_{1/2}} \right) I(r), \tag{2.25}$$

where ϵ is the polarisation of the dipole trap beam: $\epsilon = 0$ for linear polarisation (π) and $\epsilon = \pm 1$ for circular polarisation ($\sigma^{\pm}$).

Furthermore, the AC Stark shift for a multi-level atom can be calculated from the Hamiltonian of an atom in an oscillating electric field [40, 41]. The energy shift for the multi-level system can be written as the summation of the AC Stark shifts for all the possible atomic transitions [42]:

$$U_{dipole} = \frac{E(r)^2}{4\hbar} \sum \frac{\left| \langle JIFm | \, \hat{d} \, | J'I'F'm' \rangle \right|^2}{\Delta_e}, \tag{2.26}$$

where $E(r)$ is the amplitude of the dipole trap beam, $\frac{1}{\Delta_e} = \frac{1}{\omega_0 - \omega_L} + \frac{1}{\omega_0 + \omega_L}$ is an effective detuning, and $|JIFm\rangle$, $|J'I'F'm'\rangle$ are the initial and final states respectively.

To calculate the energy shift with equation (2.26), we need to reduce the dipole matrix elements by using the Wigner-Eckart theorem [35]. It describes the selection rules between m levels with the 3-J symbol, and the coupling probability between F states with the 6-J symbol. First of all, the 3-J symbol is applied to reduce the non-coupling m states due to the selection rules. This depends on the polarisation of the light

field: $\epsilon = \pm 1$ for $\sigma^{\pm}$-polarisation and $\epsilon = 0$ for π - polarisation, and the selection rule is $m' = m + \epsilon$ [35]:

$$\left|\langle JIFm|\,\hat{d}\,|J'IF'm'\rangle\right|^2 = (2F+1)\begin{pmatrix} F' & 1 & F \\ m' & \epsilon & -m \end{pmatrix}^2 |\langle JIF|\,d\,|J'IF'\rangle|^2 \tag{2.27}$$

To reduce the F and I dependence, the 6-J symbol is introduced as

$$|\langle JIF|\,d\,|J'IF'\rangle|^2 = (2J+1)(2F'+1)\begin{Bmatrix} J & J' & 1 \\ F' & F & I \end{Bmatrix}^2 \left|\langle J|\,\hat{d}\,|J'\rangle\right|^2. \tag{2.28}$$

The remaining dipole matrix elements are expressed as a function of the partial lifetime τ for the transition $J \to J'$ [35]:

$$\frac{1}{\tau} = \frac{\omega_0^3}{3\pi\epsilon_0\hbar c^3}\frac{2J+1}{2J'+1}\left|\langle J|\,\hat{d}\,|J'\rangle\right|^2 \tag{2.29}$$

By putting together equations (2.27), (2.28), (2.29) and substituting to equation (2.26), we can calculate the AC Stark shift of a multi-level atom:

$$U_{dipole} = -\frac{3\pi c^2}{2} I(2F+1) \sum_{J',F',m'} \frac{1}{\omega_0^3 \Delta_e \tau} (2F'+1)(2J'+1)\begin{pmatrix} F' & 1 & F \\ m' & \epsilon & -m \end{pmatrix}^2 \begin{Bmatrix} J & J' & 1 \\ F' & F & I \end{Bmatrix}^2. \tag{2.30}$$

Light shift for the ground state ($6S_{1/2}$)

The electric dipole transitions for the fine structure level of the ground state $6S_{1/2}$ obey a selection rule of the angular momentum $\Delta l = \pm 1$ [8]. Due to that rule, an electron in the ground state $6S_{1/2}$ can be coupled to the excited state nP which has $\Delta l = 1$. The calculation of the Stark shift thus uses table 2.1 for the partial lifetime parameter to obtain the energy shift of the ground state.

The light shift calculation in graph 2.3 compares the results for a simple model (equation (2.25) for only 6P state, blue line) to the results obtained for a multi-level model (equation (2.30) for the 6P - 11P state, red line). The two vertical lines correspond to the caesium D_1 line (894

Level	$\lambda_{1/2}(nm)$	$\tau_{1/2}(\mu s)$	$\lambda_{3/2}(nm)$	$\tau_{3/2}(\mu s)$
6P	894.6	0.03494	852.4	0.03051
7P	459.3	1.308	455.5	0.5787
8P	388.9	10.17	387.6	2.542
9P	361.7	45.94	361.2	6.852
10P	348.0	153.1	347.7	14.35
11P	340.0	418.0	339.8	25.70

Table 2.1: The partial lifetime (τ) and the wavelength of the transition $6S_{1/2} \rightarrow nP_J$ [43, 44].

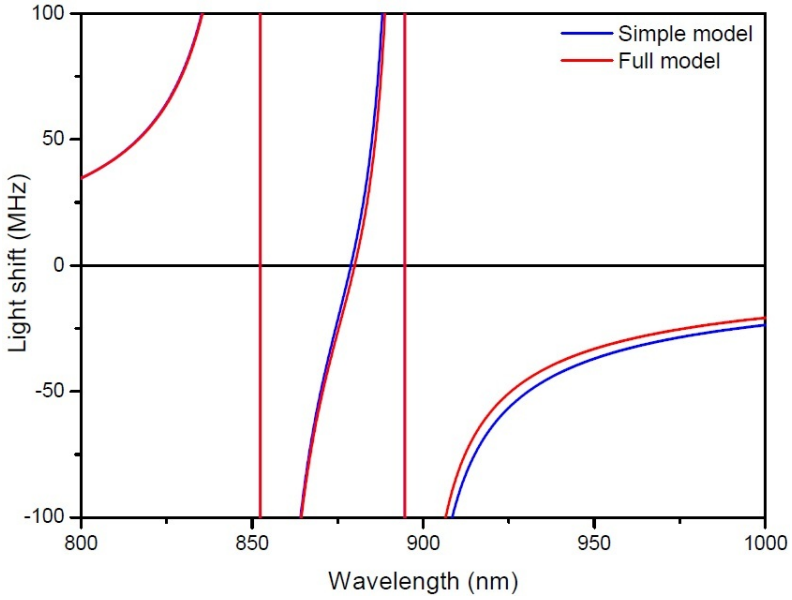

Figure 2.3: The numerically calculated light shift of the ground state of Cs for a linearly polarised trapping beam with an intensity of $I_0 = 3.0 \times 10^9$ W/m^2. The blue line represents the results for the simple model and the red line is the energy shift for full model.

nm) and the D_2 line (852 nm). As can be seen from graph 2.3, the results of the simple model and the full model differ by about 10% at the wavelength of 935.6 nm. The approximation of the simple model becomes closer to the full model at longer wavelengths. On the other hand, the simple model cannot be used for calculating the energy shift for the wavelength below 500 nm due to the effects of the 7P - 11P transitions which are quite significant.

Light shift for the excited state ($6P_{3/2}$)

As discussed previously, the light shift of the ground state is dominated by the coupling to the P-levels. On the other hand, the shifts of the excited state depends on the contributions of the S-levels and D-levels. We start the calculation by noticing that, due to the electric dipole selection rule $\Delta l = \pm 1$ [8], the excited state $6P_{3/2}$ ($l = 1$) can be coupled to both the S-states ($l = 0$) and D-states ($l = 2$). The partial lifetime (τ) used for calculating the AC Stark shift is illustrated in table 2.2 and 2.3.

Level	$\lambda_{1/2}(nm)$	$\tau_{1/2}(\mu s)$
7S	1469.5	0.07529
8S	794.4	0.2599
9S	658.8	0.5533
10S	603.4	0.9924
11S	574.6	1.607
12S	557.3	2.428
13S	546.3	3.490
14S	538.5	4.809
15S	532.9	6.431

Table 2.2: The partial lifetime (τ) and the wavelength of the transition $6P_{3/2} \rightarrow nS_{1/2}$ [43, 44].

Level	$\lambda_{3/2}(nm)$	$\tau_{3/2}(\mu s)$	$\lambda_{5/2}(nm)$	$\tau_{5/2}(\mu s)$
5D	3612.7	10.090	3489.2	1.433
6D	921.1	0.3466	917.2	0.0587
7D	698.3	709.7	697.3	0.1198
8D	621.7	1.284	621.3	0.2170
9D	584.7	2.131	584.5	0.3587
10D	563.7	3.290	563.5	0.5527
11D	550.4	4.807	550.3	0.8063

Table 2.3: The partial lifetime (τ) and the wavelength of the transition $6P_{3/2} \rightarrow nD_J$ [43, 44].

In figure 2.4 and 2.5, the light shift of the excited state $F_e = 3$ and $F_e = 4$ level has been computed by using equation (2.30) for the dipole trap beam with linear polarisation ($\epsilon = 0$).

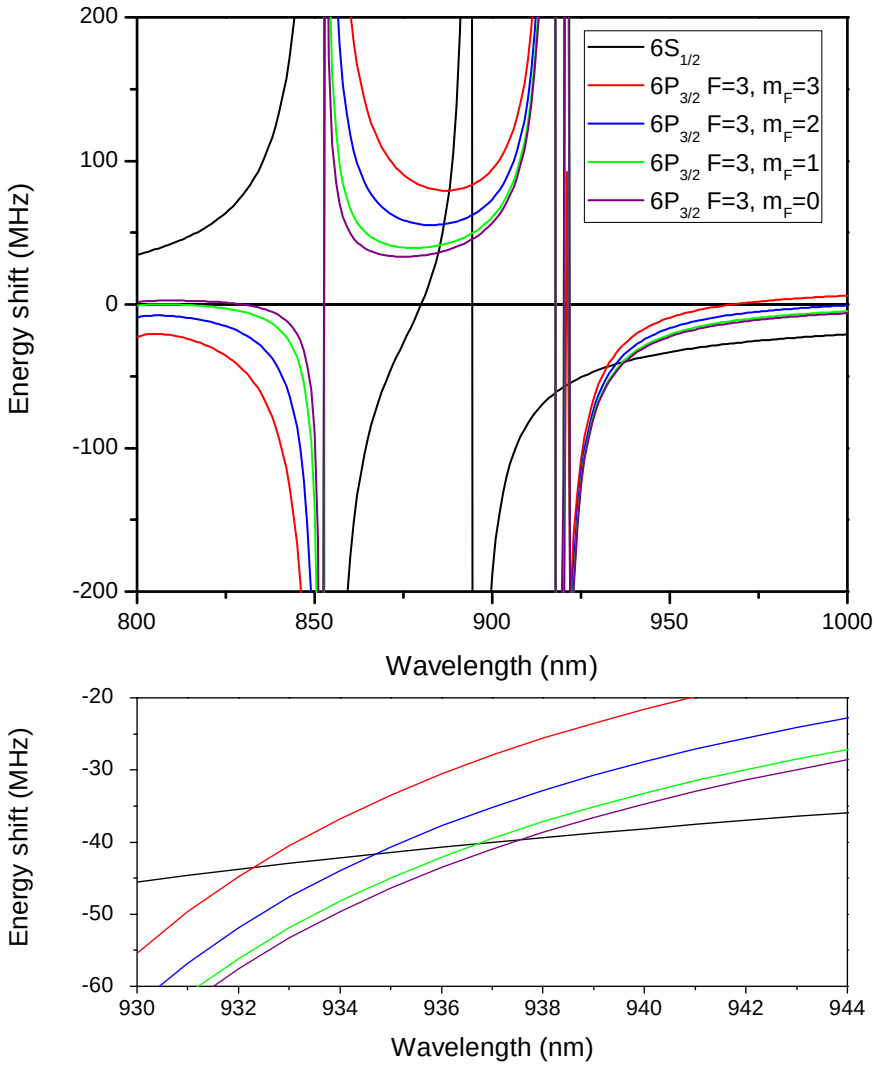

Figure 2.4: (Top) Numerically calculated AC Stark shift of the ground and excited states of Cs for linear polarisation at an intensity of $I_0 = 3.0 \times 10^9$ W/m^2. (Bottom) Magnification of the top graph between 930 nm and 944 nm. All sublevels of the ground state experience the same shift but the excited state levels ($F_e = 3$) are split. The crossing points of each line indicates the magic wavelength for each sublevel, which is around 935 nm.

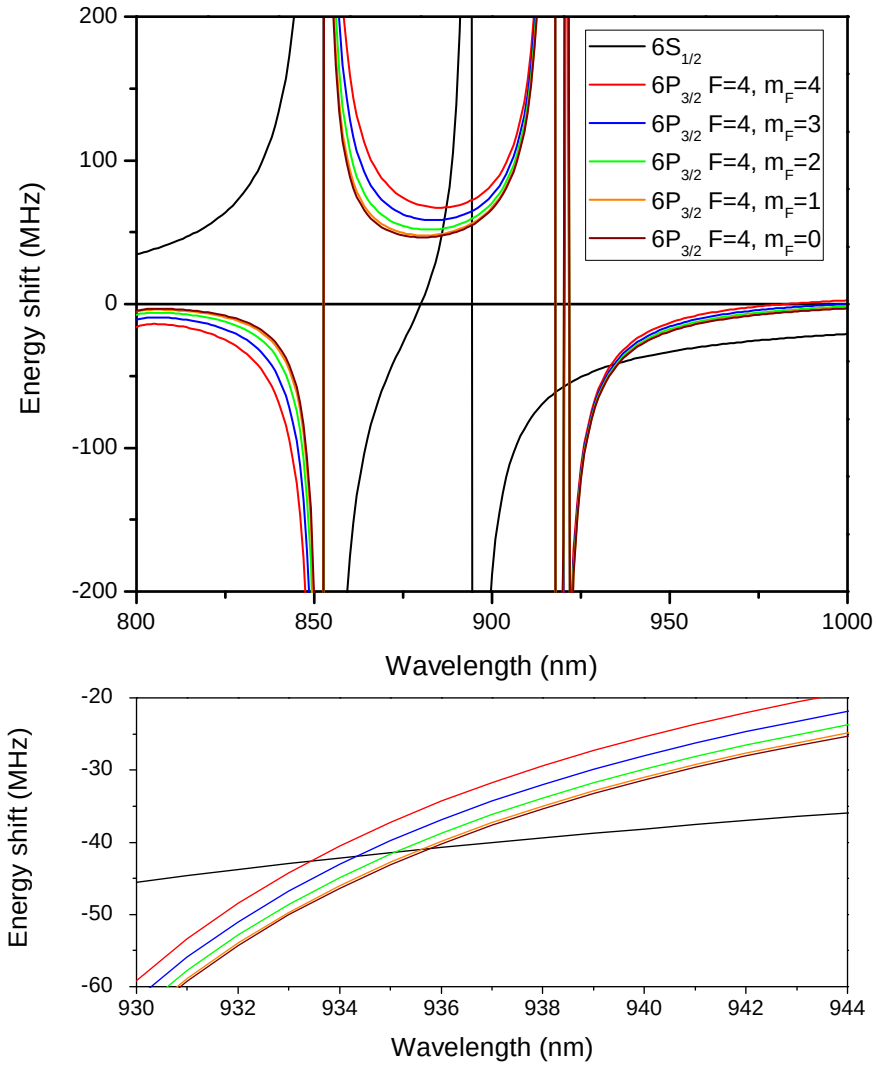

Figure 2.5: (Top) Numerically calculated AC Stark shift of the ground and excited states of Cs for linear polarisation at an intensity of $I_0 = 3.0 \times 10^9$ W/m^2. (Bottom) Magnification of the top graph between 930 nm and 944 nm. All sublevels of the ground state experience the same shift but the excited state levels ($F_e = 4$) are split. The crossing points of each line indicates the magic wavelength for each sublevel which is around 935 nm.

From figures 2.4 and 2.5, the wavelength for which the state-insensitive trapping occurs for the different sublevels is between 934 and 940 nm. Our dipole trap has a wavelength of 935.6 nm [39, 44]. The relevant light shifts for the different sublevels at this wavelength are reported in figure 2.6.

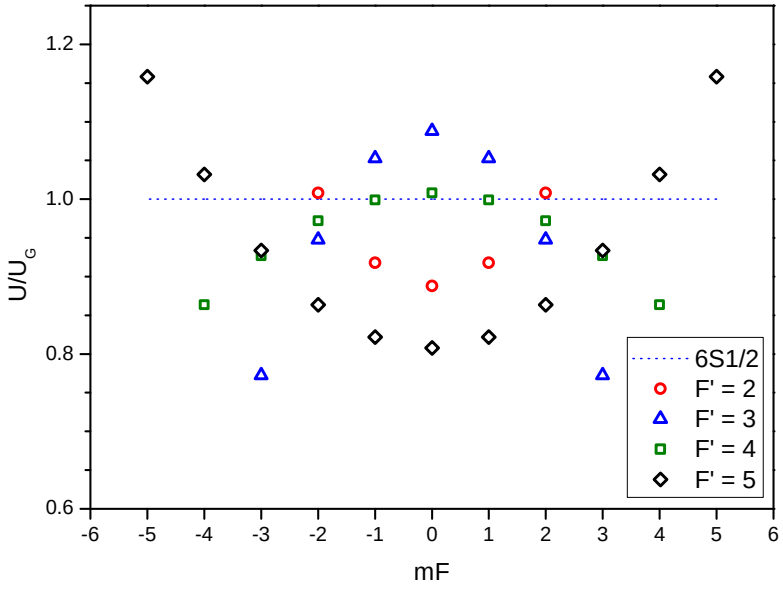

Figure 2.6: Numerically calculated AC Stark shift of the Cs excited state (F_e = 2, 3, 4, 5) sublevels, rescaled by the ground state shift. Calculations are carried out for a wavelength of 935.6 nm.

The advantages of the state-insensitive dipole trap are the reduction of the dipole force fluctuation (see section 4.3.6), and the possibility to perform atomic spectroscopy and laser cooling as in free space. In a generic dipole trap, the excited state shift is opposite to the shift of the ground state. This causes a fluctuating force on the trapped atoms as they experience different potentials. However, the state-insensitive trap provides the same shift, thus the dipole force fluctuation is significantly reduced.

From a spectroscopy point of view, the trap at the magic wavelength reduces the atomic transition shifts with respect to the normal dipole trap. As can be seen in figure 2.6, we cannot have equal light shifts for all sublevels of the ground and excited states. Although the shifts are still below ±20 % relative to the ground state shift, they can affect the spectroscopy as the natural linewidth of caesium (Γ_{D_2}) is $(2\pi)5.22$ MHz. A lower trap depth can be used to further reduce unwanted shifts. For

example, a trap depth below 800 μK produces relative shifts smaller than the natural linewidth.

2.3.3 Modelling of an optical dipole trap

In this section, the different kinds of optical dipole trap are examined to determine the trap depth and the trap frequency. In order to model the dipole trap, I assume that our laser has a Gaussian beam profile which is written as [45]:

$$E(x,y,z,t) = E_0 \frac{w_0}{w(z)} e^{-\frac{x^2+y^2}{w^2(z)}} e^{-ik(\frac{x^2+y^2}{2R(z)}+z)} e^{-i\omega t}, \tag{2.31}$$

where:

w_0 is the beam waist,
$z_0 = \frac{\pi w_0^2}{\lambda}$ is the Rayleigh range,
$R(z) = z + \frac{z_0^2}{z}$ is the radius of curvature,
$w(z) = w_0\sqrt{1+\frac{z^2}{z_0^2}}$ is the spot size.

The equation above describes an electric field propagating in the z direction which has an intensity:

$$I(x,y,z) = \frac{c\epsilon_0}{2} E(x,y,z,t)^2. \tag{2.32}$$

The beam intensity is then used to compute the trap depth with equation (2.30). In our calculation, the trap laser has a wavelength of 935.6 nm, with a power of 200 mW, and a beam waist $w_0 = 6.69\,\mu m$.

Single focussed beam dipole trap

The simplest optical trap [7, 8, 32] is a single tightly focussed Gaussian beam. The trap depth depends on the beam intensity. The beam intensity is calculated from equation (2.31) and (2.32) as:

$$I(r,z) = \frac{2P}{\pi w^2(z)} e^{-2\frac{r^2}{w^2(z)}}. \tag{2.33}$$

By substituting the intensity into equation (2.25) or (2.30), the trapping potential is then written as:

$$U(r,z) = U_0 \frac{1}{1 + z^2/z_0^2} e^{-2\frac{r^2}{w^2(z)}}, \tag{2.34}$$

where U_0 is the potential depth at the focus which is determined from the maximum beam intensity $I_0 = \frac{2P}{\pi w_0^2}$.

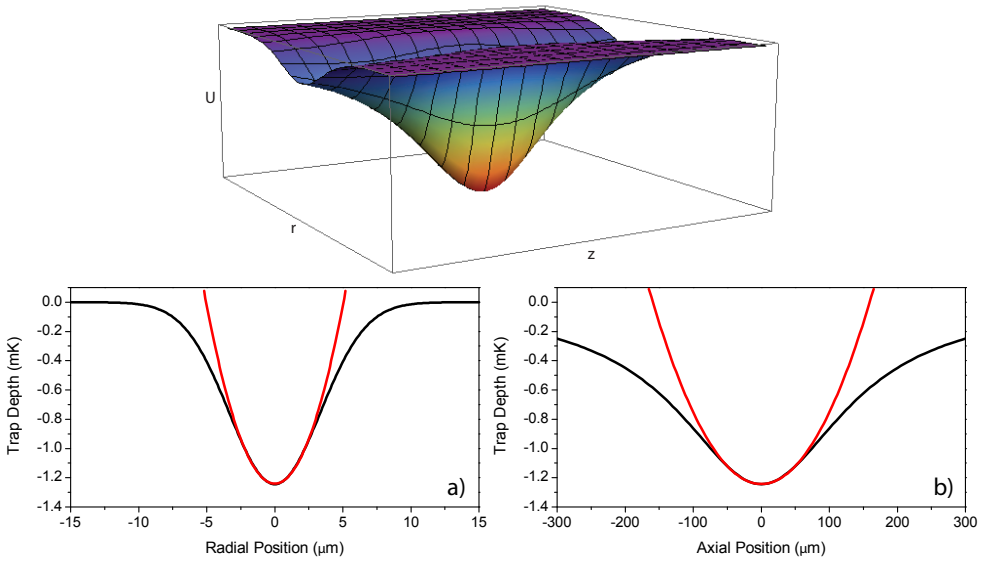

Figure 2.7: Model of the single focussed beam dipole trap. The cross section for the radial axis is shown in a) and for the axial axis in b). The red lines are best fits with a harmonic potential.

From figure 2.7, we notice that the bottom of the trap can be approximated as a parabola by using the Maclaurin series to expand equation (2.34). Thus the harmonic potential can be derived and the trap frequencies can be calculated. For the radial axis in figure 2.7a), the trap potential follows the Gaussian function ($e^{-2\frac{r^2}{w^2(z)}}$). The radial trap frequency is then given by:

$$\omega_r = \sqrt{\frac{-4U_0}{m\omega_0^2}}. \tag{2.35}$$

On the other hand, for the axial direction in figure 2.7b) the trap potential behaves as a Lorentzian function ($\frac{1}{1+(z/z_R)^2}$). The axial trap frequency is then written as

$$\omega_z = \sqrt{\frac{-2U_0}{mz_R^2}}. \tag{2.36}$$

As a result of the difference in axial and radial trap frequencies, the confinement in the axial direction is much weaker than the radial direction. Consequently, the setup of this trap has to be horizontally aligned so that the force in the radial direction holds atoms against gravity.

1D lattice dipole trap

A simple way to obtain a strong confinement and increase the trap depth is to set up a retro-reflecting beam, thus creating a standing wave. The intensity is then computed from two counter-propagating beams by assuming that both beams have equal power and the same beam waist:

$$I(r,z) = \frac{8P}{\pi w^2(z)} e^{-2\frac{r^2}{w^2(z)}} \cos^2(kz). \tag{2.37}$$

The intensity of the 1D optical lattice is four times larger than the single focussed beam. The potential is then written as:

$$U(r,z) = U_0 \frac{1}{1+z^2/z_0^2} e^{-2\frac{r^2}{w^2(z)}} \cos^2(kz), \tag{2.38}$$

where U_0 is the potential depth at $I_0 = \frac{8P}{\pi w_0^2}$.

Similarly to the single focussed dipole trap, the radial direction of the trap follows the Gaussian term. The trap frequency is then given by

$$\omega_r = \sqrt{\frac{-4U_0}{m\omega_0^2}}. \tag{2.39}$$

The axial direction in figure 2.8b) has an additional periodic term ($\cos^2(kz)$) due to the interference of the two lattice beams. The trap frequency then depends on the wavelength of the trap laser. By expanding the periodic and the Lorentzian term, the vibrational frequency in the

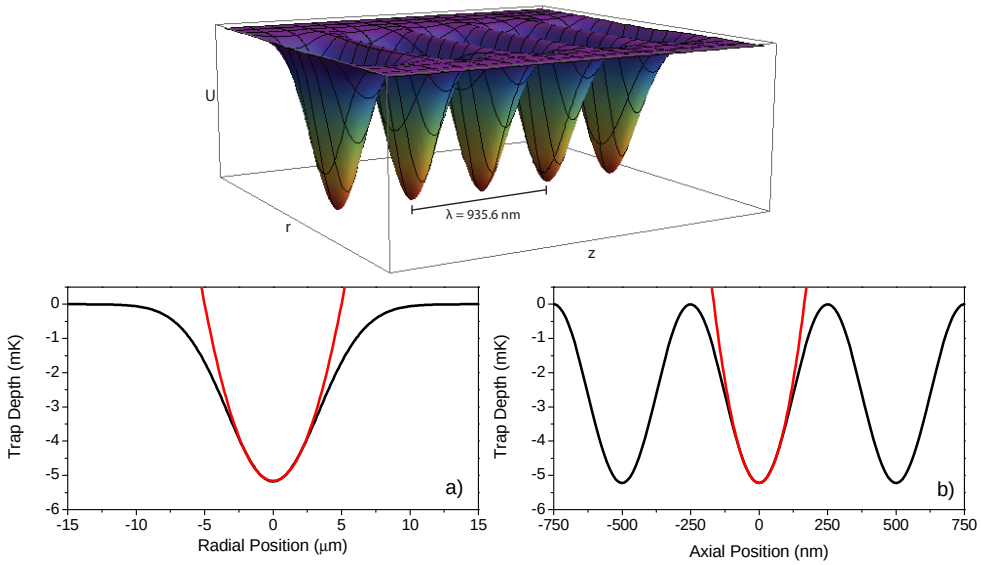

Figure 2.8: Illustration of the trapping potential for a 1D lattice. This trap has a periodicity in the axial direction of $\lambda/2$. The cross section of the dipole potential for the radial axis is shown in a) and for the axial direction in b). The red lines are beat fits with a harmonic potential to determine the vibrational frequency.

axial direction can be written as

$$\begin{aligned} \omega_z &= \sqrt{\frac{-2U_0}{m}\left(\frac{1}{z_0^2}+k^2\right)} \\ &\approx \sqrt{\frac{-2U_0k^2}{m}}. \end{aligned} \tag{2.40}$$

The confinement in the axial direction thus becomes stronger due to the periodic term. This force can then separate the trapped atoms into different potential wells. This will be discussed further in the context of the study of collisional losses in chapter 5.

Chapter 3

Experimental apparatus

This chapter describes the experimental setup, which consists of four parts: the laser system, the optical phase-locked loop, the vacuum system and the imaging system. In addition to these equipments, our experiment used magnetic coils and a computer control system which were designed by Peter Douglas and are described in [46].

3.1 Laser system

Tunable lasers are a standard tool in atomic physics [47]. In our experiment, the MOT laser is provided by a commercial semiconductor diode laser, while the dipole trap laser, requiring power more than 100 mW, is obtained by a Ti-sapphire laser. In this section, I will describe the setup of the lasers, the optical elements for the MOT system, and the MOT laser frequency stabilisation. Finally, I will describe the setup of the Ti-sapphire laser.

3.1.1 MOT laser

In order to trap and cools atoms to micro kelvin temperatures, a stable, narrow linewidth and tunable laser are general requirements [48]. The lasers of the MOT system consist of a cooling laser (also called the master laser) and a repumper laser. The frequencies of both lasers need to be stabilised to an atomic transition.

Laser construction

According to the requirement of the laser system, external cavity diode lasers (ECDL) are used in the experiment. There are many designs for external cavity diode lasers and a schematic of our ECDL is shown in figure 3.1. It is a single-sided extended cavity in the Littrow Configuration which follows the design of ref. [49]. This configuration is the most widely used for the following reasons: availability of commercial laser diodes, easy and simple setup, and a broad tuning range [47, 49].

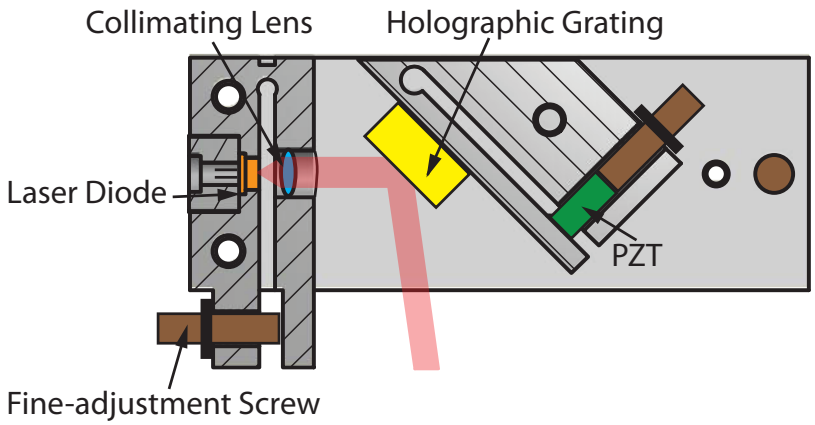

Figure 3.1: A sketch of an external cavity diode laser in the Littrow configuration.

In this configuration, a laser diode[1] and a high numerical aperture lens are placed in the mounting block. The laser beam can be finely collimated via a fine adjustment screw. The collimated beam is incident onto a diffraction grating which was aligned so that the first diffraction order is back-reflected into the laser diode. The first order optical feedback from the grating creates an external optical cavity while the zeroth order is used as the laser output. In order to tune the laser frequency, a piezo-electric actuator is used to change the external cavity length which also changes the feedback wavelength by tilting the angle of the grating. To avoid change in frequency due to thermal expansion, the mounting block is temperature stabilised. The construction in figure 3.1 is placed on a Peltier element and equipped with an AD590 temperature sensor.

[1] HL8342MG from Opnext

A home built PI temperature control circuit[2] is used to stabilise the temperature to below 10 mK uncertainty. Furthermore, acoustic and vibrational noise can also cause the variations of cavity length leading to frequency fluctuations. To avoid the fluctuations, our laser was enclosed in an aluminium box to reduce the acoustic noise. Also, we tried to avoid mechanical movements on the optical table with the laser.

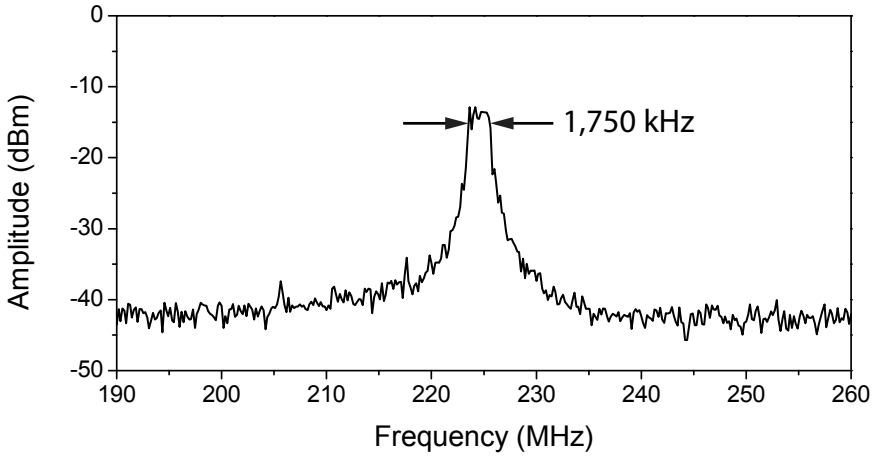

Figure 3.2: The beat spectrum of two free running ECDLs.

The laser linewidth was measured by beating two free running lasers [50], and the beat signal was detected by an ultrafast photodiode from Hamamatsu. The result is shown in figure 3.2. The width of the beat signal was $(1,750 \pm 60)$ kHz, corresponding to a linewidth of around 1,240 kHz for each laser. Although the linewidth of the lasers is around 1 MHz in 1 s measuring time, their frequencies still drift on longer time scales e.g., when the lab temperature changes.

Frequency stabilisation

For applications in laser cooling, it is important to keep the laser frequency at or near a specific atomic resonance for a long period of time. There are many techniques to stabilise the laser frequency on a desired atomic transition, such as FM spectroscopy lock and dichroic atomic

[2]Our temperature control circuit uses the chip module WTC3243 from Wavelength Electronics.

vapour laser lock (DAVLL) [51, 52]. In our system, we implement a Doppler-free dichroic atomic vapour laser lock (DF-DAVLL) [52]. While this lock is easy to setup, its disadvantage is that stray magnetic field can perturb our experiment, and temperature drifts can move the level of the error signal.

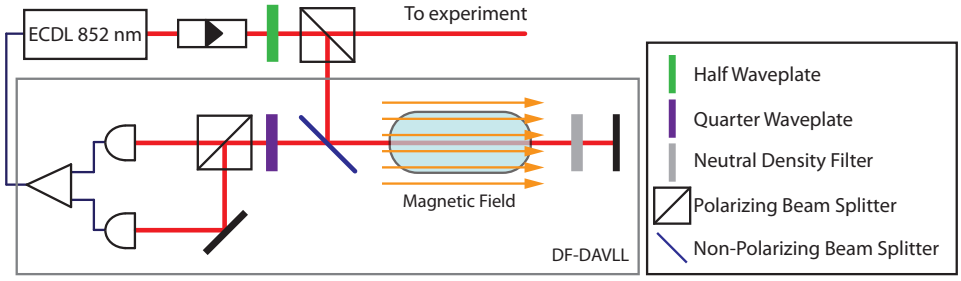

Figure 3.3: The optical diagram for a DF-DAVLL setup.

A diagram for a DF-DAVLL setup can be seen in figure 3.3. A small fraction of the power from ECDL is sent to the locking system depicted in the gray box. The laser beam is reflected from a non-polarising beam splitter into a Cs vapour cell and retro-reflected back from a mirror. In order to get a better Doppler-free saturated absorption spectroscopy, a neutral density filter reduces the power of the returning beam.

To create the DF-DAVLL error signal, the Cs cell is enclosed in a solenoid, which produces a weak magnetic field along the beam direction. In this configuration, a linearly polarised beam can be considered as a superposition of σ^+ and σ^- circularly polarised light. In a magnetic field, the Cs hyperfine levels are shifted due to the Zeeman effect. As a result, the $\sigma^\pm$ photons from the probe beam are absorbed following the selection rules: $\Delta \mathrm{m} = \pm 1$ for $\sigma^\pm$ light. By an optical pumping process, the atoms are pumped into the state: $\mathrm{m}_F = \pm \mathrm{F}$ where their energy levels are shifted in opposite directions. After that, the probe beam passes through the non-polarising beam splitter again. The superposition of the different circular polarisations are converted into linear polarisation by a quarter waveplate. Finally, the two shifted signals are separated by a polarising beam splitter and then detected by two photodiodes.

To produce the error signal in figure 3.4, the two spectroscopy signals were electronically subtracted in the photodiode box. They were then fed to the home built PI lock box which was used to stabilise the piezo

voltage (for details about the electronic locking system, see Appendix A).

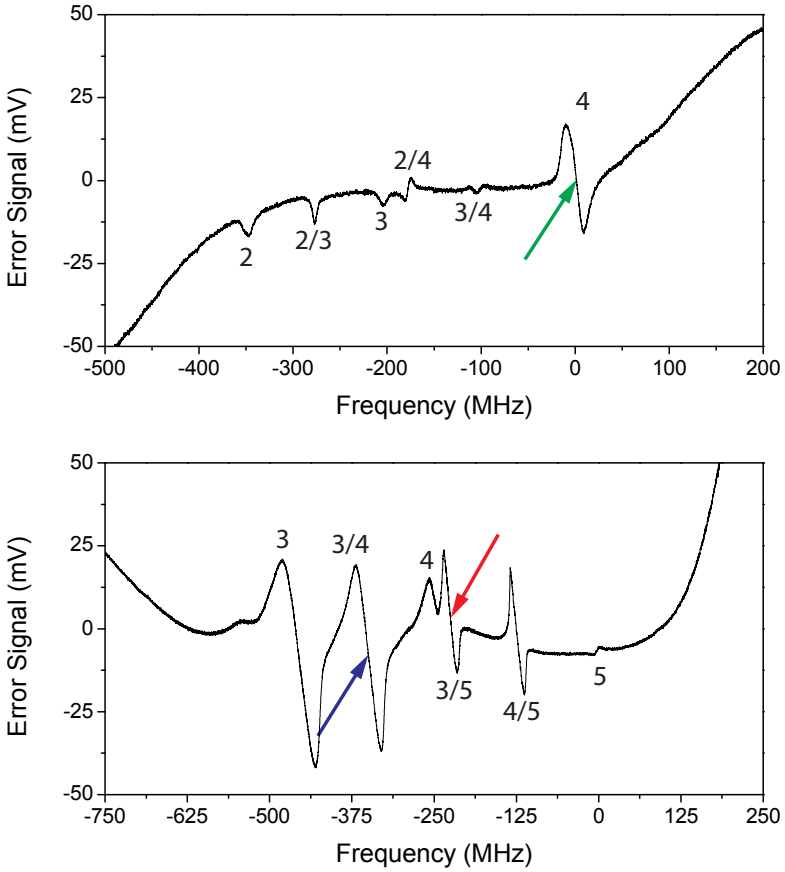

Figure 3.4: The error signal produced by the DF-DAVLL shows the error signal from the F = 3 ground state (upper graph) and the signal from the F = 4 ground state (lower graph). The number in the figure indicates the excited state. The arrows point at the locking transition of each laser: the master laser (red arrow), the repumper laser (green arrow) and the depumper laser (blue arrow).

The laser linewidth of the locked laser was measured by beating the master ($F_g = 4 \rightarrow F_e = 3/5$) and the repumper ($F_g = 3 \rightarrow F_e = 4$) beam on a photodiode. Both lasers were locked by the DF-DAVLL. The beat signal of around 9.2 GHz was then mixed down with the reference frequency at 9 GHz before analysing it by a spectrum analyser. The linewidth in 1 s measuring time was (402 ± 9) kHz, corresponding to a linewidth of around 285 kHz for each laser.

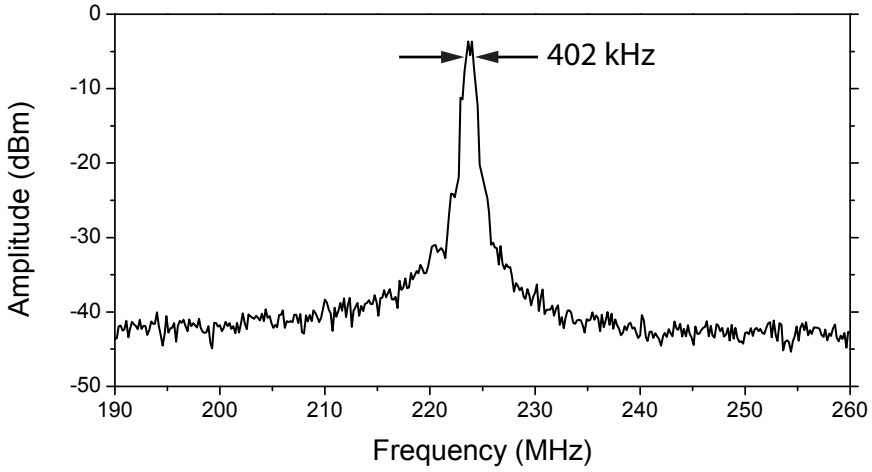

Figure 3.5: The beat spectrum of two ECDLs with the DF-DAVLL.

Cooling laser

The main laser in the experiment is the cooling laser. This laser cools the atoms via Doppler and sub-Doppler cooling. It is constructed in a master-slave configuration since the power from the master is not sufficient to operate the MOT. An injected laser (also called slave laser) requires a few μW power from the master laser to be forced to lase on the master frequency. The optical setup for the cooling laser is illustrated in figure 3.6.

The laser is locked on the $F_g = 4 \rightarrow F_e = 3/5$ crossover transition by the DF-DAVLL. Since the locking point is red-detuned with respect to the cooling transition by about 226.5 MHz, the laser beam is sent through a double pass AOM to shift the frequency slightly below the cooling transition ($F_g = 4 \rightarrow F_e = 5$). The shifted beam is then coupled to a polarisation maintaining (PM) fiber[3] mounted in a fiber port[4] which can be finely aligned via 6 degrees of freedom. A crucial alignment of the PM fiber optic is the orientation of the linear polarisation. If it is not aligned with the slow axis or the stress rod direction[5], the output polarisation will change between linear and circular polarisation. The

[3]P3-780PM-FC-5 Panda style PM fiber optic from Thorlabs
[4]PAF-X-15-PC-B fiber port from Thorlabs
[5]The connector key is normally aligned to a slow axis

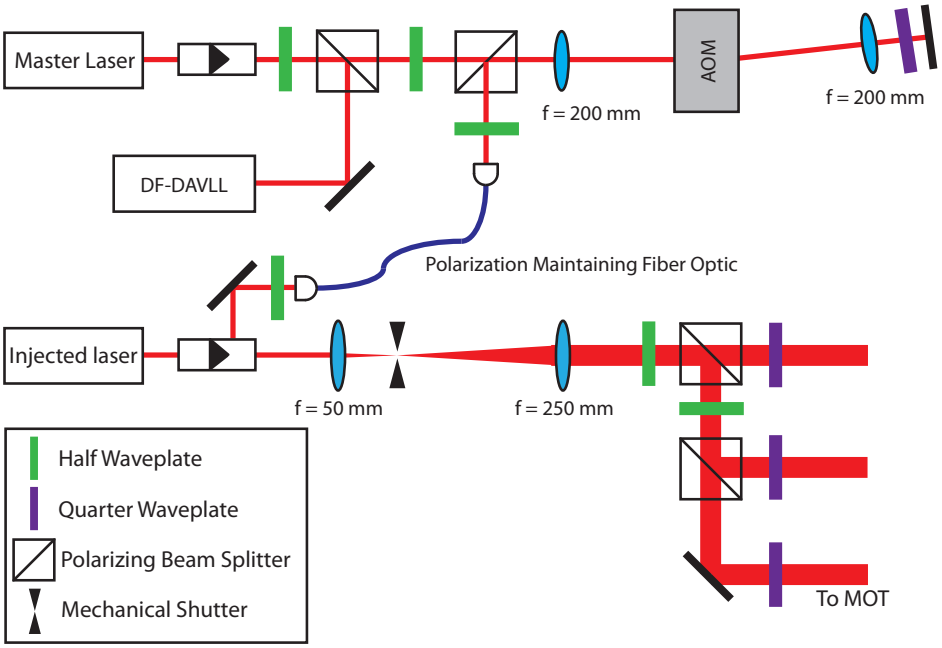

Figure 3.6: The schematic of the optics for the master laser and the injected laser.

collimated output beam from the fiber is sent through a half waveplate into a side port of the slave's optical isolator.

To inject the laser, a few mW of the master laser were fed into a free running laser[6]. It is important to match the beam shape of the master laser and the injected laser to produce an injection over a large current range. Under the right conditions of temperature and current, the output from the slave laser has identical characteristics to the master laser. The output power from the injected laser is around 50 mW. It is expanded by a 1:5 telescope to a beam waist of 6.42 mm. A mechanical shutter is positioned in the focus of the telescope. This beam is then split into three beams as required to operate the MOT.

Repumper laser

The repumper laser is another laser needed for a MOT. Even though the cooling transition is closed, there is some probability that the atoms are excited into the $F_e = 4$ excited state and decay to the $F_g = 3$ ground state. The repumper then recycles the atoms in the $F_g = 4$ ground state.

[6]SDL-5412-H1

The optical setup for the repumper is shown in figure 3.7.

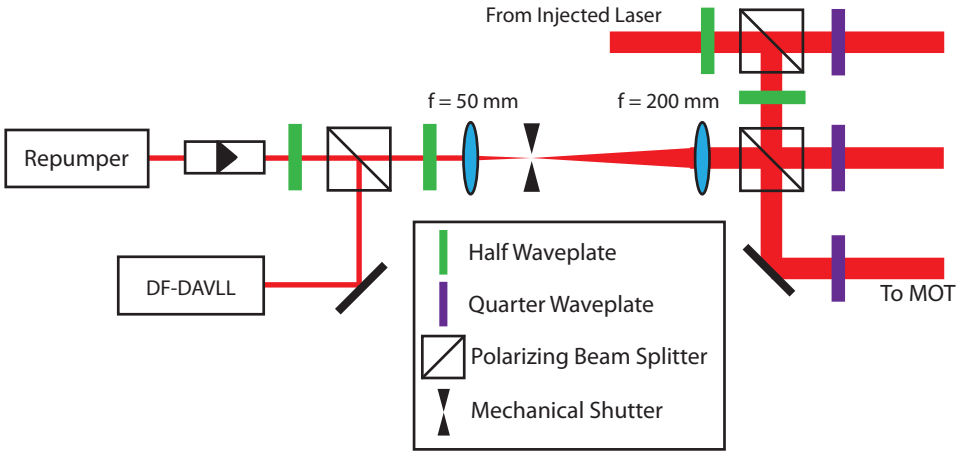

Figure 3.7: The optical schematic for the repumper laser.

The repumper laser is also locked via a DF-DAVLL on the $F_g = 3 \rightarrow F_e = 4$ transition. The laser beam with a power of about 1 mW is expanded by an 1:4 telescope. It can be switched by a mechanical shutter. Finally, it is overlapped with the master laser beam on a polarising beam splitter.

Depumper laser

Another laser which plays an important role in our experiment is the depumper laser. This laser was used to prepare atoms into the lower hyperfine ground state ($F_g = 3$). The hyperfine changing collisions in the dipole trap are in this way suppressed (see details in section 4.3.4).

The depumper laser is locked to the $F_g = 4 \rightarrow F_e = 3/4$ crossover transition and then the frequency was shifted down into resonance with the $F_g = 4 \rightarrow F_e = 3$ transition by an AOM. As a result, we were able to control the intensity and the frequency of the laser which was useful for the experiment (see section 4.3.4). The depumper beam had a maximum power of 9.4 mW and a beam waist of 2.48 mm. It can also be switched by a mechanical shutter.

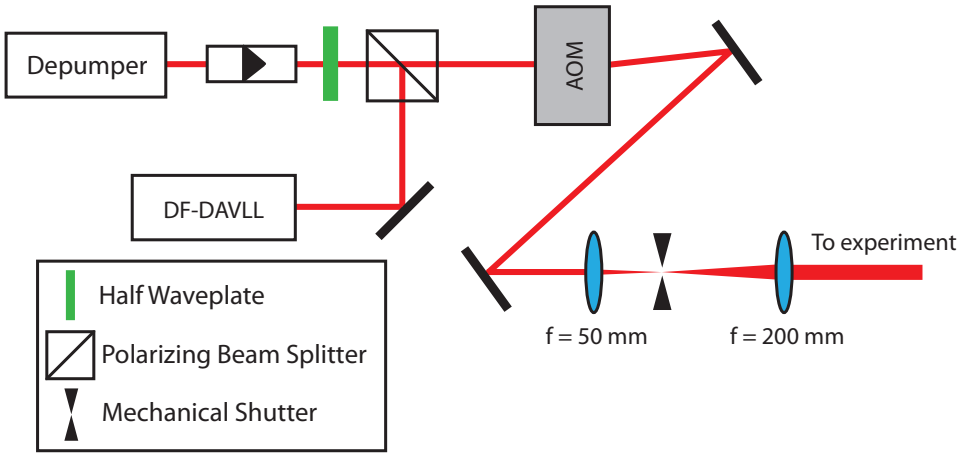

Figure 3.8: Optical schematic for the depumper laser.

3.1.2 Titanium sapphire laser

The laser used to produce a dipole trap in chapter 4 was a Ti-sapphire laser depicted in figure 3.9. It consists of a pump laser[7] and a Ti-sapphire crystal contained in a ring cavity[8]. The pump laser is a standard diode-pumped solid-state laser, which gives a continuous wave output at 532 nm wavelength and a maximum power of 8 W. The Ti-sapphire cavity spacer is constructed in a single piece of aluminium to increase the stability of the system [53].

In the block resonator, a Ti-sapphire crystal is mounted on a water cooled brass block, and four mirrors are used to create a bow-tie ring cavity. To prevent the cavity from operating in two directions, a Faraday rotator is installed. Due to the broad gain spectrum of the crystal, the wavelength range of the system is defined by the output coupler mirror (M4). There are 3 sets for different wavelengths: short wavelength 700 - 780 nm, medium wavelength 780-870 nm, and long wavelength 870 - 980 nm [54]. We operated the laser with the 870 - 980 nm set.

To tune the laser to the required wavelength, the angle of a birefringent filter, which directionally depends on the polarisation of light can be adjusted by a micrometer screw to obtain the minimum loss for the required wavelength. This is a coarse adjustment method capable of tuning several nm. To fine tune the frequency, the angle of thin intracavity

[7]Coherent Verdi-V8
[8]Coherent MBR-110

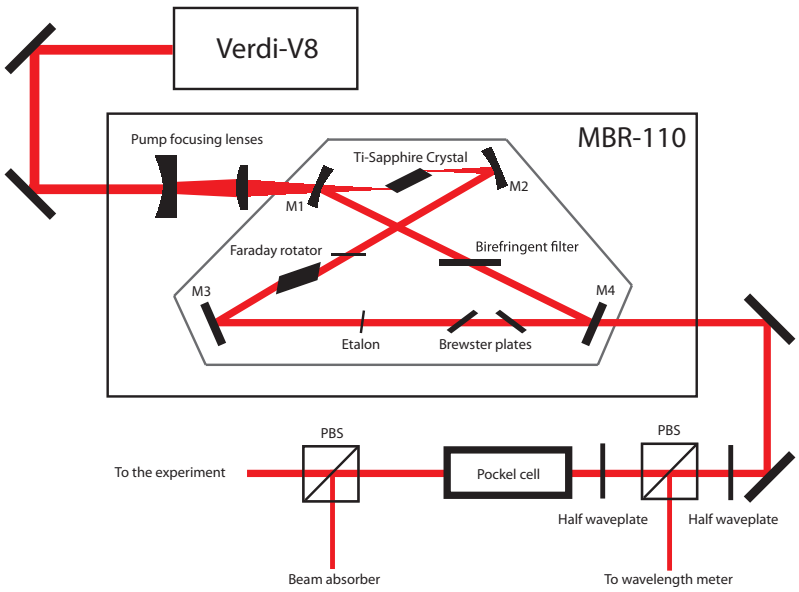

Figure 3.9: A scheme of the Ti-sapphire setup for the experiment in chapter 4.

etalon could be adjusted. Moreover, the etalon prevents laser mode-hops by locking it to the maximum transmission.

In order to reach the maximum output power, the optical elements in the ring cavity need to be regularly cleaned and slightly realigned. Furthermore, the laser was placed in a wooden box, as a reduction in temperature fluctuations increases the output power stability.

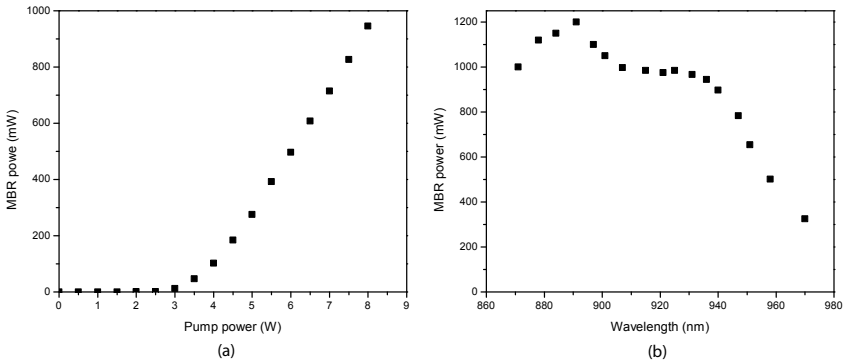

Figure 3.10: The output power of the MBR-110 at a wavelength of 935 nm as a function of the pumping power from Verdi-V8 is plotted in (a) and the maximum output power as a function of the wavelength is shown in (b).

In the experiment described in chapter 4, the selected wavelength was around 935 nm, so the long wavelength mirror set was required. The output power of the Ti-sapphire laser strongly depends on the pumping power and on the desired wavelength, as shown in figure 3.10. The threshold pumping power for laser operation of the MBR-110 was around 3.5 W and the peak output power for the long wavelength optic set was around 890 nm. Nonetheless, the laser power around 935 nm with the maximum pumping power of 8 W was about 900 mW which was enough to create a trap depth of ~ 2 mK.

In addition to gaining the maximum power, the laser output power needed to be modulated for measuring the vibrational frequency in section 4.3.3. Hence a Pockel cell was installed, which rotates the polarisation of the beam as a function of the applied voltage. Together with a polarising beam splitter, this provides controllable laser power on μs scale.

3.2 Optical phase-locked loops

Electromagnetically induced transparency (EIT) has many applications in precision metrology [55, 56] and nonlinear optics [57]. Phase coherent laser sources are necessary to generate ground state atomic coherence. Various techniques have been developed to obtain two coherent sources of light. They make use of acousto-optic modulators (AOM), electro-optic modulators (EOM), direct current modulation of a vertical cavity surface emitting laser (VCSEL), and optical phase-locked loops (OPLL) [55].

In the case of the VCSEL, the current of the laser is modulated to create frequency sidebands. The same result can be produced by passing the laser beam through an EOM. Disadvantage of this method is that it requires additional optics to separate the sidebands to be able to control the relative intensity and polarisation [58]. The latter problem can be overcome with the use of an AOM. However at very large frequencies, like those required in our experiment, AOMs are expensive and have low efficiency [59]. In our experiment, we have chosen to use an OPLL so as to be able to easily control the polarisation and intensity of the two beams.

3.2.1 The basic loop

A phase-locked loop (PLL) is a control circuit which synchronises a control signal with a reference signal to gain the same frequency and phase [60, 61]. A PLL is widely used in frequency synthesis where the output oscillates at a multiple of the reference frequency. A basic diagram for a PLL is shown in figure 3.11 consisting of a phase detector, a loop filter and a voltage controlled oscillator [62, 63].

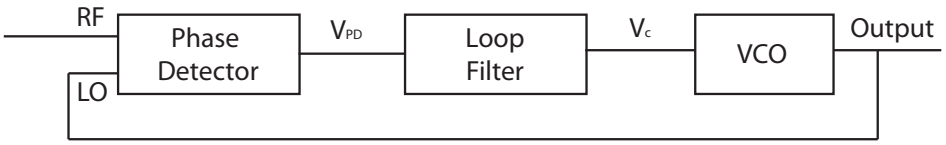

Figure 3.11: A block diagram of the phase-locked loop [63].

From the block diagram, the reference frequency (RF) is mixed with the local oscillator (LO). This can give the result as the multiplication of two sinusoidal waves:

$$\begin{aligned}\cos(\omega_A t + \phi_A)\cos(\omega_B t + \phi_B) &= \frac{1}{2}[\cos((\omega_A + \omega_B)t + (\phi_A + \phi_B)) \\ &+ \cos((\omega_A - \omega_B)t + (\phi_A - \phi_B))] \quad (3.1)\end{aligned}$$

The high frequency components from the phase detector (V_{PD}) are then filtered by the loop filter. The low frequency part (V_c) is then used to control the output frequency of the voltage controlled oscillator to give the output frequency as the local oscillator. Again, this LO is then fed back to the loops to stabilise the frequency output to the reference frequency.

The loop bandwidth is an important parameter to characterise the PLL. It determines how stable the locking is and how fast it can follow the changing phase [63, 64]. The larger the loop bandwidth is the more stable the loop is, but a large bandwidth makes a slow response time due to the large frequency range to stabilise.

3.2.2 The optical phase-locked loops

In order to lock the phase of two lasers, the frequency difference has to be measured and compared to the reference frequency. Once the offset frequency is stabilised, the phase difference of two lasers is compared to the reference phase. The phase differences are examined from the two laser fields, given by:

$$\begin{aligned} E_1(t) = &\quad E_{01}\cos(\omega_1 t + \phi_1(t)) \\ E_2(t) = &\quad E_{02}\cos(\omega_2 t + \phi_2(t)). \end{aligned} \tag{3.2}$$

One of the lasers needs to be locked to an atomic transition, for example the $F_g = 4 \rightarrow F_e = 3$ or 4 D_2 line transition. As shown in figure 3.12, the PLL1 laser is stabilised by the DF-DAVLL, the error signal is then fed back to the current driver to stabilise against fast oscillations and also to the piezo to compensate slow drifts.

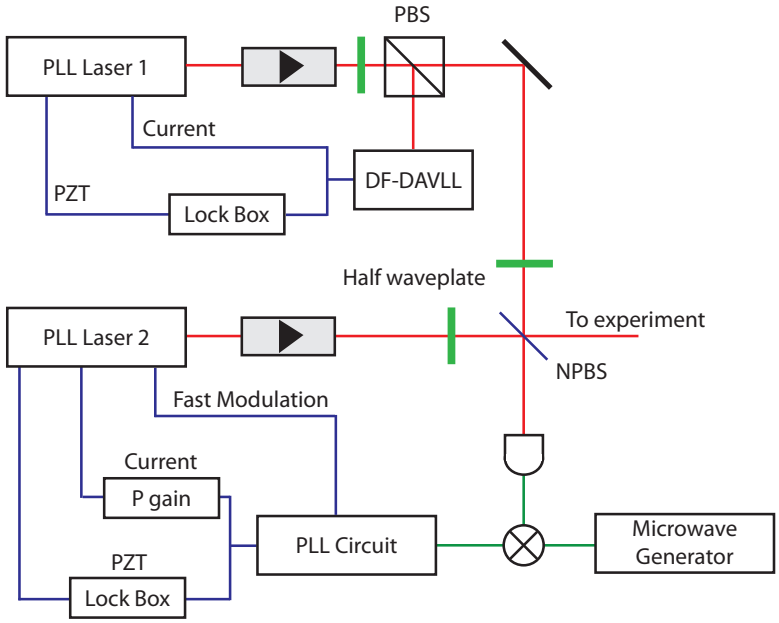

Figure 3.12: The laser schematic and the electronic locking diagram for PLL.

Before both laser beams are overlapped and focussed to a fast photodiode, their polarisations need to be aligned via a half waveplate. Since the beat signal of the two lasers is around 9.2 GHz, the rise and fall of the detector needs to be faster than 50 ps. In our experiment, we selected

a fast response photodetector from Hamamatsu[9] which has both rising and falling response times of 40 ps. The beat signal is then produced from the interference of two lasers

$$\begin{aligned} I(t) &= \frac{1}{2}c\epsilon_0[E_1(t)+E_2(t)]^2 \\ &= \frac{1}{2}c\epsilon_0[E_{01}\cos(\omega_1 t+\phi_1(t))+E_{02}\cos(\omega_2 t+\phi_2(t))]^2 \\ &= \frac{1}{2}c\epsilon_0[E_{01}^2\cos^2(\omega_1 t+\phi_1(t))+E_{02}^2\cos^2(\omega_2 t+\phi_2(t)) \\ &\quad +2E_{01}E_{02}\cos(\omega_1 t+\phi_1(t))\cos(\omega_2 t+\phi_2(t))]. \end{aligned} \tag{3.3}$$

From equation (3.3), there are two parts: the intensity of each laser and the intensity of the interference. By applying equation (3.1), the intensity of the beat signal is then given by:

$$I_{beat}(t) = \frac{1}{2}c\epsilon_0 E_{01}E_{02}\cos(\Delta\omega t+\Delta\phi(t)). \tag{3.4}$$

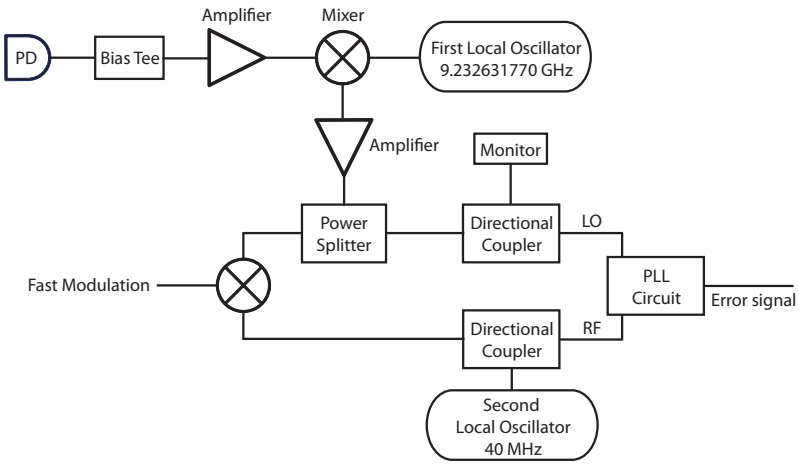

Figure 3.13: The schematic shows all RF components for the optical phase-locked loop (OPLL).

As illustrated in figure 3.13, the fast photodiode requires a bias voltage of around 10 V, so a bias tee (ZX85-12G-S+) was connected to supply this voltage and to filter the DC part out. The beat signal after this stage is very weak, it had to be amplified by two wideband amplifiers (ZX60-

[9]GaAs MSM Photodetector G4176-03

14012L+ from Mini-Circuits) with a total gain of 24 dB. The signal was then mixed down to around 40 MHz with a microwave generator (Rohde & Schwarz SMF100A) as a first local oscillator.

The output signal oscillates at 40 MHz and is amplified by an amplifier (ZFL-500LN+) before a power splitter (ZFSC-2-1+) divides the signal for the fast modulation and the phase detector. The reference frequency of 40 MHz (Rohde & Schwarz SMFY01) is also split by a directional coupler for the fast modulation and the phase detector.

In the phase detector circuit [65], an ultrafast comparator (AD96687) transforms the incoming sine wave to a pulse train which can be counted up to 200 MHz. The pulse trains are then sent to a digital phase/frequency discriminator (AD9901) used as the phase detector. The AD9901 can detect the phase within the phase difference of $0 - 2\pi$. The error signal amplitude of the AD9901 is around 1.8 V which correspond to 0.2865 V/rad. The error signal can be picked from either an inverting or a non-inverting output channel.

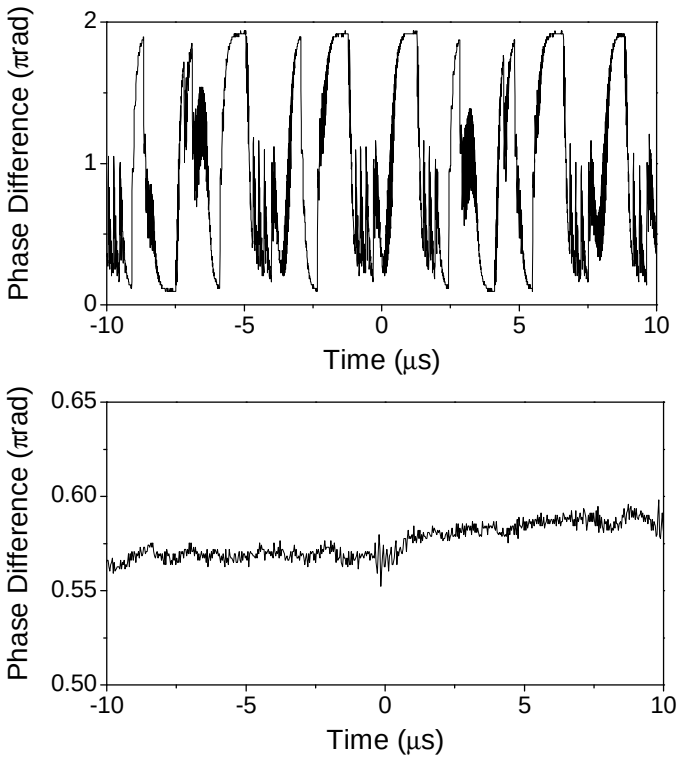

Figure 3.14: The phase difference of the two lasers when they are not phase locked (top figure) and when they are phase-locked (bottom figure).

The phase difference can be derived from the error signal as shown in figure 3.14. The top graph was recorded when both lasers were not phase-stabilised. The bottom graph was taken when the relative phase of the two lasers was stabilised via the very fast current feedback.

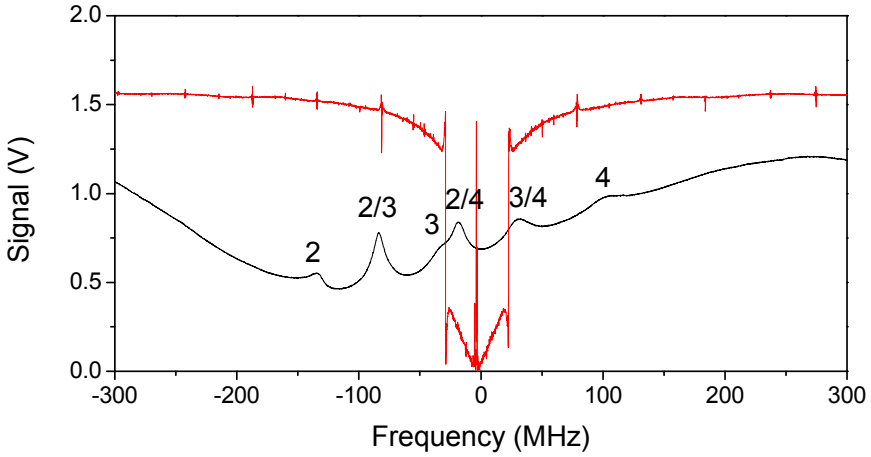

Figure 3.15: The non-inverting error signal from the PLL is shown in the red line, with one of lasers stabilised to the $F_g = 4 \rightarrow F_e = 3$ transition, The locking point of the PLL error signal is on the $F_g = 3 \rightarrow F_e = 3$ transition.

The non-inverted error signal in figure 3.15 is fed back into the lock box. The bandwidth or the frequency response for the PI lock box is around 100 Hz which is suitable for compensating slow drifts. The current feedback utilises the inverted error signal. Due to the strong feedback signal, it is attenuated by -6 dB. Furthermore, another mixer (ZFM-3) combines the local oscillator and the reference frequency to obtain a DC signal, which is used for the very fast feedback part of the stabilisation that is fed directly into the laser diode. The high-frequency component from the mixer is filtered out by a low pass filter while the low-frequency component is directly fed back into the laser diode as a very fast feedback.

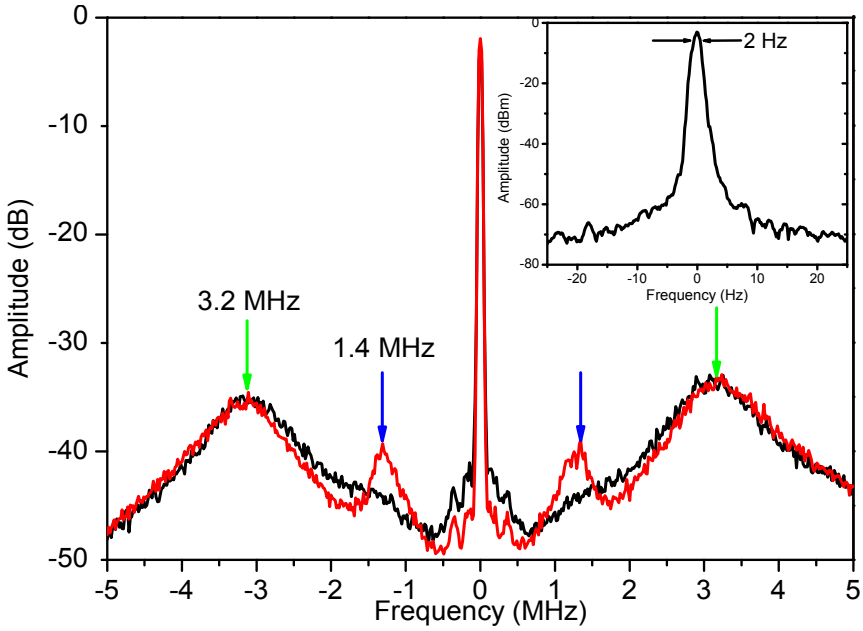

Figure 3.16: Spectrum of the beat signal of the two phase-locked lasers measured with the resolution bandwidth (RBW) of 10 kHz and 10 averages. The red data was measured with the high gain of the current feedback. The black data was measured with the optimum gain of the current feedback. The inset expanding the centre of the beat signal shows the relative linewidth of 2 Hz. The centre frequency of the spectrum is 40 MHz.

Figure 3.16 shows the beat spectrum signal of the two phase-locked lasers. The signal-to-noise ratio of the beat spectrum is around 35 dB. The relative linewidth of the two lasers is around 2 Hz as shown in the inset of figure 3.16. It is limited by the linewidth of the two function generators, as each of them has a linewidth of 1 Hz. The current feedback bandwidth is identified by setting the current feedback circuit to the maximum gain. The current feedback then starts to oscillate around the maximum frequency, which was measured to be around 1.4 MHz (as shown in figure 3.16 with the blue arrows). This gain has to be adjusted to reduce the oscillation so as to increase the stability of the loops. The optimum gain is shown in the black data where the oscillation is pushed away. Finally, the loop bandwidth was measured to be $\sim$ 3.2 MHz (as shown in figure 3.16 with the green arrows).

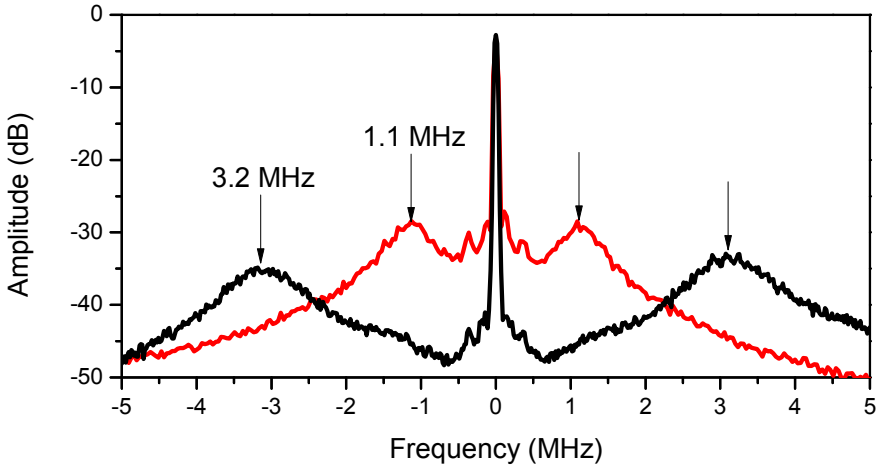

Figure 3.17: The loop bandwidth was measured with the resolution bandwidth (RBW) of 10 kHz and 10 averages. The red data illustrate the spectrum for the small loop bandwidth of 1.1 MHz. The optimum loop bandwidth of 3.2 MHz is shown in the black data.

The effect of the loop bandwidth on the spectrum of the beat signal is demonstrated in figure 3.17. The loop bandwidth can be easily adjusted by changing the resistance and the capacitance of the loop filter (see Appendix B). If the loop bandwidth is too small, it will cause the loop to be unstable. As can be seen from the red line of figure 3.17, the signal-to-noise ratio is around 22 dB, compared to the larger loop bandwidth of 3.2 MHz, which was around 35 dB. This noise level can indicate how stable the PLL is [55]. However, if the loop bandwidth is too big, the stabilisation of the loop will be slow causing the PLL to not be able to follow the changing phase.

In our experiment, the loop bandwidth is maximised to be around 3.2 MHz. This is limited due to the digital phase detector which has the phase delay much larger than the analog phase detector [64]. The phase delay limits our loop bandwidth due to it increasing the phase error in the loops. According to [64], the digital PLL has to limit a loop bandwidth around 1.7 MHz. In order to increase it, the fast digital phase detector and the phase advance filter were installed in the loop. These components can compensate the phase delay and increase the loop bandwidth to around 3 MHz.

3.3 Vacuum system

Another requirement to study laser cooling and trapping is a good vacuum, typically below 10^{-8} mbar. Collisions with the background gas cause losses from the trap (see details in section 4.3.6). In our experiment, we use a standard single vacuum chamber to study our dipole trap and its loss mechanisms.

3.3.1 Single MOT chamber

The basic design of the single MOT system is illustrated in figure 3.18.

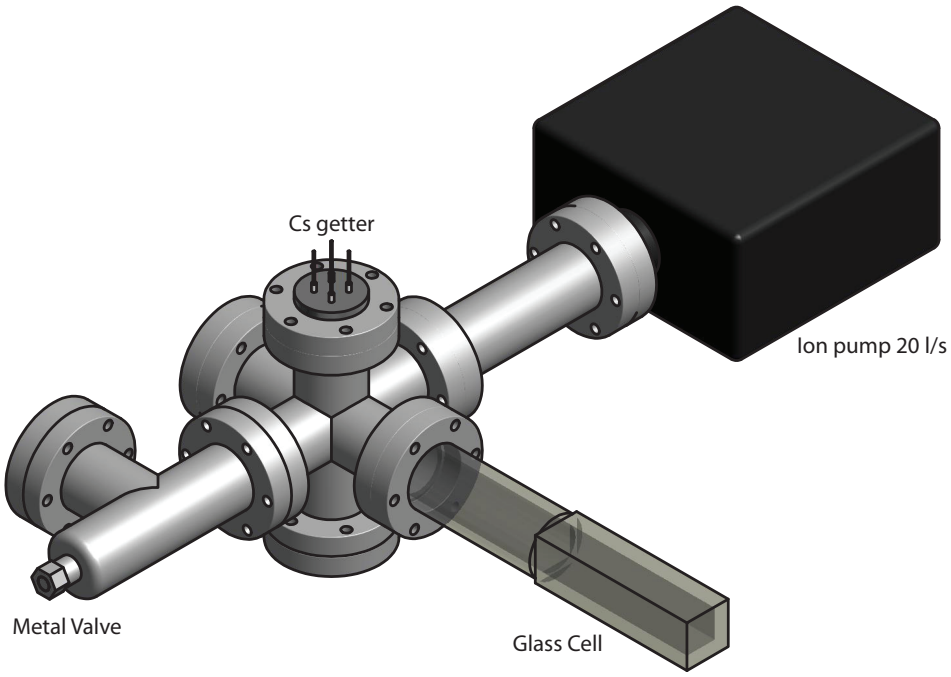

Figure 3.18: The layout of the single MOT system.

In order to achieve ultra-high vacuum (UHV), an ion pump[10] was connected to the system. This pump can reach a pressure below 10^{-9} mbar by ionising the background gas. A vacuum metal valve was installed to connect a turbo-molecular pump backed by a rotary pump. With these pumps, the system can be easily pumped down to 10^{-7} mbar. A glass

[10]Varian StarCell 20 l/s

cell[11] made from quartz glass connected to a metal flange CF40, has its outer dimension: 30×30×175 mm with a thickness of 5 mm. It provides a maximum optical access. Caesium getters[12] were used to supply the Cs atoms to the system. All components were connected together via a six-way CF40 connector piece and supported by 20 cm high aluminium mounts.

3.3.2 Bake-out procedure

After the vacuum components were assembled, the next step was to operate the pumps. A rotary pump and a turbo molecular pump were connected in series to achieve high vacuum around 10^{-7} mbar. Outgassing is a problem to reaching ultra high vacuum. Heating the system up increases the outgassing rate dramatically exhausting the residual gas in the walls on reasonable time scales. With a lower outgassing rate, the ion pump is enough to maintain ultra high vacuum in the system.

The baking process proceeded as follows: the vacuum system was wrapped with aluminium foil and a heat tape to homogeneously generate the same temperature for all parts. The temperature was increased slowly with a maximum rate of 10 °C/hr. This process was crucial for the glass cell because a temperature gradient can cause stress which can lead to a crack in the glass. The maximum baking temperature for the single MOT system was chosen to be below 200 °C, within the limits of the glass cell and the viewports.

The system was kept at the maximum temperature for 2 weeks. While cooling the system down to room temperature, the valve connecting to the turbo pump was closed and the pressure maintained only by the ion pump. The single MOT system reached a pressure below 5×10^{-9} mbar as indicated by the ion pump current.

3.4 Imaging System

In a microscopic dipole trap experiment, high sensitivity and resolution are essential requirements of the imaging system. Our objective lens can

[11] Custom built by Optiglass Ltd, 52 Fowler Rd, Hainault, Essex IG6 3UT
[12] SAES Getters, CS/NF/8/25 FT10+10, 5G00608

resolve μm length scales and our intensifier unit and photon counting module are used to detect photons scattered from a small number of atoms.

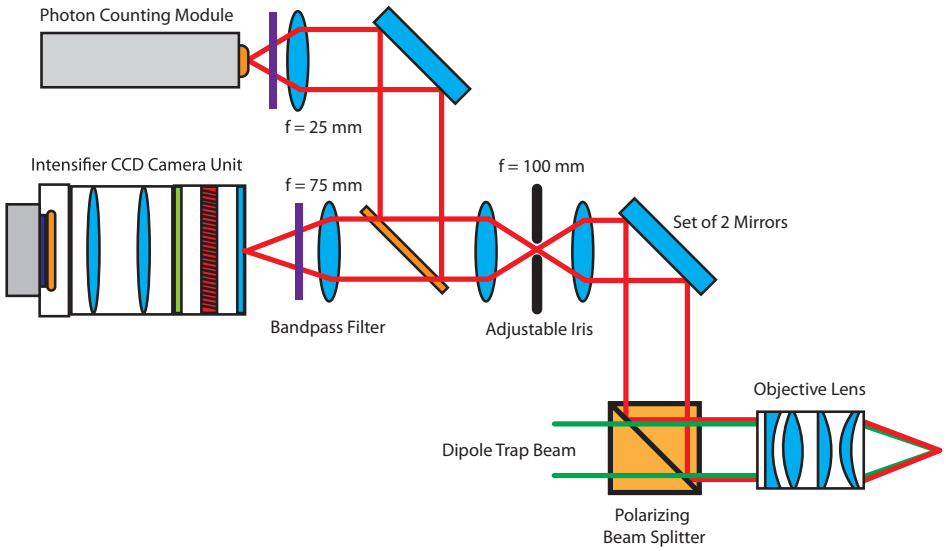

Figure 3.19: Imaging system diagram for our dipole trap experiment.

A diagram of our imaging system is shown in figure 3.19. The fluorescence of the trapped atoms is collected by the objective lens which was mounted on a XYZ translation stage. Behind the objective lens is a polarising beam splitter used to combine the imaging beam and the dipole trap beam. Two broadband mirrors (700 - 1300 nm) reflect fluorescence along an aluminium construction positioned above the glass cell. In the aluminium support, the light passes through a f = 100 mm bi-convex lens focusing the light through an adjustable iris. The iris was used to block background light. Another f = 100 mm lens recollimates the light and a 50:50 beam splitter sends 50% of the light to the intensifier camera unit and the rest to the photon counting module. For the intensifier, a f = 75 mm plano-covex lens is used to form an image on the photocathode, while a f = 25 mm bi-convex lens focuses the light on the photon counting module. In order to filter any undesirable wavelengths, a bandpass filter[13] allowing just wavelengths of (850±5) nm is installed in front of both detecters to reduce the background noise.

[13]FB-850-10 from Thorlabs

3.4.1 Objective lens

The objective lens[14] consists of 4 BK7 lenses and is housed in a black anodised aluminium tube. The lens was originally designed by Wolfgang Alt, and published in ref. [66].

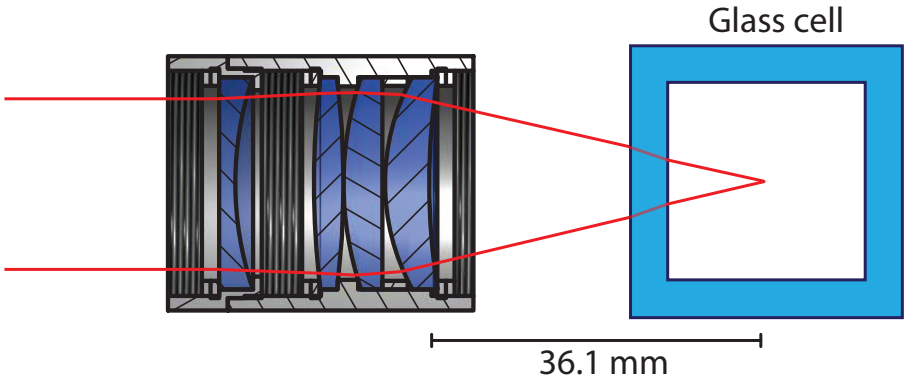

Figure 3.20: The CAD drawing of the objective lens bases on the design from ref. [66].

According to the original design in figure 3.20, at an operating wavelength of 852 nm, the objective lens has a numerical aperture (NA) of 0.29, a focal length of 36.1 mm, a solid angle of 0.021 and a diffraction-limited spot size of 1.8 μm [66]. Our experiment uses this lens for both the fluorescence imaging at 852 nm and the focusing of the dipole trap at 935.6 nm. For the wavelength at 935.6 nm, the lens has a focal length of 36.2 mm and a diffraction-limited spot size of 2.0 μm.

For the experiment in chapter 4, the objective lens was adapted by changing the second lens from the left in figure 3.20 from a bi-convex 100 mm lens to a bi-convex 200 mm lens. The focal length and the diffraction limit was then calculated by OSLO optical design software[15]. As a result of our calculation, the focal length is increased to 43.4 mm for 852 nm and 43.6 mm for 935.6 nm and the diffraction-limited spot size is also raised to 2.4 μm for 852 nm and 2.6 μm for 935.6 nm. The modified lens was appropriate for our experiment as it can ideally image with 2.4 μm resolution and focus the dipole trap beam down to a 2.6 μm waist.

[14]The objective lens is constructed by LENS-Optics GmbH.
[15]The educational version is available from http://www.sinopt.com

3.4.2 Intensifier camera unit

The microscopic dipole trap requires a high sensitivity imaging unit due to the small number of atoms in the trap. To be able to image the atomic fluorescence in the small trap, a normal camera needs a long exposure time which also increases the noise level in the image. An intensifier camera can reduce the exposure time to the scale of milliseconds and it also reduces the noise level as the CCD chip is operated at very low temperatures.

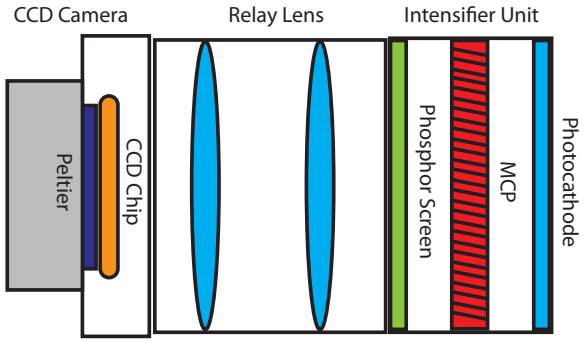

Figure 3.21: The structure of the intensifier camera unit.

The intensifier camera unit in figure 3.21 is composed of an image intensifier unit[16] and a digital CCD camera[17]. They are connected together via a 1:1 relay lens. In general, the intensifier unit contains a photocatohode, a micro-channel plate and a phosphor screen. The incoming photons are converted to electrons on a multialkali photocathode material. It has a spectral response range between 185 nm to 900 nm with a quantum efficiency of 2% at 852 nm [67]. The emitted electron is then accelerated by an electric field to hit a micro-channel plate (MCP). The MCP amplifies the electron from the photocathode. The gain of the MCP can be adjusted via the electric field on the plate. The maximum gain for the intensifier unit is around 10^6 electrons per input electron. Finally, the amplified electrons are converted into photons on the phosphor screen (P-43) which produces an image at a wavelength of 550 nm. The CCD camera then collects the photons from the intensifier unit with a quantum efficiency of 70% at 550 nm [68].

[16]Image Intensifier Unit C9016-24 from Hamamatsu
[17]IEEE1394 Digital CCD Camera C4742-80-12AG from Hamamatsu

The CCD camera chip is placed in a vacuum and cooled down to -30 °C by a Peltier element to reduce dark currents [68]. The CCD chip has 1344 × 1024 pixels, each with the dimensions of 6.45 × 6.45 μm and a readout resolution of 12 Bits or 4096 grey levels for each pixel. To be able to control the CCD camera, a serial bus IEEE 1394 (FireWire) is used to transfer the information from the CCD chip to a computer. A TTL trigger input is connected to the camera module to control the exposure time. Furthermore, the intensifier unit uses a USB interface to control the gain of the MCP and also a TTL gate to prevent the intensifier unit from excessive light input.

3.4.3 Single photon counting module

Another tool to detect ultra-weak light is a single photon counting module[18] (SPCM). It has the capability to detect the fluorescence of a single photon. An important device in this module is the silicon based single photon avalanche diode (SPAD). It can detect photons from 400 to 1060 nm wavelength with a quantum efficiency of around 50% at 850 nm.

The SPAD is a kind of avalanche photodiode (APD) using a photon-triggered avalanche current due to a high electric field between a p-n junction [69, 70]. However, the SPAD requires a bias voltage above the breakdown voltage where it can act in the Geiger Mode [70, 71]. At this mode, one single photon can produce a current in the mA scale while a bias voltage below the breakdown voltage provides a gain below the detectable range. A TTL output with a width of 15 ns is provided when it detects one photon[19]. However, the module has to reset the bias voltage after each single photon detection which takes 20 ns, so the maximum counting rate is around 35 × 10^6 counts/s. The dark count rate is around 350 counts/s.

[18] SPCM-AQR-13 from Perkin Elmer Optoelectronics

[19] The details of this module including the circuit can be found in ref. [69, 71]

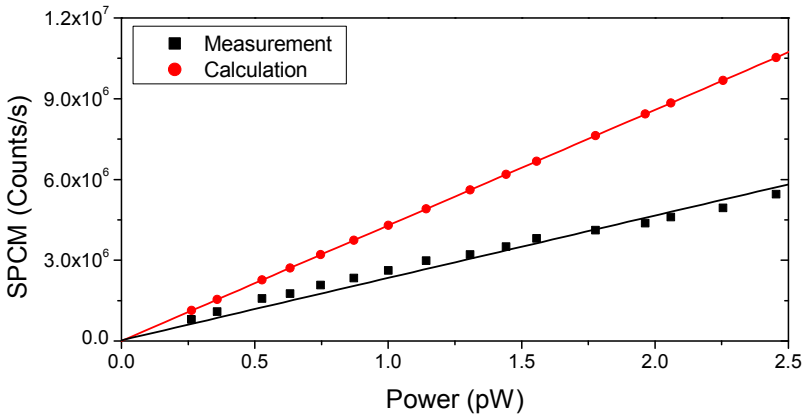

Figure 3.22: The measurement of the counting rate as a function of the laser beam power at 852 nm compared to the calculation. This result corresponds to a quantum efficiency of 54%.

To readout the number of photons, a dual counter model-995 from Ortec was used to count the standard NIM signal[20] with a value up to 100×10^6 counts/s. A fast/slow NIM logic converter model-499 from Ortec which can convert signals up to 40 MHz had to be installed as the counter requires a NIM signal.

Moreover, we can control the counting time by triggering the counter module with a TTL signal. The results in figure 3.22 allow us to derive the quantum efficiency of our single photon avalanche diode at 852 nm by comparing the counting rate to the number of photons from a laser beam measured by a photodiode.

3.4.4 Number of atoms calibration

Measuring the number of atoms is essential to investigating the characteristics of our dipole trap, especially its lifetime. In order to count the number of atoms, we measure their fluorescence in the MOT. This method is suitable for our camera and also the SPCM which is able to count the number of photons. The photon scattering rate for a single

[20]NIM is a Nuclear Instrumentation Module standard used in experimental particle and nuclear physics.

atom is given by [35]:

$$\Gamma_{sc} = \frac{\Gamma}{2} \frac{\left(\frac{6I}{I_{sat}}\right)}{1 + \left(\frac{6I}{I_{sat}}\right) + 4\left(\frac{\Delta}{\Gamma}\right)^2}, \tag{3.5}$$

where the saturation intensity (I_{sat}) of the cycling transition($\sigma^{\pm}$-polarised light) is 2.71 mW/cm^2 [35]. Our MOT beams had an intensity (I) of 5.08 mW/cm^2 per beam and a detuning (Δ) of -2Γ. These parameters gave the total scattering rate of 6.54 $\times$ 10^6 photons/(atom·s).

Optical elements	Transmission coefficient
Glass Cell (2X)	0.96^2
Objective Lens (8X)	0.995^8
Beam splitter	0.5
Mirror (2X)	0.995^2
2Lenses (4X)	0.995^4
Beam splitter	0.5
Lens (2X)	0.995^2
Bandpass filter	0.52
Total	~ 0.11

Table 3.1: The intensity transmission coefficient for each optical element. The number in the bracket indicates the number of surface for each optical element, for example (2X) indicates two surfaces.

The total value measured by the detector depends on the solid angle, the transmission properties of the imaging system as well as the detection efficiency of the module. Finally, the measured value on the camera or the SPCM is given by

$$N_{readout} = \eta T_c \Omega \Gamma_{sc} N_{atom} t, \tag{3.6}$$

where η is the detection efficiency of the detector, the transmission coefficient (T_c) is 0.11, the solid angle of our objective lens (Ω) is 0.021 as from ref. [66] and t is the scattering time or the exposure time.

From equation (3.6), we can directly measure the number of atoms with the SPCM as the quantum efficiency ($\eta = 0.54$) was measured in figure 3.22. However, the efficiency of the ICCD camera still needs to be measured.

In order to do that, a laser beam of known power and wavelength was sent into the camera through a series of attenuators to prevent the camera from an excessive power. The power of the beam is converted to the number of photons per second. The CCD intensity is then integrated over the whole CCD chip. The result of the CCD intensity was plotted as a function of the photon number with a fixed exposure time to determine the slope as the efficiency of the ICCD unit.

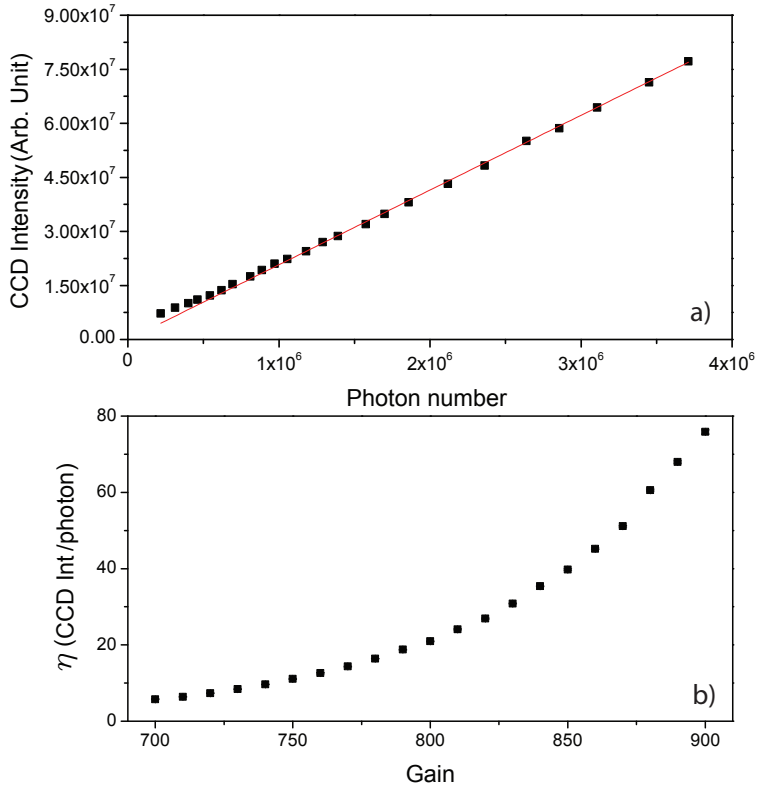

Figure 3.23: The calibration of our intensifier camera unit with the fixed intensifier gain of 800 in a) and the calibrated efficiency for the different intensifier gain in b). The calibration was done by fixing the exposure time at 4 ms.

The result of the calibration is shown in figure 3.23a. The efficiency of the camera is $\eta = 20.74$ CCD Int/photon, calibrated for an intensifier gain of 800 with the exposure time of 4 ms. Moreover, the efficiency for the different intensifier gains was also calibrated in the same way. The result of the calibration is shown in the figure 3.23b. As a result of the efficiency calibration, the number of atoms from the camera unit can be calculated with equation (3.6).

Chapter 4

Characterisation of a state-insensitive dipole trap

The core of the results presented in this chapter was also published in P. Phoonthong, P. Douglas, A. Wickenbrock, and F. Renzoni, *Characterisation of a state-insensitive dipole trap for caesium atoms*, Phys. Rev. A. **82**, 013406 (2010).

4.1 Introduction

As discussed in the previous chapters, state-insensitive trapping can be realised by choosing the wavelength of the trapping laser field such that the AC Stark shifts of the ground and excited state of the addressed transition are equal. This constitutes a great advantage for the realisation of frequency standards. The trapped atom can be used to measure the clock transition without unwanted energy shifts, so to realise a frequency standard. The wavelength at which state-independent trapping is realised is termed the magic wavelength. However, for the microwave transition of caesium, the magic wavelength has been shown not to exist [72].

Another application for the magic wavelength is in quantum optics: the state-independent dipole trap allows one to precisely address the trapped atom without having to detune the laser to compensate for the light shift.

In this chapter, I will first describe the experimental setup of my magic wavelength dipole trap and then the measurements of the trap frequencies which lead to the beam waist or the trap size. Moreover, the trap lifetime is measured for different ground states so as to determine the role of hyperfine changing collisions. Other relevant loss mechanisms are also identified.

4.2 Experimental setup

The experimental setup is shown in figure 4.1. In our experiment, the caesium atoms are captured by a standard magneto-optical trap (MOT) in a glass cell. The MOT lasers consist of a cooling laser which is red-detuned with respect to the cooling transition ($F_g = 4 \rightarrow F_e = 5$) and a repumping laser tuned to the $F_g = 3 \rightarrow F_e = 4$ transition. Another laser, used to prepare the atoms in the lower ground state, is tuned to the $F_g = 4 \rightarrow F_e = 3$ D_2 line transition.

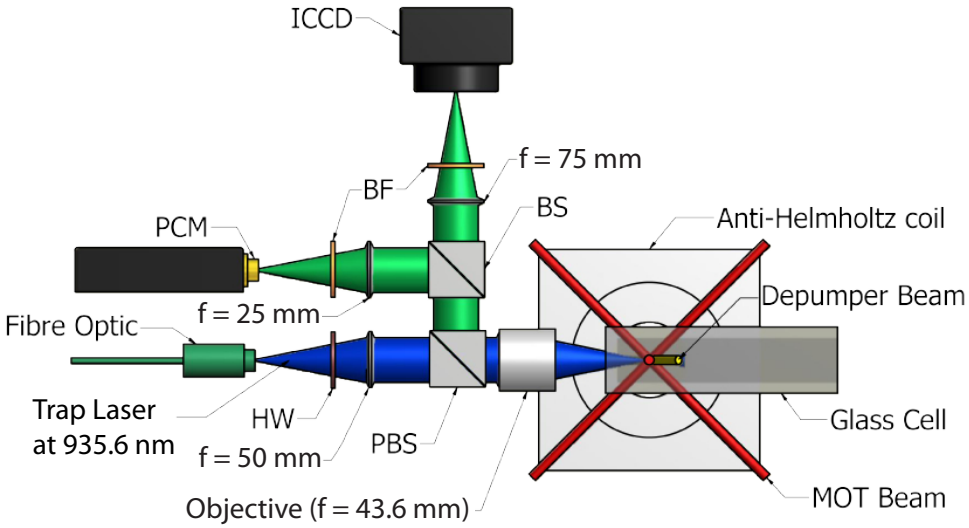

Figure 4.1: Experimental setup. ICCD is an intensified charge-coupled device camera, PCM is a photon counting module, BF is a bandpass filter, PBS and BS are a polarising and a normal beam splitter, and HW is a half waveplate.

A Ti-sapphire laser (Coherent MBR-110 pumped by a Verdi-V8) is used to provide the linearly-polarised trapping beam which is tuned to the magic wavelength for the $6S_{1/2}$ ground state to the $6P_{3/2}$ excited

state at 935.6 nm. The beam is transported close to the glass cell by using an optical fiber, and directly focussed on the atomic cloud using an objective lens. The objective lens used in the experiment (details in section 3.4.1), which follows the design of ref. [66], has a focal distance of 43.6 mm and we directly measured (see section 4.3.2) a beam waist of $\omega_0 = (6.69 \pm 0.05)$ μm at the focal point through a sample of the glass cell.

The experimental sequences start with the MOT loading process. The MOT is loaded from the background vapour for 5 s, such a long loading time being due to a low caesium background pressure in the system. The low background pressure is a requirement for a long lifetime of the dipole trap. After the MOT loading, the dipole trap beam is turned on and left on during the trapping phase and imaging phase. Simultaneously to the turning on of the dipole trap beam, the detuning of the cooling beam will be ramped from $-2.5\Gamma_{3/2}$ to $-4\Gamma_{3/2}$ and also the magnetic field gradient is increased from 22.5 G/cm to 30 G/cm in 10 ms. During the overlapping phase, the MOT and the dipole trap are run simultaneously for 50 ms to load the Cs atoms from the MOT into the dipole trap. During the trapping phase, the MOT beams and the magnetic field are switched off and the atoms are held in the dipole trap for a variable time (trapping time). Finally in the imaging phase, the fluorescence imaging of atoms in the trap is carried out by turning on the MOT beam (but not the magnetic field) which is tuned in resonance with the cooling transition. The ICCD camera is then used to collect the fluorescence of the trapped atoms for 4 ms.

4.3 Characterisation

4.3.1 Temperature measurement

The temperature is experimentally measured by the time-of-flight method (TOF). The thermal cloud in the trap is released by turning off all laser beams and also the magnetic field. As a result, the cloud starts to fall and expand due to the kinetic energy of the atoms. The temperature of the atoms is then determined by measuring the expansion velocity. In an ideal gas, which follows the Boltzmann distribution, the

relation between the mean velocity of the gas ($\bar{v}$) and the temperature (T) is

$$\bar{v} = \sqrt{\frac{k_B T}{m}}. \tag{4.1}$$

In the time of flight method, the Gaussian width (w) of the freely expanding atomic cloud is measured by taking fluorescence images for different falling times. The thermal cloud expansion follows [46]:

$$w^2(t) = w^2(0) + \frac{k_B T}{m} t^2. \tag{4.2}$$

In our experiment, the MOT temperature is also measured to optimise the loading of the dipole trap. The temperature of the MOT without optical molasses is T_x = (102±4) μK and T_y = (57±3) μK while the application of optical molasses can reduce it to T_x = (34±1) μK and T_y = (28±1) μK. Once the atoms are loaded into the dipole trap, the temperature is measured at different times in the dipole trap as shown in figure 4.2.

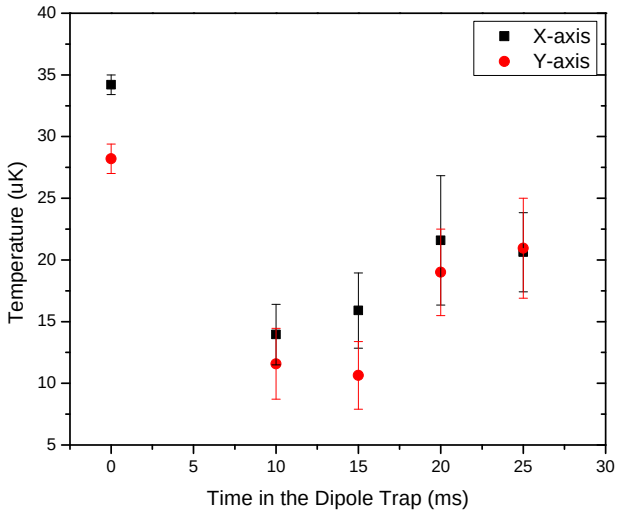

Figure 4.2: Temperature as a function of the trapping time, for a trap depth of U_0/k_B = -1.44 mK. The initial MOT temperature after the molasses phase is located at 0 ms.

As a result of a small trap depth, high temperature atoms cannot be trapped, so the average temperature of the trapped atoms is lower

than the MOT temperature. However, the red-detuned dipole trap can still heat the trapped atoms via heating mechanisms (see section 4.3.6). From graph 4.2, the temperature measurement was limited by the lifetime because the noise increases as the number of atoms decreases.

4.3.2 Beam waist measurement

The accurate measurement of the beam waist is essential to determine the trap depth. A standard technique; a razor blade set up on a two direction translation stage, is used to measure the beam waist. The transmitted light is monitored as the blade is moved across the beam. The unblocked power is given by

$$P(r) = I_0 \int_{r_0}^{\infty} e^{\frac{-2r^2}{w^2}} dr, \tag{4.3}$$

where I_0 is the peak intensity of the beam and r is the position of the razor blade across the beam. In order to integrate equation (4.3), we split it into two parts:

$$\begin{aligned} P(r) &= I_0 \left(\int_{r_0}^{0} e^{\frac{-2r^2}{w^2}} dr + \int_{0}^{\infty} e^{\frac{-2r^2}{w^2}} dr \right) \\ &= I_0 \frac{w_0}{\sqrt{2}} \left(- \int_{0}^{r_0} e^{\frac{-2r^2}{w^2}} dr + \frac{\sqrt{\pi}}{2} \right). \end{aligned} \tag{4.4}$$

We integrate by substituting $u^2 = \frac{-2r^2}{w^2}$ and the integral $\int_{\infty}^{0} e^{-u^2} du = \frac{\sqrt{\pi}}{2}$. Finally it can be simplified to the function which we use to fit the data:

$$P(r) = A \left\{ 1 - Erf \left(\frac{\sqrt{2}}{w} r_0 \right) \right\}, \tag{4.5}$$

where A is a constant, Erf is the error function and w is the beam waist. On the other hand, we can differentiate equation (4.3), thus obtaining the Gaussian function.

$$\frac{dP(r)}{dr} = I_0 e^{\frac{-2r^2}{w^2}} \tag{4.6}$$

The differentiated data are then fitted with a Gaussian function. The beam waist can then be determined as the Gaussian width (w).

To measure the minimum beam waist (w_0), the beam waists from the

different axial positions of a razor blade are measured and linearly fitted to a graph of the beam waist vs. the axial position. The minimum beam waist position is given by:

$$w^2(z) = w_0^2 \left(1 + \left(\frac{z}{z_R}\right)^2\right), \tag{4.7}$$

where $z_R = \pi w_0^2/\lambda$ is the Rayleigh length of the beam.

At positions far from the focal point ($z >> z_R$), equation (4.7) can be simplified to:

$$w(z) \approx w_0 \frac{z}{z_R} = \frac{\lambda}{\pi w_0} z. \tag{4.8}$$

The slope of the plot of the beam waist ($w(z)$) vs. the axial razor blade position (z) is approximately $\frac{\lambda}{\pi w_0}$.

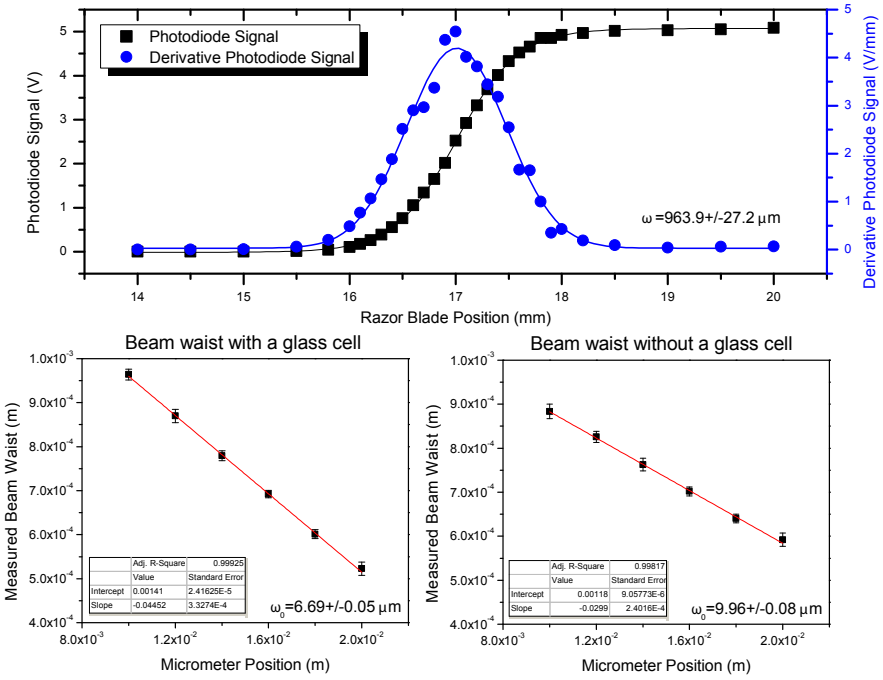

Figure 4.3: Top: measurement of the dipole trap beam waist. Bottom figure is plot of w vs. axial razor blade position. A linear fit gave the minimum waist at the focus: without a glass cell ($w_0 = 9.96 \pm 0.08$) μm and with a glass cell ($w_0 = 6.69 \pm 0.05$) μm.

In figure 4.3, the black data is the unblocked power as a function of axial position and the blue data is the derivative of the black data. The

black data is fitted with the error function of equation (4.5) while the blue data is fitted with the gaussian function of equation (4.6).

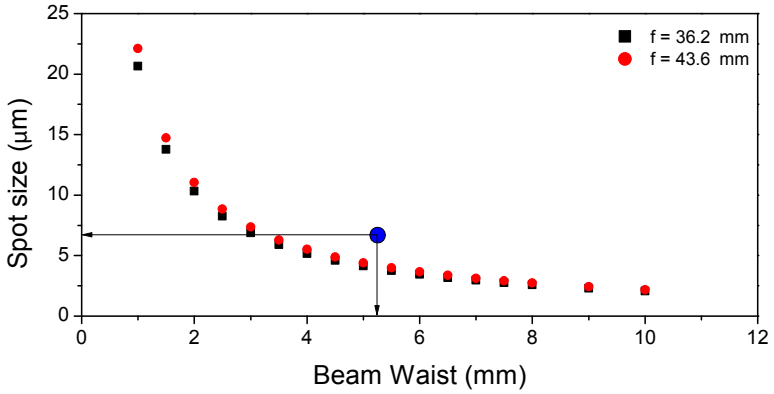

Figure 4.4: Calculated spot size as a function of the beam waist for two different focal lengths of the objective lens. The blue point is the experimental result of the beam waist of 5.24 mm which produces a spot size of 6.69 μm.

Our objective lens had a focal length of 43.6 mm. Ideally, the spot size from the beam waist of 5.24 mm should be around 4.76 μm. However, the measured spot size of 6.69 μm was slightly larger than the calculated value. A possible cause could be a non-collimated beam and a small angle of the beam. One solution may be a fine-adjustment fiber optic mount which possibly collimates the beam and also tilts the angle of the beam. Another improvement may be an enlargement of the beam waist or a shorter focal length objective (f = 36.2 mm) which can help to reduce the spot size as shown in figure 4.4.

4.3.3 Trap frequencies

An important technique frequently used to characterise a dipole trap is parametric excitation [37, 73]. Normally, a parametric measurement gives an excitation spectra with frequency ω, where ω is the natural oscillation frequency of the atoms in the trap [74, 75]. As the parametric excitation is related to the vibrational frequency, the trapping size or the beam waist (w_0) can be calculated.

In a classical harmonic potential, when the trapping beam is closely modulated at twice the trap frequency ($2\omega_{r,z}$) or at a subharmonic fre-

quency $(2\omega_{r,z}/n)$, with n integer, the energy of the oscillating atom will exponentially increase. The atoms are heated up and expelled from the trap. In the case of a single focussed laser beam, the AC Stark shift potential can be written as

$$U(r,z) \approx U_0 \left[1 - 2\left(\frac{r}{w_0}\right)^2 - \left(\frac{z}{z_R}\right)^2\right], \tag{4.9}$$

where z is the axial direction, r is the radial axis, and z_R is the Rayleigh length $z_R = \pi\omega_0^2/\lambda$. The potential is usually approximated by a harmonic oscillator potential

$$U(r,z) = \frac{m\omega_r^2 r^2}{2} + \frac{m\omega_z^2 z^2}{2}. \tag{4.10}$$

From equation (4.9) and (4.10), the vibrational frequencies can be calculated as

$$\omega_r = \sqrt{\frac{-4U_0}{m\omega_0^2}} \tag{4.11}$$

$$\omega_z = \sqrt{\frac{-2U_0}{mz_R^2}}. \tag{4.12}$$

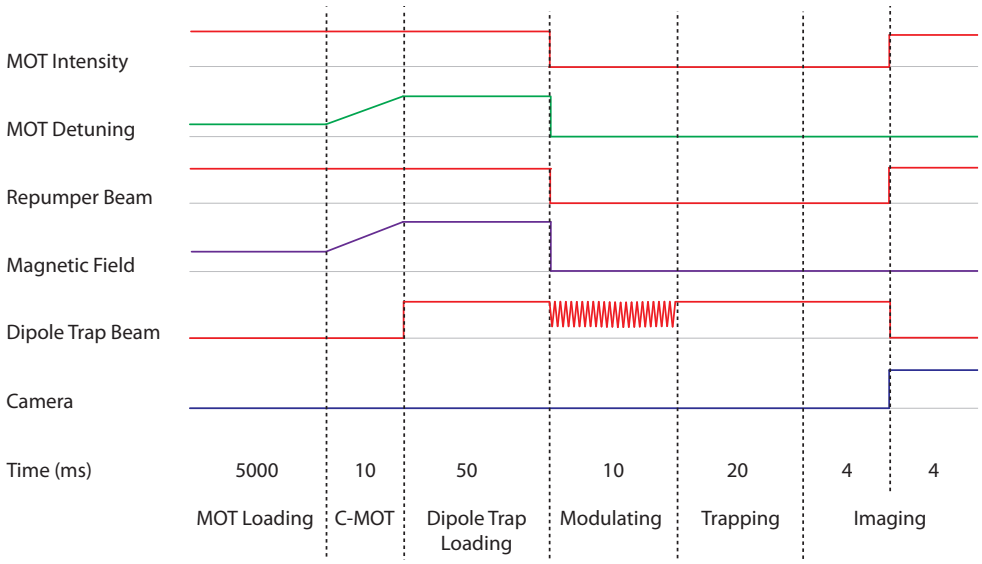

Figure 4.5: Time sequence for the vibrational frequency measurement.

To determine the trap frequency, the intensity of the trapping beam was modulated at a frequency ω during the trapping phase for 10 ms

and then the atoms were left in the trap for another 20 ms before the imaging phase as shown in figure 4.5. A Pockel cell was then setup to be able to quickly change the power of the trapping beam by rotating the angle of linear polarisation of the beam before a polarising beam splitter. Modulating the intensity of the laser beam can be achieved easily by applying a high voltage sine wave to the Pockel cell. For the low frequency modulation (less than 500 Hz), the beam amplitude modulation is 50%, and 15% for the high frequency modulation (more than 500 Hz).

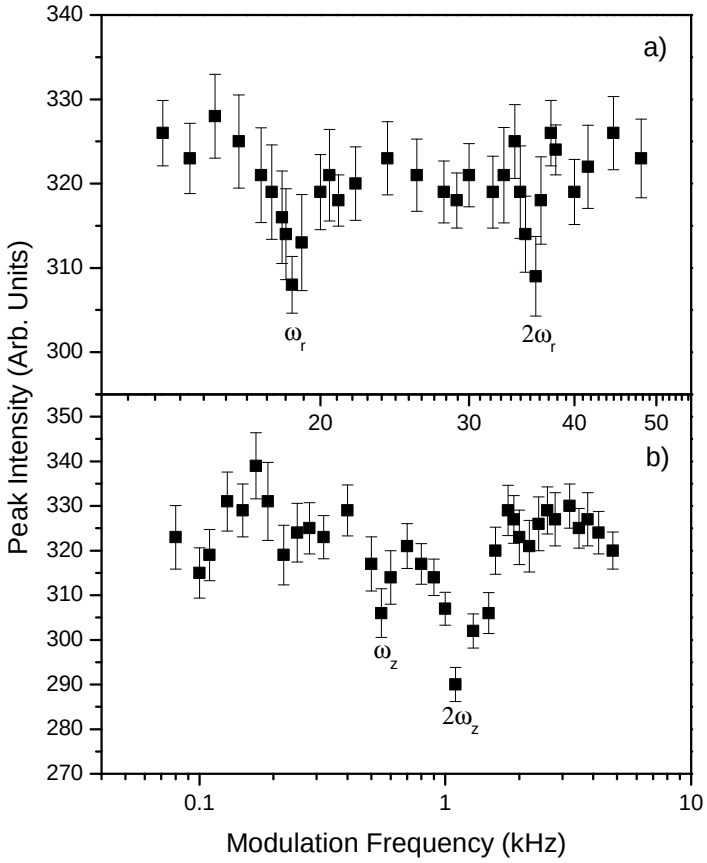

Figure 4.6: Parametric heating of Cs atoms in a dipole trap at the magic wavelength, as measured by the peak fluorescence intensity. The intensity is reported as a function of the trapping beam modulation frequency. Graph in (a) shows the excitation spectra for the radial axis and graph in (b) for the longitudinal axis.

Our results are shown in figure 4.6, for both the axial and radial frequencies. A more sensitive method [76], consisting of measuring the peak density rather than the total number of trapped atoms, is used to measure a decrease in the number of atoms left in the trap. We observed a peak intensity drop at the parametric heating both at the fundamental frequency ($\omega = 2\omega_{r,z}$) and at the first sub-harmonic frequency ($\omega = \omega_{r,z}$).

From the presented data in 4.6a) and b), the vibrational frequencies for radial and axial axis were obtained as $\omega_r/2\pi$ = (18.5±0.1) kHz and $\omega_z/2\pi$ = (550±10) Hz respectively. The power of trap beam is (254±2) mW for data in 4.6a) and (231±1) mW for data in 4.6b), so the beam waist can be calculated from equation (4.11) and (4.12). We computed the beam waist of ω_0 = (6.63±0.04) μm from the radial axis frequency and ω_0 = (6.67±0.02) μm from the axial axis frequency. Both values are consistent with our direct measurement of the beam waist ω_0 = (6.69±0.05) μm

4.3.4 Trap lifetime

Another important parameter of the dipole trap is its lifetime. The lifetime of the atoms in a far-detuned dipole trap is directly described via a loss rate equation. To determine the lifetime, the number of atoms is recorded as a function of the trapping time. The data are then fitted to the following equation [37, 77]:

$$\frac{dN}{dt} = -\Gamma N - \beta N^2, \tag{4.13}$$

where Γ is the exponential loss rate, and β is the two body collisional coefficient. The lifetime τ can be derived from the fitted value of Γ as $\tau = 1/\Gamma$.

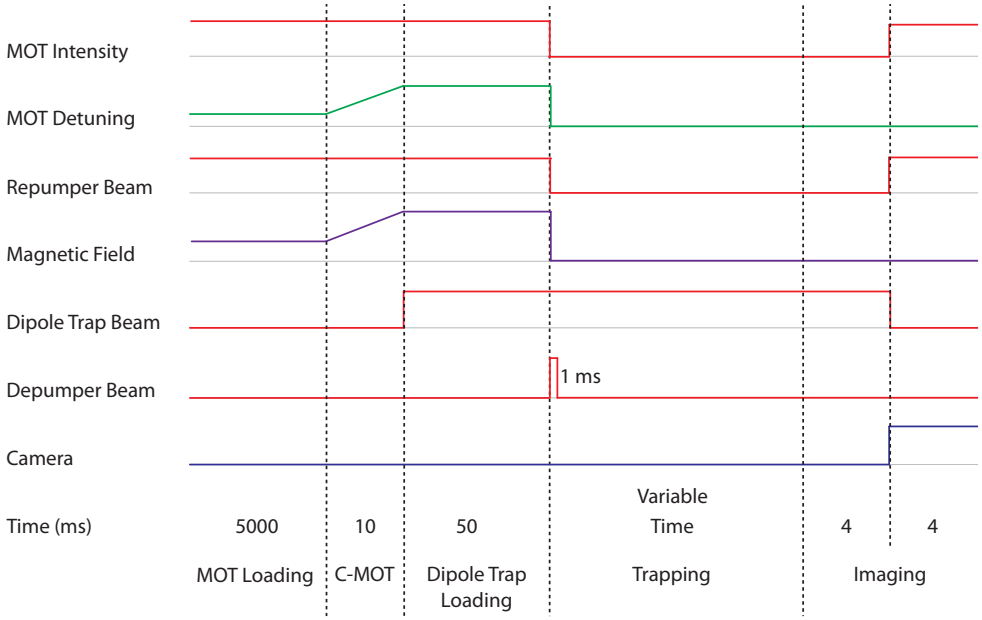

Figure 4.7: The time sequence for the lifetime measurement.

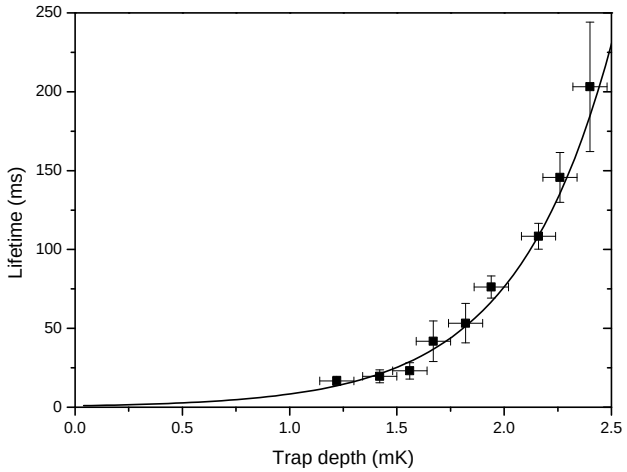

Figure 4.8: Lifetime as a function of the trap depth. The data were taken without the application of a depumper. The line is a guide for the eye.

Following such a procedure, we studied the lifetime of the trap as a function of the trap depth with results as in figure 4.7. The trap depth is easily changed by varying the intensity of the trapping beam. We found that the lifetime increases with the trap depth, as the results in figure 4.8 show. The trap depth is limited by the laser power available

in the experiment. Our Ti-sapphire laser can provide a maximum power of around 900 mW at 935.6 nm. However it is necessary to couple it to a fiber optic to obtain a clean Gaussian beam profile, although this introduces significant losses. The final power after the fiber optic and the glass cell is 393 mW which corresponds to a trap depth of U_0/k_B = -2.4 mK and a lifetime of (203±41) ms. The results in figure 4.8 refer to the case without a depumper. We expect a longer lifetime when the atoms are pumped into the lower hyperfine ground state ($F_g = 3$).

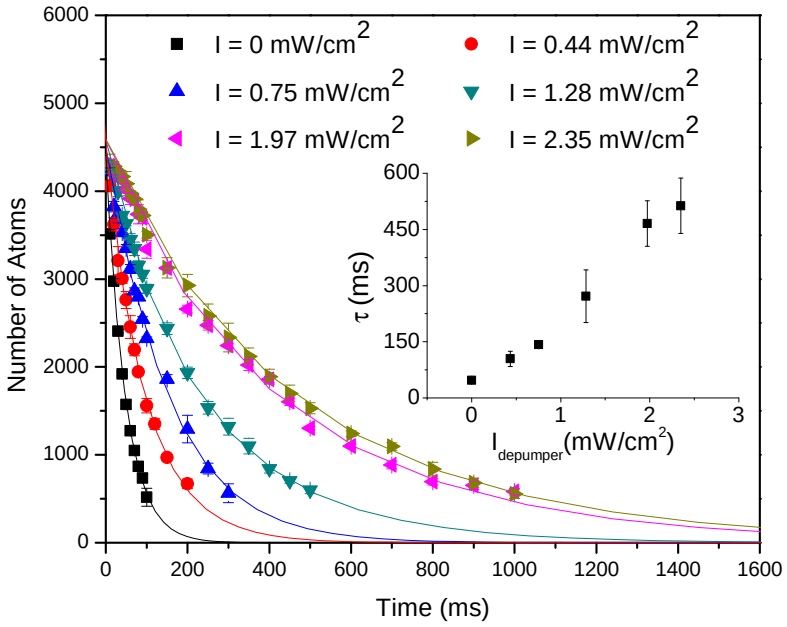

Figure 4.9: Atom number decay for different depumper intensities. The lines are the best fits of the data with equation (4.13).

A previous study for a far-detuned trap at 1064 nm showed that the lifetime of the trapped atoms significantly depends on the atomic state [37]. A long lifetime was observed for the atoms prepared in the lower hyperfine ground state ($F_g = 3$) as the dominating loss mechanism is collisions with the background gas. On the other hand, for atoms prepared in the upper hyperfine ground state ($F_g = 4$), hyperfine changing collisions is the dominating loss mechanism. This leads to a shorter lifetime.

Therefore, we introduced a depumper laser to prepare the atoms in the lower ground state by varying the intensity of the depumper beam to optimise the lifetime. During the trapping phase, the depumper is switched on for the first 1 ms of the trapping phase to prepare the atoms

in the lower ground state. Once the atoms are in the lower ground state ($F_g = 3$), we need to use the repumper laser ($F_g = 3 \rightarrow F_e = 4$) for the imaging phase so to pump atoms into the upper ground state ($F_g = 4$) to be able to detect the number of atoms left in the trap by illuminating the $F_g = 4 \rightarrow F_e = 5$ transition. The results, shown in figure 4.9 for the trap depth U_0/k_B = -1.78 mK, illustrate the expected increase of the lifetime for increasing intensity of the depumper beam.

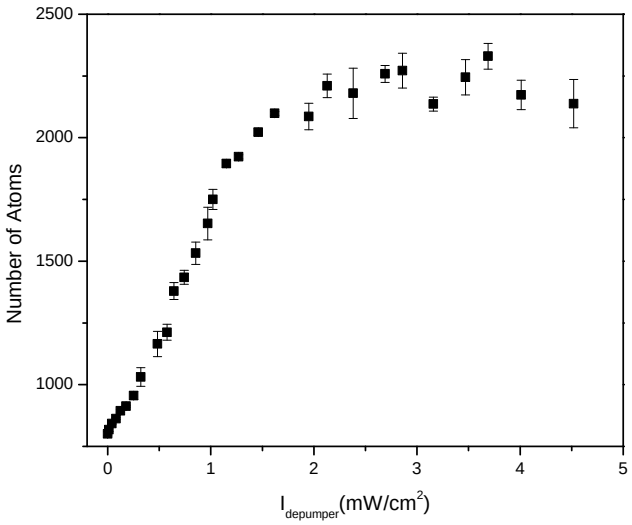

Figure 4.10: The number of atoms left in the trap after 100 ms trapping time as a function of the depumper intensity. The trap depth is U_0/k_B = -1.52 mK.

From figure 4.9, an appropriate intensity of the depumper is essential to prepare the atoms into the $F_g = 3$ level and obtain a long lifetime. A saturation effect is to be expected for an intensity of the depumper that is high enough to prepare all trapped atoms in the desired state. This was confirmed by measuring the number of atoms left in the trap after 100 ms trapping time for a variable intensity of the depumper beam. The result is reported in figure 4.10 which clearly evidences the expected saturation effect. The number of atoms increases with depumper intensity and then becomes constant for $I_{dep} \approx 2$ mW/cm^2

Finally, we have observed the longest lifetime in our system for a trap depth of U_0/k_B = -2.4 mK and a depumper intensity of $I_{dep} = 1.32$ mW/cm^2. We have measured the lifetime of $\tau = (3.6 \pm 0.4)$ s with the ap-

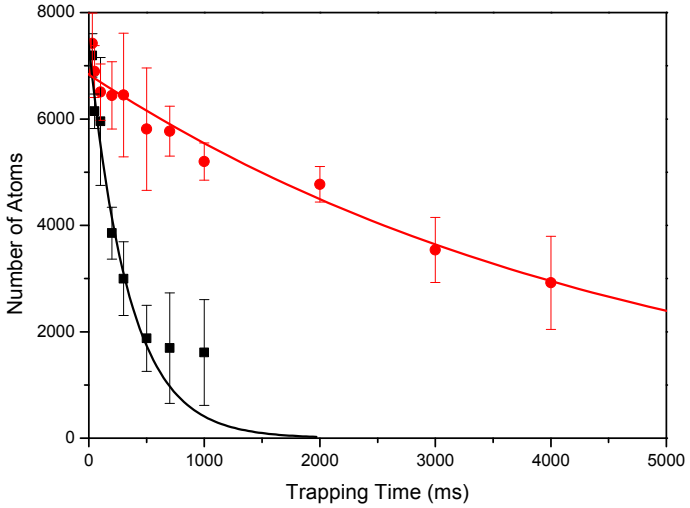

Figure 4.11: The decay curve for a trap depth of U_0/k_B = -2.4 mK with (filled red circles) and without (filled black squares) depumper. The data with the application of the depumper are fitted by a single exponential equation (red line). The data without the application of the depumper are fitted by equation (4.13) (black line).

plication of the depumper which is fitted by a single exponential equation due to the suppression of the hyperfine changing collisions. The lifetime of τ = (203±14) ms without the depumper is fitted by equation (4.13) because of the presence of the hyperfine changing collisions. According to our result in figure 4.11, the lifetime without the depumper is reduced by about one order of magnitude. These results show the effect of the hyperfine changing collisions for the case of the atoms prepared in the upper hyperfine ground state.

4.3.5 Comparison with other wavelengths

We also studied trapping of atoms for a wavelength of the trapping beam around the magic wavelength (928 - 941 nm). This allows us to experimentally verify that the trap at the magic wavelength is state-insensitive. Our Ti-sapphire laser can be widely tuned to the wanted wavelength. The depumper laser was locked to the crossover transition ($F_g = 4 \rightarrow F_e = 3/4$) which is blue-detuned from the $F_g = 4 \rightarrow F_e = 3$ transition by about 100 MHz. In order to pump atoms into the lower ground state, the depumper frequency had to be shifted by an acousto-optic modulator (AOM) to be on resonance with the $F_g = 4 \rightarrow F_e = 3$

transition which was shifted due to the AC Stark shift.

In order to experimentally determine the AC Stark shift produced by the trapping light, we make use of the results presented in the previous section about the effect of a depumper which showed that the atoms in the lower hyperfine ground state have a longer lifetime. Hence the number of atoms left after 100 ms as a function of the depumper detuning from the resonance transition was studied for the different trapping light wavelength. We expect that the number of atoms will be a maximum at the depumper resonance with the AC Stark shifted $F_g = 4 \rightarrow F_e = 3$ transition. So the depumper detuning at the maximum number of atoms left in the trap will correspond to the differential AC Stark shift for that wavelength.

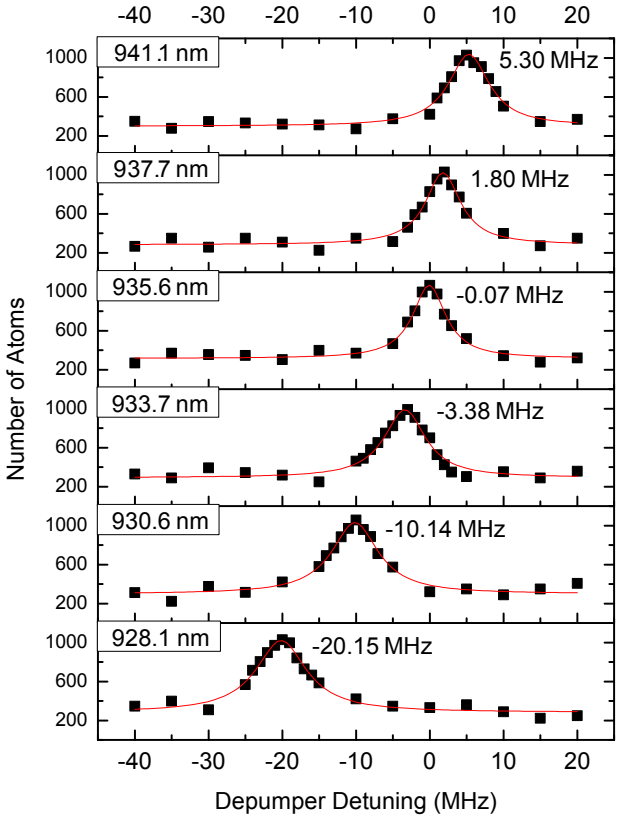

Figure 4.12: The number of atoms left in the trap after 100 ms as a function of the detuning of the depumper laser for different wavelengths of the trapping beam. The trap depth is $U_0/k_B = -1.25$ mK.

Figure 4.12 shows our experimental results for the number of atoms left in the trap after 100 ms as a function of the detuning of the depumper light. The data was fitted to a Lorentzian and the peak of each fitting curve was taken as the differential AC Stark shift of the $F_g = 4 \rightarrow F_e = 3$ D_2 line transition.

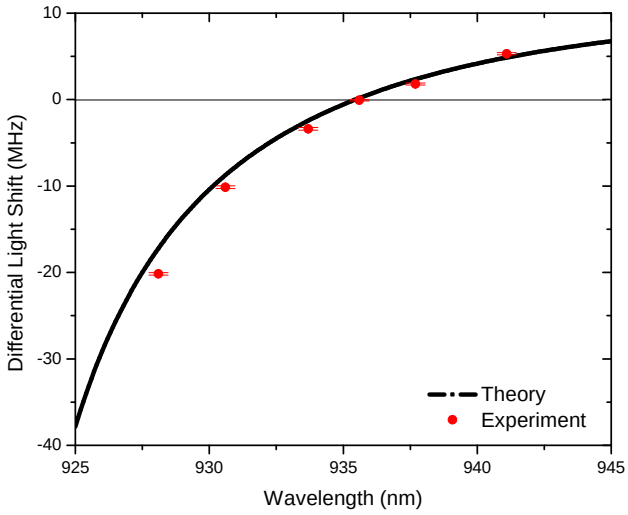

Figure 4.13: Experimental results (data points) and theoretically expected values for the differential light shift of the D_2 line transition of Cs. The trap depth is U_0/k_B = -1.25 mK.

In figure 4.13, we compare the experimental data for the differential AC Stark shift as a function of the trap beam wavelength to the theoretical value as calculated from chapter 2. In the calculation, we neglected the (m,F) dependence of the light shift of the $6P_{3/2}$ state, and reported only the differential shift of the D_2 line. Our results in figure 4.12 and 4.13 confirm the state-independent nature of the trapping at the magic wavelength (λ = 935.6 nm) as, for that wavelength, the differential AC Stark shift is zero within experimental error.

4.3.6 Trap loss mechanisms

Several processes may limit the lifetime of a dipole trap. In this section, the following processes will be considered in order to identify the main loss mechanism during the trapping phase: recoil heating [78, 79], intensity fluctuations [78, 79], pointing instabilities [78, 79], dipole force fluctuations [78, 79], and collisions with the background gas [80].

Recoil heating

We consider first heating due to spontaneous scattering of trap photons [37]. At far-detuning, the heating corresponds to an increase of the thermal energy by the recoil energy $E_{rec} = k_B T_{rec}/2$ per scattering event. The heating rate is directly linked to the average photon scattering rate by

$$\dot{Q}_{rec} = 2E_{rec}\Gamma_{sc} = k_B T_{rec}\Gamma_{sc}. \tag{4.14}$$

The scattering rate (Γ_{sc}) is related to the total potential experienced by atoms. In the optical dipole trap, the atoms experience the dipole trap potential (U_0) and the thermal energy ($\frac{3}{2}k_B T$). In case of a red-detuned dipole trap ($\Delta < 0$) and tight confinement ($U_0 >> \frac{3}{2}k_B T$), the scattering rate can be approximated as [37]:

$$\begin{aligned} \Gamma_{sc} &= \frac{\Gamma}{\hbar\Delta}(U_0 + \frac{3}{2}k_B T) \\ &\approx \frac{\Gamma}{\hbar\Delta}U_0. \end{aligned} \tag{4.15}$$

This recoil heating causes trap losses, and the trap lifetime can be derived to be [79]:

$$\tau = \frac{U_0}{2.2\dot{Q}_{rec}}. \tag{4.16}$$

The calculated lifetime for the trap depth of -2.4 mK is in excess of 100 s for the entire range of the considered wavelength of around 925 - 945 nm. The longest lifetime in our trap with the depumper beam is 3.6 s, so we can conclude that the recoil heating is not the main loss mechanism which determines the lifetime of our trap.

Intensity fluctuations heating

In a far-off resonance red detuned trap, the fluctuations in the spring constant caused by the laser intensity fluctuation can lead to exponential heating [78, 79]. To derive the heating rate, the Hamiltonian for a trapped atom can be written as

$$H = \frac{p^2}{2M} + \frac{1}{2}M\omega_{trap}^2(1+\epsilon(t))x^2, \tag{4.17}$$

where $\omega_{trap}^2 = \frac{k_0}{M}$ is the trap frequency, k_0 is proportional to the averaged laser intensity I_0 and $\epsilon(t) = \frac{I(t)-I_0}{I_0}$ is the fractional fluctuation in the laser intensity. The heating rate is determined by using the first-order perturbation theory to calculate the average transition rates between quantum states of the trap [78, 79]. The perturbation Hamiltonian is given by

$$H'(t) = \frac{1}{2}M\omega_{trap}^2 x^2\epsilon(t). \tag{4.18}$$

The transition rate of the perturbation Hamiltonian (4.18) for an atom in the state $|n\rangle$ to the state $|m \neq n\rangle$ is described as

$$R_{m\leftarrow n} \equiv \frac{1}{T}\left|\frac{-i}{\hbar}\int_0^T dt' H'_{mn}(t')e^{i\omega_{mn}t'}\right|^2 \tag{4.19}$$

$$= \left(\frac{M\omega_{trap}^2}{2\hbar}\right)^2 \int_{-\infty}^{\infty} d\tau e^{i\omega_{mn}\tau}\left\langle\epsilon(t)\epsilon(t+\tau)\right\rangle \left|\left\langle m\left|x^2\right|n\right\rangle\right|^2 \tag{4.20}$$

where x^2 can be expressed in terms of creation and annihilation operators and the fluctuation term can be defined as a one-sided power spectrum:

$$\langle m\left|x^2\right|n\rangle = \frac{\hbar}{2M\omega}\langle m\left|(a^\dagger a^\dagger + 2a^\dagger a + aa)\right|n\rangle \tag{4.21}$$

$$S(\omega) = \frac{2}{\pi}\int_0^\infty d\tau\cos(\omega\tau)\langle\epsilon(t)\epsilon(t+\tau)\rangle. \tag{4.22}$$

By substituting equations (4.21) and (4.22), and also $\omega_{mn} = 2\omega_{trap}$ into equation (4.20), the transition rates are then written as

$$R_{n\pm2\leftarrow n} = \frac{\pi\omega_{trap}^2}{16}S_\epsilon(2\omega_{trap})(n+1\pm1)(n\pm1). \tag{4.23}$$

The heating rate is then given by

$$\begin{aligned}\left\langle \dot{E} \right\rangle &= \sum_n P(n) 2\hbar\omega_{trap}(R_{n+2\leftarrow n} - R_{n-2\leftarrow n}) \\ &= \frac{\pi}{2}\omega_{trap}^2 S_\epsilon(2\omega_{trap}) \left\langle E \right\rangle , \end{aligned} \tag{4.24}$$

where $P(n)$ is the probability that the trapped atoms occupy state $|n\rangle$, and $\langle E\rangle$ is the average energy given by $\langle E\rangle = \sum_n P(n)(n+1/2)\hbar\omega_{trap}$. The lifetime then can be described as the e-folding time (the time to increase the energy by a factor e) which is given by:

$$\tau_{trap}^{-1} = \pi^2 \nu_{trap}^2 S_\epsilon(2\nu_{trap}), \tag{4.25}$$

where $S_\epsilon(\nu)$ is the one-sided power spectrum of fractional fluctuations in the laser intensity at frequency (ν).

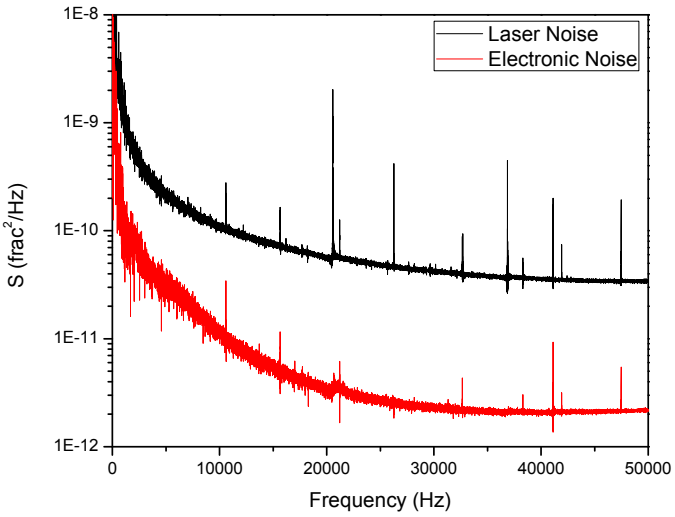

Figure 4.14: The one-sided power spectrum of fractional fluctuations in the intensity of the dipole trap laser at 935.6 nm is shown in black and the electronic noise is presented in red.

The laser noise intensity was directly measured by a photodiode after the fiber optic. The fractional fluctuation ($\epsilon(t)$) was then derived as $\epsilon(t) = \frac{I(t)-I_0}{I_0}$, where I_0 is the average photodiode voltage over the measured time. The electronic noise measurement was done in an enclosed box to protect the photodiode from the light. Using these data,

the power spectral density (PSD) was then calculated by a fast Fourier transform (FFT) method. From the one-sided power spectrum in figure 4.14, we measured the longitudinal noise with the trap frequency (ν_z) of 720 Hz as $S_\epsilon(1440) \approx 1.5 \times 10^{-9}$ Hz^{-1} and the radial noise with $\nu_r =$ 22.8 kHz as $S_\epsilon(45600) \approx 3.6 \times 10^{-11}$ Hz^{-1}. By using equation (4.25), the lifetime can be evaluated by an average e-folding time for each axis: for axial axis $\tau_r = 5.4$ s and for radial axis $\tau_z = 130$ s.

The e-folding time for axial axis is significantly larger than the observed lifetime in our experiment. On the other hand, the fluctuation of the laser intensity in the radial axis can cause a major heating mechanism in our trap.

Pointing instability heating

Another sources of heating is the pointing instability of the trap beam [78, 79]. The beam pointing fluctuations affect the location of the trapping potential which can cause a fluctuation in the trap equilibrium position. The Hamiltonian of the system is described as

$$H = \frac{p^2}{2M} + \frac{1}{2}M\omega_x^2(x - \epsilon(t))^2, \tag{4.26}$$

where $\epsilon(t)$ is the fluctuation in the pointing location of the trap centre. To calculate the heating rate, we follow the same method as in the previous case of *Intensity Fluctuations Heating*. The perturbation Hamiltonian is

$$H'(t) = -M\omega_x^2 x\epsilon(t). \tag{4.27}$$

By using the rate equation (4.19), the transition rate of the perturbation Hamiltonian (4.27) is given by

$$\begin{aligned} R_{m\leftarrow n} &= \left(\frac{M\omega_{trap}^2}{2\hbar}\right)^2 \int_{-\infty}^{\infty} d\tau e^{i\omega_{mn}\tau}(2\left\langle\epsilon(t)\epsilon(t+\tau)\right\rangle \\ &\quad |\langle m\,|x|\,n\rangle|^2). \end{aligned} \tag{4.28}$$

By substituting equation (4.22) and $\omega_{mn} = \omega_{trap}$ into equation (4.28), the transition rates are then written as

$$R_{n\pm1\leftarrow n} = \frac{\pi}{2\hbar}M\omega_x^3 S_\epsilon(\omega_x)(n + \frac{1}{2} \pm \frac{1}{2}). \tag{4.29}$$

Hence, the heating rate is

$$\dot{Q}_x \equiv \left\langle \dot{E}_x \right\rangle = \sum_n P(n) 2\hbar\omega_x (R_{n+1\leftarrow n} - R_{n-1\leftarrow n}) = \frac{\pi}{2} M\omega_x^4 S_x(\omega_x), \tag{4.30}$$

where S_x is the one-sided power spectrum of the position fluctuation and ω_x is the x-axis vibrational frequency. The lifetime is then derived to be [79]:

$$\tau = \frac{U_0}{6.6\dot{Q}}. \tag{4.31}$$

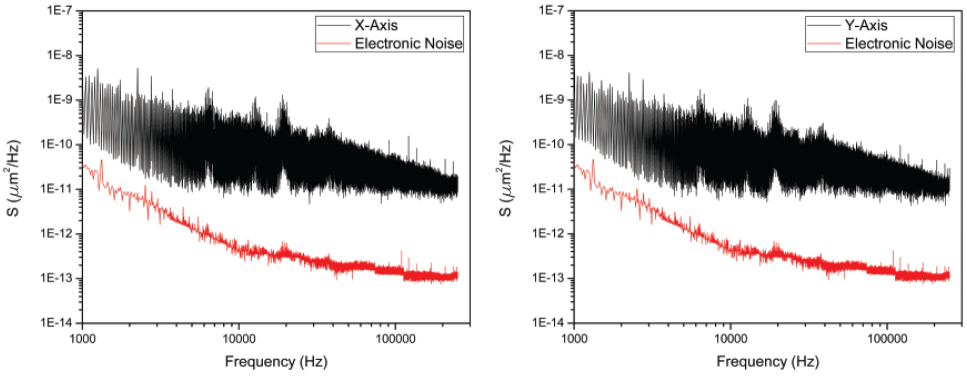

Figure 4.15: One-sided power spectrum of fluctuation in the pointing stability of the dipole trap laser at 935.6 nm.

Figure 4.15 shows our measurements for the pointing instability of the laser beam, taken by a quadrant photodiode. These data can determine only the pointing stability in the radial plane due to the 2D structure of a quadrant photodiode. A quadrant photodiode consists of four photodiodes arranged in four quadrants of a circular structure. All photodiodes are connected to a circuit to compare the intensity for each part of the beam on the photodiode. In order to measure the pointing instability, we have to initially calibrate the quadrant photodiode. The quadrant photodiode was mounted on a fixed construction and the dipole trap beam was mounted on a XYZ translation stage used in the experiment. First of all, we have to set the output signal from the quadrant photodiode to be null by an alignment of the beam so that the four photodiodes receive the same amount of light.

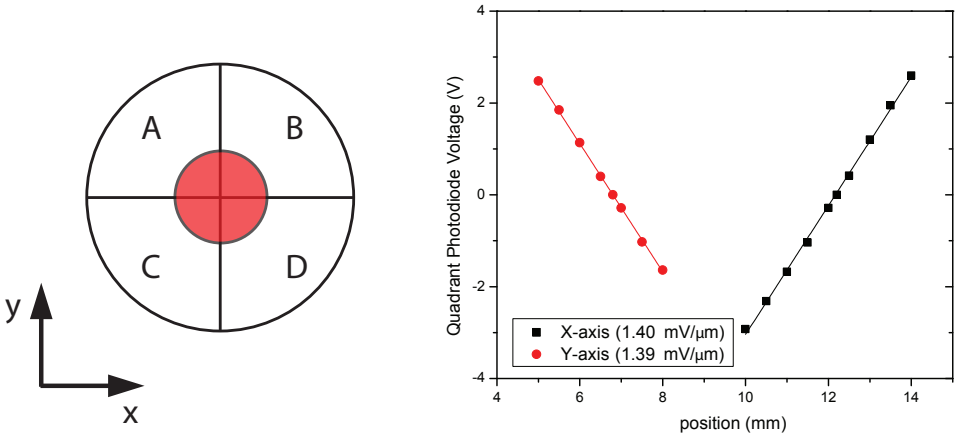

Figure 4.16: A quadrant photodiode for measuring the beam movement and the calibration graph of the beam position vs. the output voltage for both axes.

The output of the quadrant photodiode consists of two signals:

$$\begin{aligned} X &= \frac{(V_A + V_C) - (V_B + V_D)}{(V_A + V_B + V_C + V_D)}, \\ Y &= \frac{(V_A + V_B) - (V_C + V_D)}{(V_A + V_B + V_C + V_D)}. \end{aligned} \tag{4.32}$$

This output is the measurement of the beam displacement in the X and Y direction, respectively, and the sign of each signal indicates the direction of displacement. To get an accurate measurement, the laser beam should have a Gaussian profile. In order to read out the beam position from the quadrant photodiode, the output signal has to be calibrated as a function of the displacement distance for the X-axis and Y-axis. The position of the dipole trap beam on the quadrant photodiode is changed by the XYZ translation stage. This leads to an unbalance in the power on it. As from figure 4.16, the displacement of 1 μm corresponds to an output voltage change of $\sim$ 1.4 mV for both X and Y axis. This calibration is then used to convert the signal to the displacement of the beam; the quantity required to measure the pointing instability.

The black line in figure 4.15 is the power spectral density of the pointing fluctuation, measured while all mechanical shutters for the experiment were operating. The red line is the electronic noise which records the output signal without measuring the light. This can be done in the enclosure box to prevent the light from entering the photodiode. We obtained the noise at the radial trap frequency for the x-axis as $S_x((2\pi)22.8$ kHz$) = 1.2 \times 10^{-11}$ μm^2/Hz and the y-axis as $S_y((2\pi)22.8$ kHz$) = 1.2 \times 10^{-11}$ μm^2/Hz. To calculate the corresponding lifetime, we used equations (4.30) and (4.31). From the graph, the expected lifetime is about 4.3 s which is comparable to the lifetime of our experiment of 3.6 s. This shows that the beam-pointing instability is a limiting factor for our trap lifetime.

Fluctuation in the dipole force

An atom in a dipole trap experiences force from two sources: the radiation pressure and the dipole force [81]. A change of an internal atomic energy level can induce a fluctuation in the dipole force due to the differential AC Stark shift.

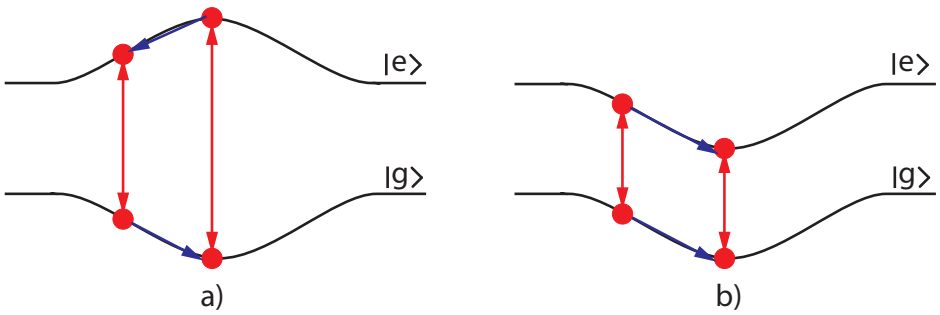

Figure 4.17: The AC Stark shift diagram shows the general dipole trap in a), while the state-insensitive dipole trap is presented in b).

For a general two-level atom in a dipole trap, the ground and excited states are generally shifted in the opposite directions, as shown in figure 4.17a). The atoms then experience a different energy shift depending on the position of the atoms in the trap. The excited atoms in different positions can have different momentum transfer, leading to momentum diffusion. The diffusion coefficient of atomic momentum can be expressed

as [81]:

$$D_{dipole} = \frac{\hbar^2}{2\Gamma}\left(\frac{\chi_{g,e}^2}{\chi_{g,e}^2 + 2\delta^2}\right)^3 (\nabla\chi_{g,e})^2, \tag{4.33}$$

where Γ is the natural linewidth, $\chi_{g,e}$ is the Rabi frequency between the ground state ($|g\rangle$) and the excited state ($|e\rangle$) of the atom in the trap, δ is the detuning between the trap laser and the atomic transition and $\nabla\chi_{g,e}$ is the gradient of the Rabi frequency due to the dipole trap.

In the case of figure 4.17a), the gradient of the Rabi frequency ($\nabla\chi_{g,e}$) becomes dominant with respect to the differential energy shift, so the momentum diffusion can affect the lifetime of the trapped atoms. However, the large detuning (δ) in a far-off resonance trap can also reduce the momentum diffusion.

For the state-insensitive dipole trap in figure 4.17b), the gradient of the Rabi frequency can be ignored due to the same shift of the ground and excited state. So the momentum diffusion does not occur in this trap. However, the calculation in figure 2.6 reveals that the AC Stark shift of the excited state depends on the m_F state. Thus the trapped atoms can still experience a small gradient of the Rabi frequency for different m_F states.

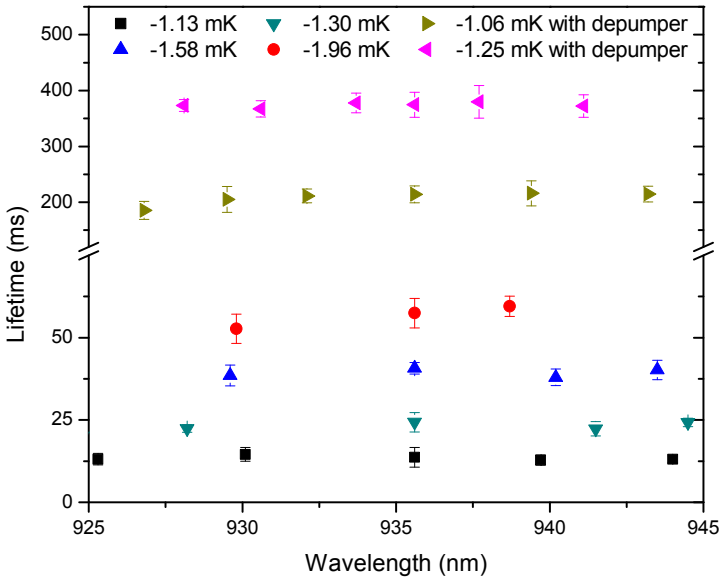

Figure 4.18: The lifetime of the atoms as a function of the wavelength for different trap depths and different intensities of the depumper beam.

Figure 4.18 shows the lifetime of the dipole trap at different trapping

wavelengths around the magic wavelength. A depumper beam is applied on resonance with the light shifted $F_g = 4 \rightarrow F_e = 3$ D_2 line transition. We did not observe any increase in lifetime around the magic wavelength (935.6 nm). Due to the low photon scattering rate in the far off resonance trap, the momentum transfer becomes small, so the momentum diffusion can be ignored. This graph shows that the fluctuation in the dipole force is not an important loss mechanism for our dipole trap.

Collisions with background gas

The energy transfer in the process of background gas collisions results in the heating of an atom [80]. For a single collision, the loss mechanism can cause an atom to heat up and leave the trap depending on the angle of collision and the trap depth. The finite trap depth is an upper bound for the energy transfer that can still result in heating but not in the loss of an atom. The loss of the trapped atoms by the background gas collisions is given by [80]

$$\dot{N} = -N n_b \langle v(Q - \Delta Q) \rangle_{T_b} = -N/\tau, \tag{4.34}$$

where Q is the elastic cross section, n_b is the background density and τ is the lifetime. The cross section ΔQ is related to the heating of the trapped atoms for all angles of collision. It can be written as

$$\begin{aligned} \Delta Q &= \int_0^{\theta_{max}} \sigma(\theta) 2\pi \sin(\theta) d\theta \\ &\approx \frac{Q}{2\cos^2[\pi/(s-1)]} \int_0^{x_{max}} F(x;s) x dx, \end{aligned} \tag{4.35}$$

where $F(x;s)$ is the model function for the small-angle differential cross section ($\sigma(\theta)/\sigma(0)$) in ref. [80]. A very accurate semi-empirical representation of the model function is written as

$$F(x;s) = [1 - c_1(s)\sin[c_2(s)x^2] + c_3(s)x^2]^{-(s+1)/s}, \tag{4.36}$$

where $x_{max} = \sqrt{U_0/U_{ref}}$, and the constants for the induced dipole-dipole interaction of atom-atom scattering ($s = 6$) are equal to $c_1(6) = 3.75$, $c_2(6) = 0.556$ and $c_3(6) = 2.94$. To estimate the background pressure of the system, we calculate the pressure of the system with the

equation (4.34) by using the parameters in ref. [80].

According to the experimental data, the longest lifetime at a trap depth of -2.4 mK is 3.6 s, corresponding to a background gas pressure of P = 3.4 $\times$ 10^{-9} mbar. This value is within the range of pressures expected for a single-cell experiment. Collisions with the background gas are thus also a limiting factor for our trap lifetime.

4.4 Conclusions

I have experimentally characterised our state-insensitive dipole trap. The magic wavelength at 935.6 nm produces the same AC Stark shift for the ground state $6S_{1/2}$ and the excited state $6P_{3/2}$. The single trapping beam is produced by an objective lens (f = 43.6 mm) which can focus the beam to a waist of 6.69 μm. At the maximum power of our Ti-sapphire laser, I produced a trap with a depth of -2.4 mK and a lifetime of (203$\pm$41) ms. By introducing a depumper laser to prepare the atoms into the lower hyperfine ground state, I reduced the hyperfine changing collisions and measured a lifetime of (3.6$\pm$0.4) s, the longest lifetime we measured in our setup. I analysed in detail the loss mechanisms in the trap, and concluded that the trap lifetime is limited by the beam pointing instability and the collisions with the background gas.

Chapter 5

Upgrade of the experiment towards a 1D optical lattice

As shown in the previous chapter, the lifetime of our dipole trap is limited by the collisions with the background gas and the pointing instability of the trapping beam. Further problems of the experimental setup were the long-term power instability of the Ti-sapphire laser and the amount of stray light in the imaging path. To overcome these problems, the experimental apparatus was upgraded. First, a new vacuum system was assembled to reduce the pressure in the science cell. Next, the Ti-sapphire laser was replaced by a Master Oscillator Power Amplifier (MOPA) system. Finally, the imaging system was improved to be able to detect fewer atoms with a better signal-to-noise ratio. This chapter documents and characterises the changes made to improve the system in detail.

5.1 New vacuum system

To improve the vacuum, and thus increase the lifetime of the atoms in the dipole trap, I designed a new vacuum system in which the atomic source and the dipole trap are in two different chambers. The double MOT system consists of the atomic source chamber and the science chamber as shown in figure 5.1.

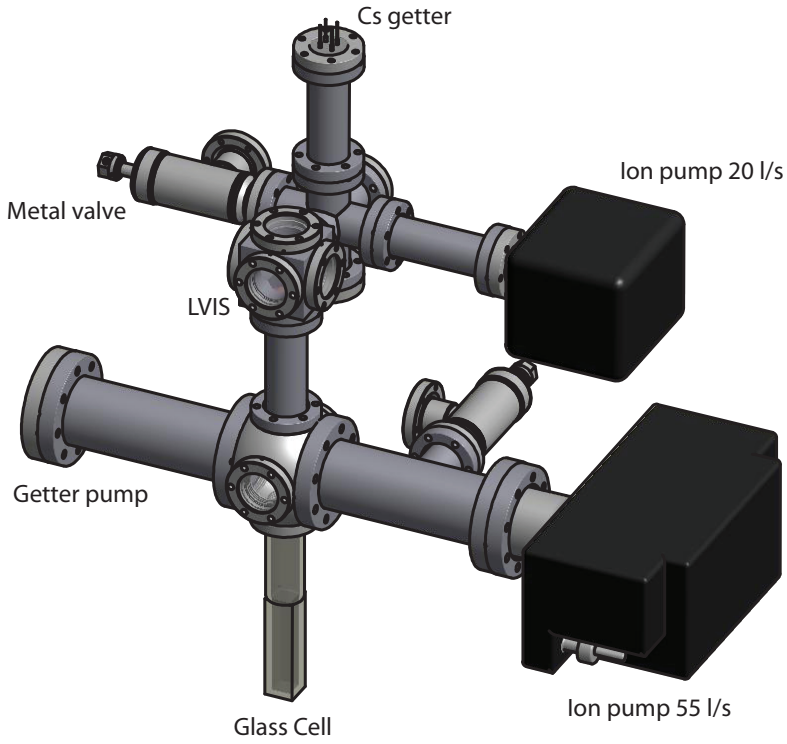

Figure 5.1: The layout of the double MOT system

In the new design, the vacuum components of the single MOT system from the previous setup were used as the atomic source chamber (see figure 3.18). But instead of the glass cell, a six-way cube was installed. This part contained the so-called Low-Velocity Intense Source of Atoms (LVIS), described in the next section. One side of the cube is connected to a double-sided blank flange with a small hole. This part acts as a channel for cold atoms and a differential pumping stage. It separates the relatively high pressure region of the LVIS from the new low pressure science chamber providing longer trap lifetimes for the experiment.

The pressure in the science chamber is maintained by two vacuum pumps: an ion pump[1] and a non-evaporable getter (NEG) pump[2]. Both pumps are attached to a spherical square connector[3]. The glass cell was placed opposite to the cold atom channel. The whole construction is vertically mounted on an optical table so that the science glass cell rests about 14 cm above the surface. This ensures maximum optical

[1]Varian StarCell 55 l/s
[2]SAES Getters GP 100 MK 5
[3]MCF450-SphSq-E2C4 from Kimball

access, mechanical stability and good overlap of the atomic beam with the science MOT.

5.1.1 LVIS

Several atomic sources suitable to load a MOT have been developed in the last twenty years: the Zeeman slower, the 2D MOT and the LVIS. A Zeeman slower is the most intense source of slow atoms and provides a flux up to 10^{11} atoms/s [82]. However, its disadvantage is its large size, the high stray magnetic fields generated and the high background of thermal atoms. 2D MOT and LVIS use pre-cooled atoms as atomic sources.

I implemented an LVIS system similar to the one described in ref. [83]. An LVIS is similar to a standard MOT setup but one of the retro-reflecting mirrors and corresponding waveplate is placed in the vacuum chamber and has a small hole at the centre. Due to the imbalance in radiation pressure on that axis, a continuous cold atomic beam is extracted from the MOT [84].

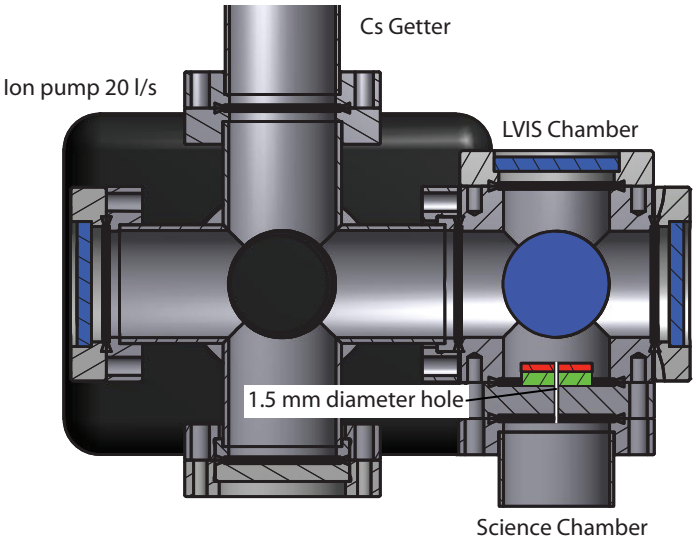

Figure 5.2: Cross section of the LVIS chamber.

Our LVIS chamber in figure 5.2 was constructed from a cube[4] and 5 uncoated viewports[5]. A 20 l/s ion pump was connected to maintain

[4]E-CU150-6 from MDC Caburn
[5]Zero Length 304L CF40 viewports from VG Scienta

a pressure below 10^{-8} mbar. An electric feedthrough is connected to a pair of Cs dispensers providing a background gas of thermal atoms to load the LVIS. A pair of anti-Helmholtz coils set up on the viewports along the axis perpendicular to the plane of figure 5.2 creates a gradient of $\sim$ 8 G/cm at 3.2 A. The standard three retro-reflected laser beams for the MOT have a waist of $\sim$10 mm and a power of $\sim$15 mW per beam providing a peak intensity of $\sim$9.5 mW/cm^2. 2 mW of repumping light is added and overlapped with the MOT beams. A beam of cold atoms from the LVIS is then extracted via a 1.5 mm hole in the mirror (green in figure 5.2) and the quarter waveplate (orange) to load the science chamber MOT. Both optical elements were glued onto the double-sided blank flange with a low outgassing vacuum glue[6].

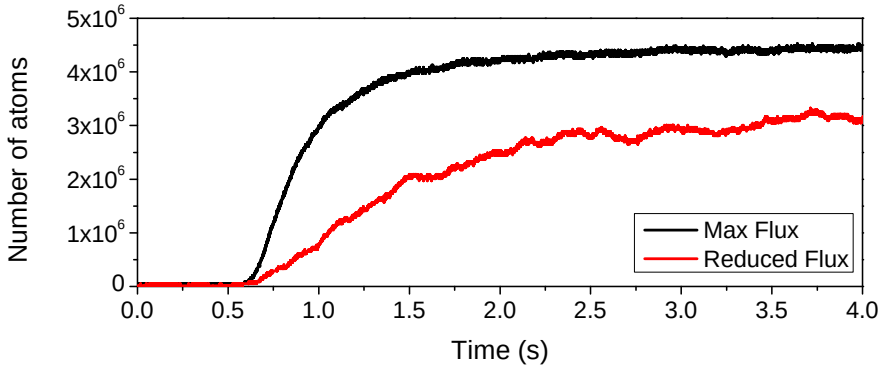

Figure 5.3: The atomic flux of the LVIS is measured by monitoring the loading of the science MOT. The LVIS is switched on at 0.6 s. The maximum flux of 9×10^6 atoms/s is measured at a magnetic field gradient of 8 G/cm (black line). By reducing the gradient to 4 G/cm, the LVIS can provide a flux of 1.7×10^6 atoms/s (red line).

The atomic flux from the LVIS can be characterised by measuring the loading time of the science MOT. By optimising the position of the LVIS with respect to the hole, the flux could be maximised to around 9×10^6 atoms/s as shown in the black data of figure 5.3. On the other hand, this flux can be easily reduced by decreasing the magnetic field gradient. Figure 5.3 (red line) shows that by reducing the gradient to 4 G/cm a reduced flux of 1.7×10^6 atoms/s was produced.

[6]Torr Seal from Varian

5.1.2 Pressure measurement

The pressure in the science cell can be monitored via the ion pump current or obtained from the MOT lifetime. However, the ion pump current reached the minimum limit and could not display a pressure below 2.5×10^{-10} mbar. Another method to measure the pressure inside the science cell is via the lifetime of the MOT. The MOT decay time relates to the background pressure since the collisions between the background gas atoms and the trapped atoms can cause losses. The loss coefficient is defined as

$$\Gamma_M = \frac{1}{\tau_M} = n_{\mathrm{b}}\sigma_{\mathrm{b}}\bar{v}_{\mathrm{b}} + n_{\mathrm{Cs}}\sigma_{\mathrm{Cs}}\bar{v}_{\mathrm{Cs}}, \tag{5.1}$$

where τ_M is the MOT lifetime, n_{b} and n_{Cs} are the densities of background gas, σ_{b} and σ_{Cs} are the collisional cross sections between atoms in the trap and the background and $\bar{v}_{\mathrm{b}}$ and $\bar{v}_{\mathrm{Cs}}$ are the average velocities of background gas. The subscripts indicate the type of the background gas: (b) is other gases and (Cs) is the caesium atoms.

We can assume that the amount of caesium (n_{Cs}) in the science cell is far more than other background atoms (n_{b}). Also, the collision cross section of Cs-Cs[7] is bigger than the collision with other background atoms for example Helium [85]. Therefore the collisions between the trapped caesium and the hot caesium background are the dominant loss mechanisms. In the science cell with a pressure of P, the density and the mean kinetic energy of the background gas obey the ideal gas laws [85]:

$$P = n_{\mathrm{Cs}}k_B T, \tag{5.2}$$

$$\bar{v}_{\mathrm{Cs}} = \sqrt{\frac{8k_B T}{\pi m_{\mathrm{Cs}}}}. \tag{5.3}$$

By substituting n_{Cs} and $\bar{v}_{\mathrm{Cs}}$ into equation (5.1), the pressure is then written as

$$P = \frac{1}{\tau_M \sigma_{\mathrm{Cs}}}\sqrt{\frac{\pi m_{\mathrm{Cs}} k_B T}{8}}. \tag{5.4}$$

The pressure in the science chamber can be calculated from the MOT lifetime. The MOT lifetime can be determined by monitoring the exponential decay of the MOT fluorescence when the atomic source is shut.

[7] $\sigma = 2\times10^{-17}\ m^2$ for Cs-Cs collisional cross section [85].

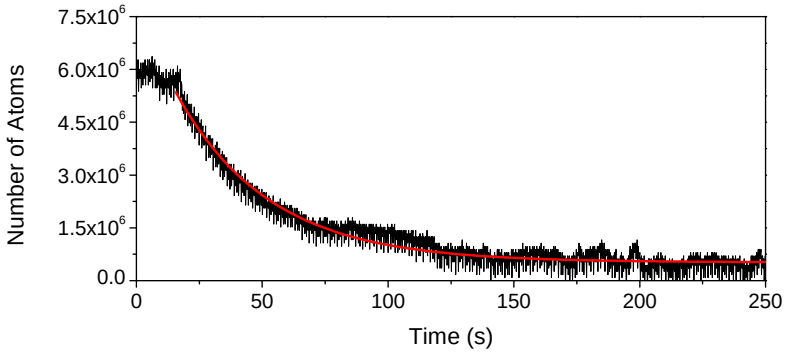

Figure 5.4: The decay of the MOT was measured after the LVIS was shut. The red line is the best fit with an exponential decay. The lifetime of the MOT is (36.5±0.6) s which corresponds to a pressure of (2.6±0.1)×10^{-10} mbar.

As shown in figure 5.4, the exponential decay time of the MOT in the new vacuum system is (36.5±0.6) s. By using equation (5.4), we estimated the pressure in the science chamber to be around (2.6±0.1) × 10^{-10} mbar. This pressure can now be used to determine the limitation on the dipole trap lifetime due to the collisions with the background gas. In the previous single cell vacuum system, the pressure in the science cell was around 3×10^{-9} mbar which corresponds to a maximum lifetime of around 3.6 s for a trap depth of 2.4 mK. By separating the atomic source, the pressure in the science cell can be significantly reduced. The maximum lifetime of the new apparatus is estimated from equation (4.34) to be around 50 s for the same trap depth.

5.2 Dipole trap laser improvement

The Ti-sapphire laser used in the previous setup showed large long term power instability, which made the operation of the experiment difficult. As a result of this, we decided to replace it with a MOPA system, which is a valid alternative to generate high power laser radiation with a wavelength around 935 nm. In our setup, we use a GaAs based tapered amplifier (TA). The output spectrum of the amplifier is very broad (∼ 10 nm) but it can be narrowed by injecting it with an external laser. The chip itself consists of two gain regions: a pre-amplifier stage and an amplification stage (see figure 5.5). The pre-amplifier region is a small rectangular area, with dimensions 5 × 1.4 μm, acting as a spatial filter

for the seed laser. In this way, only the TEM_{00} mode is amplified. The amplification region is a tapered area with a big output facet (256 × 1.4 μm), so that the intensity in the gain medium does not reach the destruction threshold even for high power outputs. Both chip facets are treated with an anti-reflection coating of less than 0.01% reflection to avoid laser action of the amplifier chip itself.

5.2.1 Design

The design of the MOPA construction is shown in figure 5.5. The beam is focussed into the pre-amplifier region by a lens (f = 8.0 mm) with a high numerical aperture [8] (NA = 0.5). Due to spatial constraints in the output beam path, the working distance of the collimating lens had to be longer[9]. Both lenses are held on robust Fiber Launchers[10] which allow fine adjustment in five degrees of freedom (X, Y, Z, θX, θY).

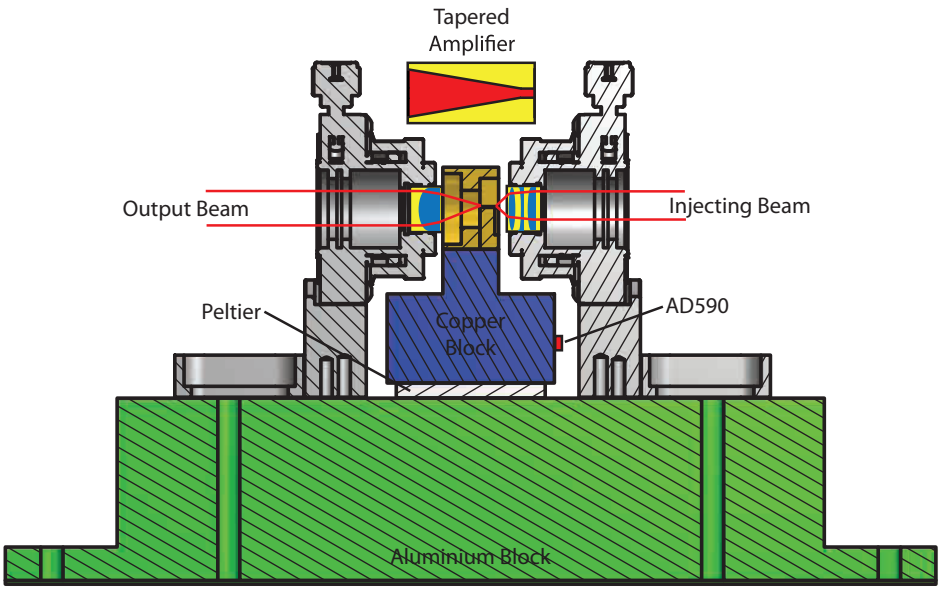

Figure 5.5: Design of the MOPA construction. The small figure shows the details of the tapered-amplifier chip.

The semiconductor gain profile is temperature sensitive therefore the TA chip has to be temperature stabilised to guarantee stable operation.

[8] GLC-8.0-8.0-830 from Melles Griot
[9] C240TME-B from Thorlabs, working distance: 5.92 mm.
[10] Model 9095 from New Focus

A copper block is used to increase thermal inertia. Its temperature is sensed by an AD590 and controlled with a peltier element[11]. The heat is transferred into the large aluminium base plate acting as a heat sink. A commercial feedback circuit[12] provides stabilisation. The TA current is supplied by a commercial laser diode controller[13]. It can provide current up to 4 A with a noise level below 50 μA.

5.2.2 MOPA setup

The MOPA system is set up in a master-slave configuration, as shown in figure 5.6. It mainly consists of a seed laser and a single pass TA [86].

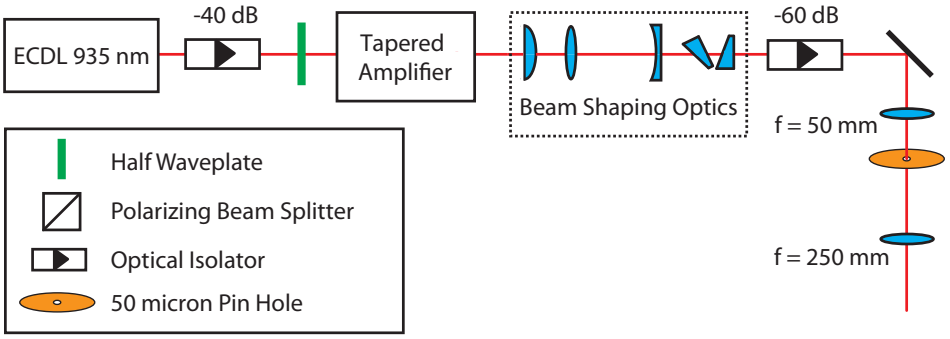

Figure 5.6: The laser schematics for the MOPA system.

A laser diode at 935 nm[14] is constructed in the Littrow configuration as the seed laser, emitting a maximum output around 50 mW. The beam then passes through a 40 dB optical isolator which prevents optical feedback into the laser diode. The output power of the TA for a given input intensity depends on the angle of the linear polarisation of the seed beam. Accordingly, a half waveplate is installed to be able to optimise the polarisation. Owing to the large tapered area, the output beam is much wider in the plane of the taper. The output aspheric lens collimates only the vertical axis of the beam, and the horizontal axis is collimated by an additional 100 mm cylindrical lens. After that its waist is reduced

[11]MCPE1-12707AC-S 55.6W from Multicomp
[12]PTC10K-CH 10A temperature control from Wavelength Electronics
[13]LDC240C from Thorlabs
[14]M9-935-0100-S50 common cathode laser diode at (935±5) nm from Axcel Photonics

by a 2:1 telescope and the profile made circular by an anamorphic prism pairs. Another 60 dB optical isolator is used to protect the MOPA from retro-reflected light. The beam is spatially filtered by a 50 μm pin hole and then expanded by a 1:5 telescope. Finally, the Gaussian beam with a beam waist of about 5.6 mm is focussed by the objective lens to create the micro dipole trap.

5.2.3 Characterisation

The output power of the TA depends on the chip current and the power of the seed laser. These relations were investigated, and the results are illustrated in figure 5.7.

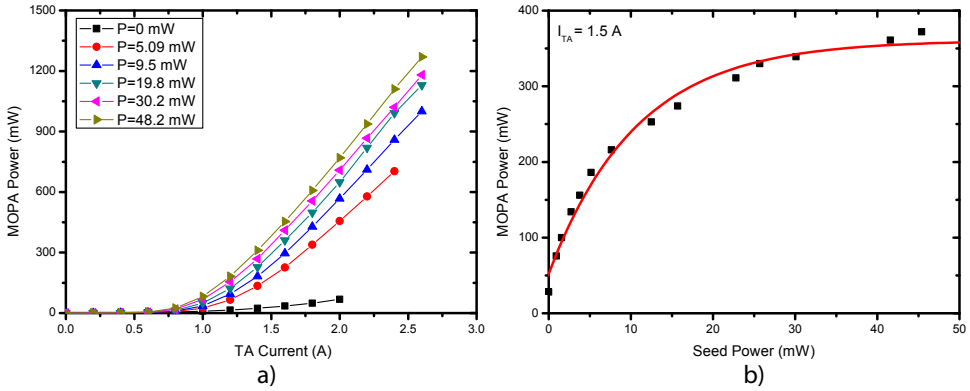

Figure 5.7: The MOPA output power as a function of the current is shown in a) and as a function of the seed power for a given current of 1.5 A in b). The data was taken for a chip temperature of 13.2 °C.

The TA can be operated at a maximum current of 2.8 A with the seed laser and at 2 A without the seed laser. The amplification threshold from figure 5.7a) is between 1 and 1.3 A depending on the seed power. An increase in the seed power not only increases the output power but also reduces the amplification threshold current. However, the TA output power saturates for a seed power around 30 mW, as can be seen in figure 5.7b).

By changing the temperature of the TA, the threshold current is changed which causes the change of the output power. A linear fit to the data in figure 5.8 shows that the output power increases by $\sim$ 16 mW/°C. To have the maximum output power, the chip temperature is

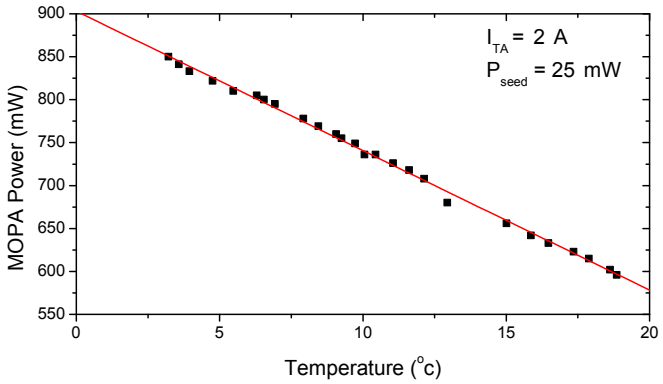

Figure 5.8: The MOPA output power as a function of the chip temperatures. The current of the TA was fixed at 2 A and the power of the seed laser was 25 mW.

reduced to slightly above condensation. To reduce the temperature further, the TA is placed in an enclosing box containing silica gel to reduce air humidity. For most experiments, the TA was operated at $T_{TA} \sim 10$ °C, $I_{TA} = 2.7$ A and $P_{seed} = 32$ mW which gave a maximum output power of ~ 1.2 W.

5.2.4 Dipole trap alignment

Overlapping the focussed dipole trap on the centre of the MOT is crucial to maximise the number of atoms loaded into the trap. The dipole trap and the MOT beam are aligned along the same axis due to the limitations of the optical access. The problem of using the same axis is that the MOT beam has to be collimated while the dipole trap beam must be focussed. Our solution is shown in figure 5.9.

The MOT beam is focussed by a f = 50 mm lens before it is collimated by the f = 36.1 mm objective. This reduces the waist of the MOT beam by a factor of 0.72 while the dipole trap beam is focussed by the same objective. A dichroic mirror[15] is used to combine both beams. It reflects the MOT beam at the wavelength of 852 nm and transmits the dipole trap beam at the wavelength of 935 nm. The objective and the dichroic mirror are constructed in a cage system to increase the stability. The whole construction is mounted on a XYZ translation stage with a micrometre scale allowing the fine adjustment of the dipole trap position.

[15]DMLP900R: Longpass Dichroic Mirror/Beamsplitter from Thorlabs

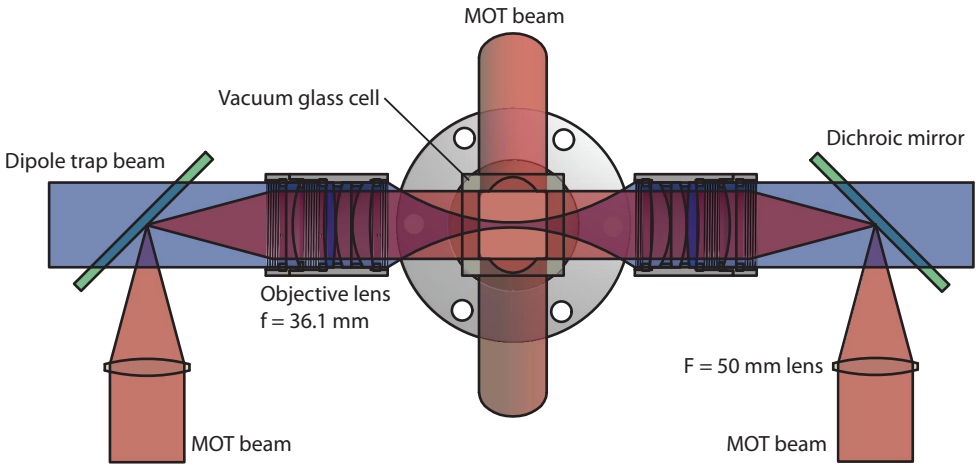

Figure 5.9: The bottom view of the system illustrates the overlapping of the dipole trap (blue beam) and the MOT beam (red beam). Both beams are combined at the dichroic filter which reflects the 852 nm light of the MOT beam and transmits the 935 nm dipole trap beam. This construction, which includes the objective and the dichroic filter, is mounted on the XYZ translation stage.

We adopted the following procedure to overlap the single focussed dipole trap beam onto the centre of the MOT:

1. The magnetic field of the LVIS is decreased to reduce the loading rate of the science MOT. We obtain in this way a small MOT which allows us a more precise overlap.

2. An additional on-resonant beam is brought via a fiber optic onto the same construction as the objective. The beam is then centered on the dichroic mirror and the objective.

3. The on-resonant beam is then focussed by the objective. Although the filter allows only 2% of the intensity to go through, its intensity is still high enough to produce a significant scattering force on the small MOT. By adjusting the translation stage, the MOT will be completely destroyed when the on-resonant beam coincides with the centre of the MOT.

4. The fiber optic is then removed and the dipole trap beam is then sent through the centre of the objective. The pan-tilt angle of the dipole trap beam is adjusted until the MOT disappears.

5. The magnetic field of LVIS is then increased to obtain a large MOT before the final adjustment is done by the fluorescence imaging. The translation stage is finely moved until the position of the dipole trap is at the centre of the MOT.

Once the single beam dipole trap is aligned, a 1D optical lattice can be easily produced by retro-reflecting the beam. The fluorescence image is then used to overlap two focussed beams to form the 1D optical lattice.

5.3 Imaging system improvement

Due to the high noise level which was observed by characterising the previous imaging system, we decided to design a new imaging system with the purpose of reducing the background noise. The setup of the new imaging system is illustrated in figure 5.10.

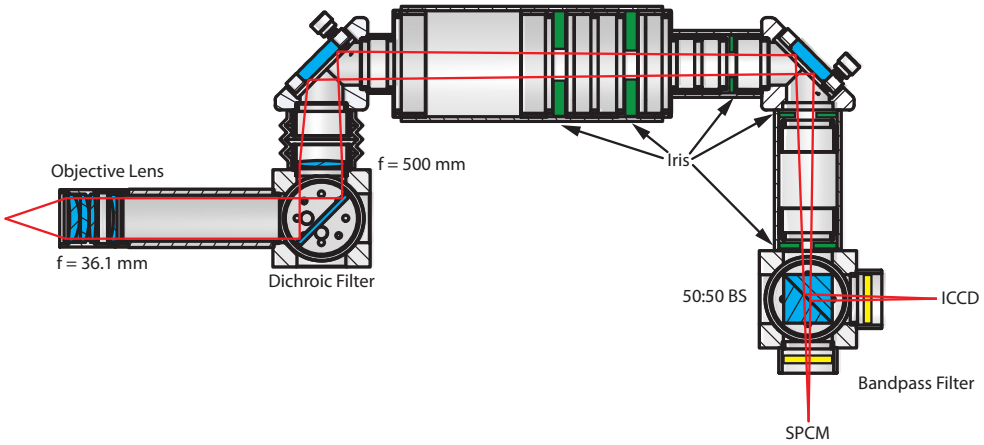

Figure 5.10: The schematic of the imaging system.

The objective with a focal length of 36.1 mm is used to collect the fluorescence light of the atoms (see details of the objective lens in section 3.4). The objective is mounted on a XYZ translation stage to be able to finely adjust the imaging position. On the translation stage, the dichroic mirror[16] reflects the atomic light at 852 nm (R = 97.3 %) and transmits the dipole trap light at 935 nm (T = 95.8 %). This allows us to use the same axis for the imaging beam and the dipole trap beam. After that a bi-convex lens with a focal length of 500 mm focusses the atomic

[16]DMLP900R: Longpass Dichroic Mirror/Beamsplitter from Thorlabs

fluoresence on the detector. The theoretical magnification of this lens system is $f_{img}/f_{obj} \sim 14$. The lens system is constructed inside a black plastic tube to suppress the background light. Furthermore, the out-of-focus light is blocked by 5 adjustable irises mounted at the position of 15, 19, 25, 29, and 35 cm from the focusing lens. At the end of the black tube, the light is split by a non-polarising beam splitter and sent through a bandpass filter[17] to filter all unwanted wavelengths. Finally the fluorescence of atoms is detected by the Intensifier CCD unit and the single photon counting module.

The atom number calibration for the new imaging system was done by following the same method described in section 3.4. The total transmission coefficient is given by table 5.1.

Optical elements	Transmission coefficient
Glass Cell (2X)	0.96^2
Objective Lens (8X)	0.995^8
Dichroic Mirror	0.973
Lens (2X)	0.995^2
Mirror (2X)	0.995^2
Beam splitter	0.5
Bandpass filter	0.52
Total	~ 0.22

Table 5.1: The intensity transmission coefficient for the new imaging system. The number in the bracket indicates the number of surfaces for each optical elements, for example (2X) indicates two surfaces.

The improved system increases the amount of photons on the detector due to the reduction of the number optical elements in the imaging path. Additionally, it reduces the background noise in the system as a result of the series of irises and the enclosure of the optical system in the black plastic tube.

[17] FB-850-10 from Thorlabs

5.3.1 Camera pixel calibration

To determine the trap waist, the pixel size of the ICCD camera has to be calibrated. Generally, atoms in the dipole trap are located at the focus of the trap. Since the objective was placed on a XYZ translation stage, this provided fine adjustment in the axial and radial position. Therefore, by moving the objective focus with a micrometre scale, the pixel position of the dipole trap on the camera could be changed. The displacement of the translation stage and the pixel displacement on ICCD were plotted to perform the calibration as shown in figure 5.11.

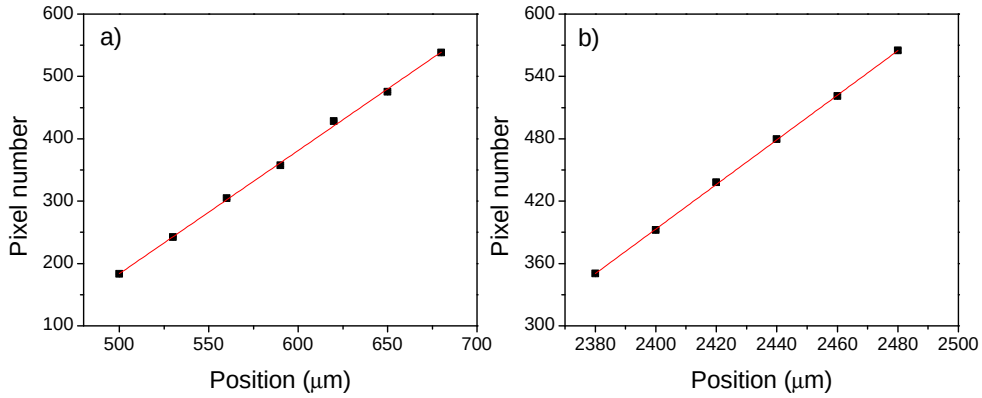

Figure 5.11: Pixel size calibration of ICCD by imaging the dipole trap cloud after 50 ms holding time. The pixel position was determined by fitting Gaussian distributions to images. The calibration of the axial direction in a) is (0.51 ± 0.01) μm/pixel and of the radial axis in b) is (0.47 ± 0.01) μm/pixel.

The trap size from this calibration is (6.72 ± 0.09) μm which can be compared to the value of (6.57 ± 0.02) μm as obtained by the razor blade method (see section 4.3.2 for details). We attribute the small discrepancy to the fact that the imaging plane on the CCD may not be perfectly in the range of focus which is given by the Rayleigh range (around 160 μm).

5.4 Characterisation

The sequence used to characterise the dipole trap in the new system is shown in figure 5.12. The science MOT is loaded from the LVIS for 2 s. After that the atomic beam from LVIS is shut to keep the background gas in the science chamber very low. The MOT is then compressed for 10 ms by ramping up the magnetic field gradient and red-shifting the MOT laser frequency (see details in section 5.2.1). The dipole trap beam is then switched on. The overlapping time with the MOT can be varied to maximise the number of trapped atoms. Next, the optical molasses are applied for 5 ms by switching off the magnetic field and decreasing the intensity of the MOT light. The atoms are then held in the dipole trap for a variable time to measure the trap lifetime (see details in section 5.2.2). Finally, the fluorescence imaging of atoms are detected by the ICCD unit for 5 ms when atoms are still held in the trap.

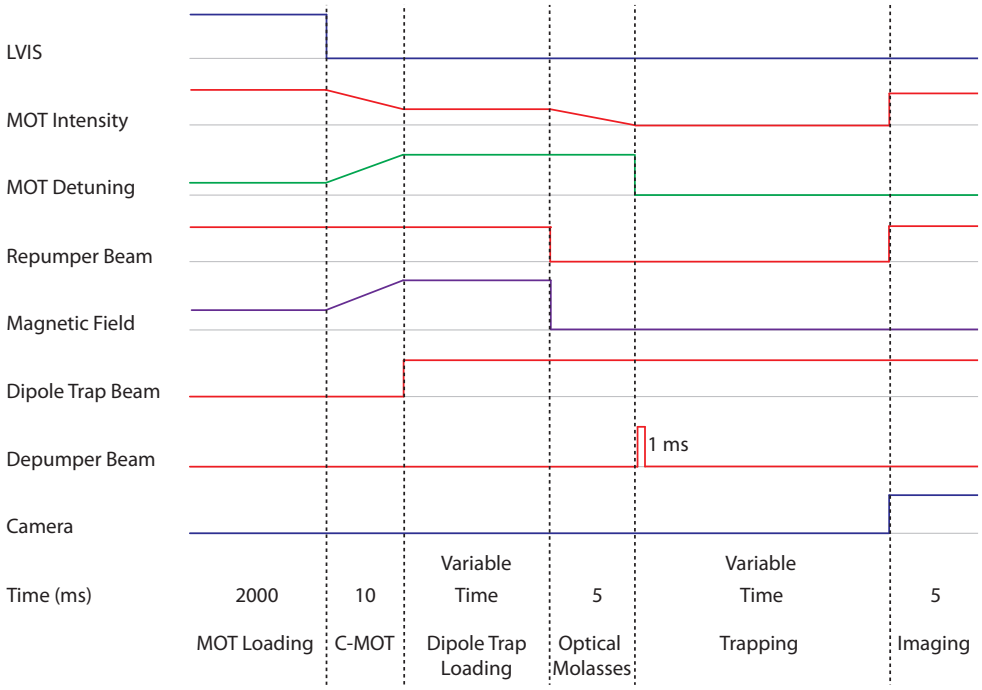

Figure 5.12: The experimental sequence used to determine the loading parameter and the lifetime of the dipole trap.

5.4.1 Dipole trap loading

The transfer of atoms from the MOT to the dipole trap follows the loading curve which is given by [77, 87]

$$\frac{dN}{dt} = Re^{-\gamma t} - \Gamma_L N - \beta_L N(N-1), \tag{5.5}$$

where R is the loading rate from the compressed MOT which has a lifetime of $1/\gamma$. Γ_L and β_L are the loss coefficients due to collisions with the background gas and two-body collisions respectively during the loading process. The subscript L is to indicate the loss coefficient during the loading process when the trapped atoms experience the MOT light.

Following equation (5.5), the number of atoms in the trap linearly increases at the beginning of the loading process. The loading rate (R) can be maximised by increasing the density of atoms (Compressed-MOT) [88]. However, the compression tends to heat the atoms causing losses. When the number of atoms in the dipole trap is increased, the collisions with the background gas and other trapped atoms start to play a role, as can be seen from the decrease in the tail of the loading curve.

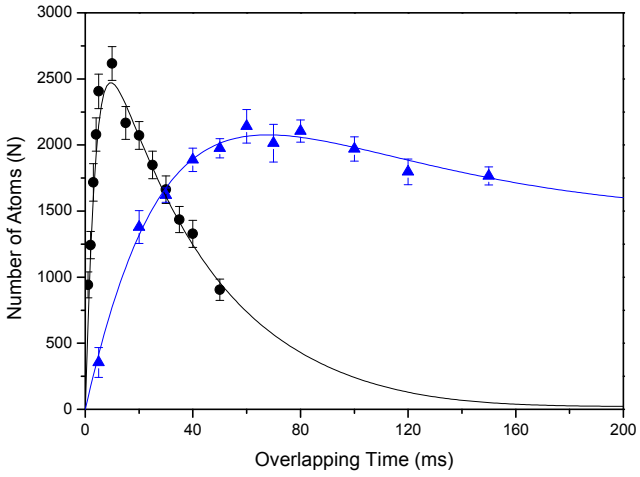

Figure 5.13: Loading curve of the dipole trap. The number of atoms vs loading time is reported together with the best fit with equation (5.5). The loading from the compressed MOT with a magnetic field gradient of 30 G/cm and a detuning of -10Γ is illustrated in black. The loading without compressing the MOT is shown in blue. The trap depth is 0.9 mK and the trap waist is 6.72 μm.

To study the loading process, the number of trapped atoms N is studied as a function of the overlapping time with results as in figure 5.13. The data is then fitted with equation (5.5) to determine the loading parameters.

The most important parameter is the loading rate which can be easily optimised by controlling the density of the MOT via the compression phase. The loading rate without the C-MOT (blue line) is around 1.1×10^5 atoms/s which can fill up the dipole trap within ∼50 ms. The C-MOT with a magnetic field gradient of 30 G/cm and a detuning of -10Γ (black line) can increase the loading rate to around 5.8×10^5 atoms/s and also reduce the loading time to ∼10 ms. The C-MOT can thus improve the loading efficiency. However, it also increases two body inelastic collisions (β_L) which are a significant source of losses in the loading process.

5.4.2 Lifetime

After the loading stage, the atoms are held for a variable time to study the dynamics of the atoms in the dipole trap. The loss mechanisms, namely collisions with the background gas and two-body collisions, are studied via lifetime measurements. The loss rate equation is written as [77]

$$\frac{dN}{dt} = -\Gamma_T N - \beta_T N(N-1), \tag{5.6}$$

where the parameter Γ_T and β_T are the loss coefficient in the absence of the MOT light. By solving equation (5.6), we obtain

$$N(t) = \frac{\Omega N_0}{\Omega e^{\Omega t} + \beta_T N_0 (e^{\Omega t} - 1)}, \tag{5.7}$$

where N_0 is the initial number of trapped atoms and $\Omega = \Gamma_T - \beta_T$. This equation is then used to fit the data to determine both loss coefficients.

The first parameter is the loss coefficient due to the background gas collisions. The lifetime for the different trap condition has been investigated as a function of the trap depth as illustrated in figure 5.14. We found that the lifetime for the new apparatus is clearly larger than in the previous one. Owing to the separation of the atomic source from the science chamber, the background gas collisions can be significantly

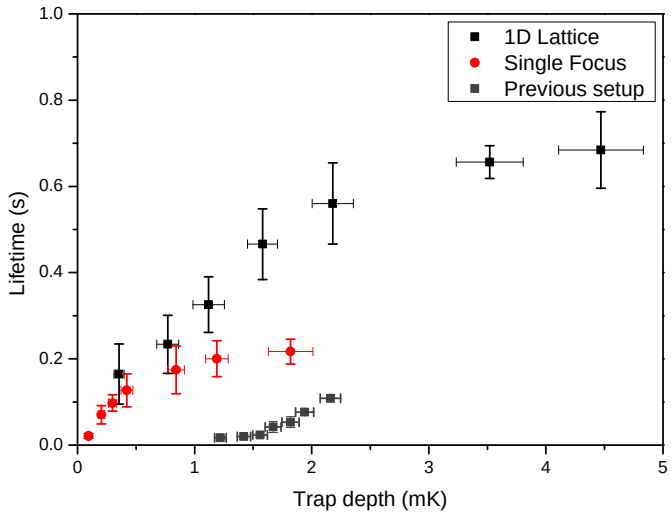

Figure 5.14: The comparison of lifetime measurement as a function of the trap depth for the single focussed beam dipole trap (black), the 1D lattice dipole trap (red) and the dipole trap from the previous apparatus (grey).

reduced, and thus the lifetime increases.

In a 1D optical lattice (1D lattice), atoms experience a strong confinement in the axial direction while the single focussed beam (SF trap) has far less dipole force along that axis. Moreover, the vibrational frequency of the 1D lattice is in the scale of a few hundred kHz while the SF trap has a trap frequency of a few hundred Hz[18]. The lifetime of the SF trap is then affected by the parametric heating since the noise level in the system tends to be very large at low frequency. As a result, the lifetime in the 1D lattice is larger than the SF trap especially for a deeper trap. However, the lifetime of both traps tends to be limited to around 700 ms for the 1D trap and 250 ms for the SF trap. The limitation may be caused by two-body collisions, as investigated next.

Another parameter in equation (5.6) is the two-body collisional coefficient (β_T). This parameter relates to the collisions of a trapped atom with other trapped atoms.

Figure 5.15 shows the two-body collisional coefficient as a function of the trap depth for the 1D lattice and the SF trap. The graph shows that the effect of two-body collisions is significantly reduced in the 1D lattice

[18]For example, a trap depth of 1.2 mK has an axial vibrational frequency of around 500 Hz and 510 kHz for the SF trap and the 1D lattice respectively

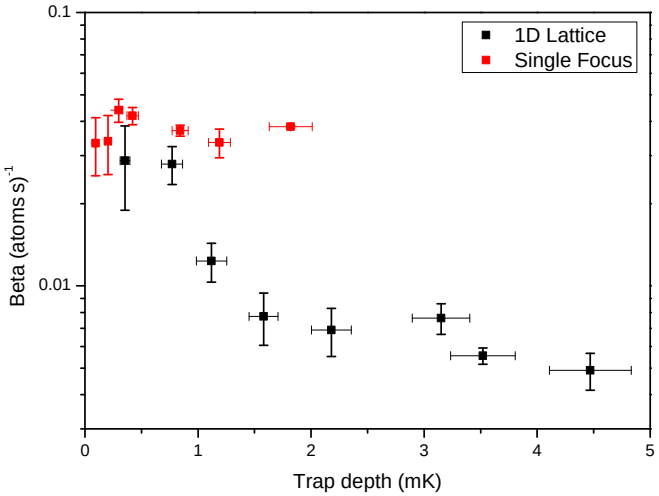

Figure 5.15: Comparison of two-body collision coefficients for the single focussed beam dipole trap and the 1D lattice dipole trap.

since the atoms in different wells do not collide. However, the collisions between atoms of different lattice sites increases at small trap depths as the atoms can jump over the lattice potential.

5.4.3 Collisions in dipole trap

In the dipole trap in the absence of the MOT light, atoms are in the ground state. The collisions taking place in the trap can be either elastic or inelastic [89]. When both atoms are in the lower energy level of the hyperfine ground state, an elastic collision is the only possible process. On the other hand, hyperfine changing collisions can lead to an exoergic process because the internal atomic energy can be transformed into kinetic energy [90]. In the case of Cs, the hyperfine splitting of 9.2 GHz corresponds to a transfer of energy of 0.15 K. This process then becomes a source of heating in the dipole trap.

In order to avoid the inelastic collisions, the trapped atoms can be prepared in the lower hyperfine ground state by applying a depumper laser. The depumper is tuned to the $F_g = 4 \rightarrow F_e = 3$ D_2 line transition by an AOM. The appropriate depumper intensity is then determined by applying the depumper light for the first 1 ms of the trapping time and detecting the number of trapped atoms after 50 ms as a function of the depumper intensity.

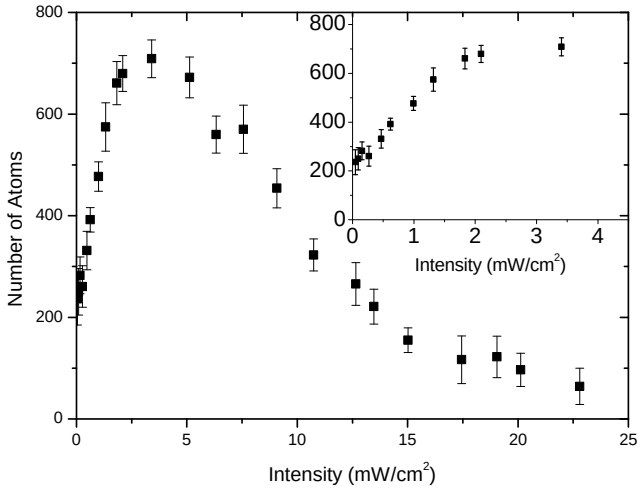

Figure 5.16: The number of atoms left in the single focussed beam dipole trap after 50 ms holding time is plotted as a function of the depumper intensity. The inset magnifies the intensity range up to 4 mW/cm^2 and illustrates the saturation effect around 2 mW/cm^2. The data was taken with a trap depth of U_0/k_B = -0.74 mK.

According to our results shown in figures 4.10 and 5.16, the intensity at which the effect of the depumper saturates is around 2 mW/cm^2. Figure 5.16 also shows that a depumper intensity above 5 mW/cm^2 can lead to the loss of trapped atoms due to recoil heating. Hence, the depumper intensity of (3.2±0.5) mW/cm^2 is the optimal intensity to suppress the hyperfine changing collisions.

The hyperfine changing collisions can be investigated by measuring the lifetime and the two-body collision coefficient with and without the application of the depumper light. The graph of both parameters illustrated in figure 5.17 and 5.18 clearly shows that the preparation of the atoms in the lower hyperfine ground state suppresses the exoergic inelastic collisions. The two-body collisional coefficient is reduced by about one order of magnitude, as shown in figure 5.17. A longer lifetime of the atoms prepared in the $F_g = 3$ ground state is also obtained as shown in figure 5.18. However, the lifetime of the 1D lattice and the SF trap are expected to be longer since the background pressure has been improved. Thus other loss mechanisms must play an important role.

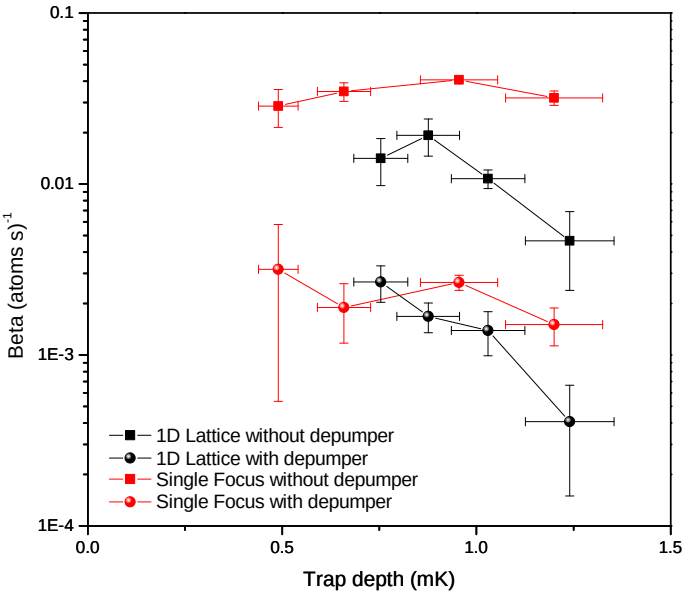

Figure 5.17: Two-body collisional coefficient (β_T) with and without the application of the depumper laser as a function of the trap depth.

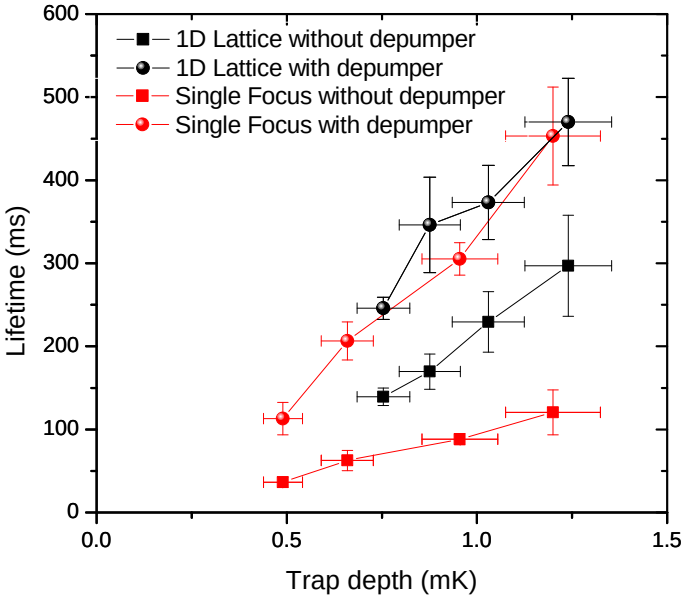

Figure 5.18: Lifetime with and without the application of the depumper laser as a function of the trap depth.

5.4.4 Other loss mechanisms

The new apparatus significantly reduces the background gas in the science chamber. The pressure measured from the ion pump is below 2.5×10^{-10} mbar and the pressure from the MOT lifetime measurement is around $(2.6 \pm 0.1) \times 10^{-10}$ mbar. Both pressures correspond to a maximum lifetime of around 40 s for a trap depth of 1.2 mK[19]. Our data in figure 5.18 shows a maximum lifetime of around 470 ms for the same trap depth. Hence, the collisions with the background gas is not the limiting factor in our experiment.

As discussed in the previous chapter, the heating due to the intensity fluctuations and the pointing instability can be an important heating source in the system. For the new dipole trap laser, this technical noise should be investigated to determine the loss mechanisms. The intensity fluctuations of the MOPA laser system is measured after the beam passes through a pinhole as it is illustrated in figure 5.19.

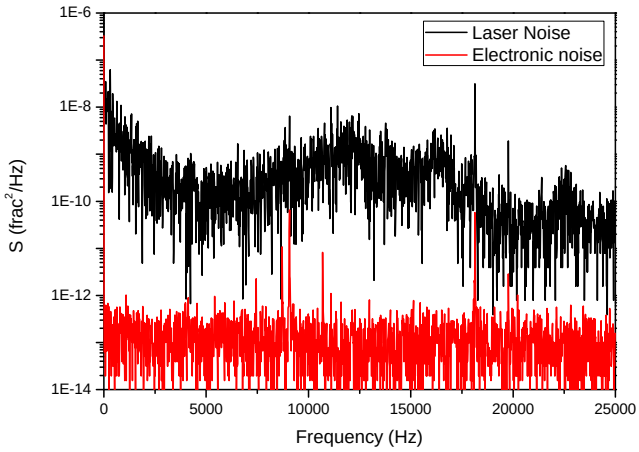

Figure 5.19: One-sided power spectrum of fractional fluctuations in the beam intensity of the MOPA laser is illustrated in black and the electronic noise is shown in red.

The same method as in section 4.3.6 is used to determine the limitation on the lifetime produced by these heating sources. The lifetime for a trap depth of 1.2 mK is limited to around 540 ms for the radial axis and around 34 s for the axial axis. Therefore, the lifetime of the new apparatus is limited by the intensity fluctuation caused by a major heating mechanism.

[19]This lifetime is calculated by using equation (4.34)

The pointing instability is also suspected to be another source of heating owing to the different optical tables of the dipole trap laser and the science cell. It can lead to different vibrational frequencies of the two optical tables. This can change the beam displacement on the objective which can shake the centre of the trap. However, the measurement of the pointing instability indicates that the lifetime is limited to around 2.8 s for a trap depth of 1.2 mK. Therefore, while the beam pointing instability is not a limiting factor for our current measurements, it will need to be addressed to obtain long lifetimes (more than 3 s).

5.5 Conclusions

In this chapter, I described the upgrade and the characterisation of the new apparatus. The vacuum system, the dipole trap laser and the imaging system have been upgraded. In order to reduce the collisions with the background gas, the atomic source is located in a different chamber and delivered through a small aperture, so as to maintain the lower pressure in the science chamber. This can increase the lifetime of the dipole trap to around 40 s. The unstable Ti-sapphire laser was replaced by a MOPA system which can provide a trap depth of 1.85 mK for the single focussed dipole trap and 4.5 mK for the 1D lattice. The imaging system was improved by covering the imaging beam path with a black tube and by blocking out-of-focus light with a series of iris. This can increase the signal-to-noise ratio, allowing us to detect a small number of atoms.

I also characterised the state-insensitive trap in the new system. The number of atoms loaded into the dipole trap can be increased by compressing the MOT during the loading process. The single focussed beam dipole trap and the 1D lattice were compared to study the lifetime and two-body collisions. I obtained a maximum lifetime of 700 ms at a trap depth of 4.5 mK for the lattice trap. I studied the hyperfine changing collisions which can limit our trap lifetime. The reduction of the two-body collisions can increase the lifetime to 440 ms for the SF trap and 470 ms for the 1D lattice with a trap depth of around 1.2 mK. Finally, I analysed the loss mechanisms by following the method outlined in the previous chapter, and concluded that our trap lifetime is limited by the intensity fluctuations of the dipole trap beam.

Chapter 6

Conclusions and outlook

6.1 Summary

The experimental work described in this thesis consisted of developing a state-insensitive trap for caesium atoms for possible future applications namely quantum control and high sensitive magnetometry. The state-insensitive trap for the D_2 line transition of caesium is known to be around 935 nm, the so-called magic wavelength. An experimental apparatus was set up. The cancellation of the differential AC Stark shift has been verified and the system was characterised.

The characterisation of the first experiment mainly considered the trap lifetime and the loss mechanisms at the magic wavelength provided by a Ti-sapphire laser. I found that the trap lifetime strongly depends on the trap depth and the different hyperfine ground states of the trapped atom. By introducing a depumper to prepare atoms in the $F_g = 3$ ground state, the trap yields a significantly longer lifetime than in the case of atoms occupying the $F_g = 4$ state. As a result of the application of the depumper, the system achieved the maximum lifetime of 3.6 s with a trap depth of 2.4 mK. The collisions with the background gas and the pointing instability of the trap beam were found to be the limiting factors for the lifetime.

In the second experiment, I upgraded the vacuum system to reduce the collisions with the background gas. The Ti-sapphire laser system has also been replaced with a MOPA system to solve the problem of long term power instability and to reduce the difficulty of maintenance.

In order to detect a small number of atoms, the imaging system was improved by enclosing the beam path with a black plastic tube and by blocking the out-of-focus light with a series of adjustable irises. This experiment compared the single focussed beam dipole trap with the 1D optical lattice trap. The characterisation of the new system included the study of the loading mechanism, the lifetime and the loss mechanisms. Following the improvement of the vacuum system, I expected a lifetime of around 40 s for a trap depth of 1.2 mK. However, the measurement showed that the 1D lattice trap has a maximum lifetime of 470 ms with a trap depth of 1.2 mK. The intensity fluctuation of the MOPA system and the pointing instability were found to be the major loss mechanisms of the new trap.

6.2 Improvements to the experiment

The 1D lattice experiment is still at an early phase so several improvements and optimisations are needed to yield a longer lifetime. The experiment in chapter 5 shows that the intensity fluctuation and the pointing instability of the dipole trap beam are a significant source of heating and therefore the major loss mechanisms. The simplest way to stabilise the intensity is by using a feedback circuit to control the output power via an AOM. The frequency response of the feedback circuit has to cover a frequency up to a few hundred kHz due to the axial vibrational frequency of the 1D lattice. Furthermore, the pointing instability can be improved by coupling the dipole trap beam into a fiber and mounting it on a more stable XYZ translation stage. These improvements will increase the lifetime up to 40 s, which is the limitation by the background gas collisions. Finally, another MOPA system will provide more optical power to create a 2D optical lattice trap which will be suitable to have a single atom occupation per site.

6.3 EIT in the state-insensitive trap

Much effort was put into the experimental setup and the characterisation in order to optimise and improve the system. The future research will

focus on the study of electromagnetically induced transparency (EIT) in the state-insensitive trap. EIT is a destructive quantum interference in a three-level system when two ground states are coupled to the same excited state [29]. This phenomenon can also be considered as the coherent population trapping (CPT) when atoms are cycled into the non-coupling state (Dark state) [56]. The narrow linewidth of the EIT and CPT feature is very useful in metrology applications, namely high sensitive magnetometry [91–93] and frequency standards [56, 94].

The EIT and CPT are mostly studied in a gas cell or a buffer-gas cell [29, 56]. The investigation showed that the collisional broadening [56, 95], the stray magnetic field [56] and the lack of interrogation time [56, 96] affect the linewidth of the EIT and CPT feature. Recently, EIT experiments have started to use cold atoms in order to narrow the linewidth extremely [31, 97, 98]. However, the magnetic field gradient of the MOT can broaden the linewidth of the EIT feature due to the Zeeman effect and the dipole trap can introduce an AC Stark effect which can also increase the linewidth of the EIT feature [81]. EIT experiments in a state-insensitive trap will overcome these broadenings. First of all, the atom-laser interrogation time will significantly increase since our experiment gains the long lifetime of the dipole trap [31]. Moreover, the state-insensitive trap will reduce the broadening due to the light shift [81]. Finally, the collisional broadening will be drastically reduced when each lattice has a single atom occupancy.

Appendix A

Locking system

A.1 PID controller

A Proportional-Integral-Derivative Controller (PID-Controller)[62, 99, 100] is a general control loop feedback widely used in control systems. A PID Controller processes the error between a measuring point and a setting point. The PID output is fed back to the system to change the process accordingly.

The PID controller consists of three parts: the Proportional, the Integral and the Derivative part. The Proportional part directly reacts to the current error, the Integral part reacts proportionally to the sum of errors in a given period of time and the Derivative part reacts proportionally to the rate at which the error is changing. By tuning these three parts, the stabilisation of the system to the set point can be optimised.

The output of the PID controller is given by:

$$Output(t) = K_p e(t) + K_i \int_t^0 e(t)dt + K_d \frac{de}{dt}, \tag{A.1}$$

where

e is the error signal which is the difference between the output and the setpoint.

K_p is the Proportional gain: a larger value will increase the settling speed but the system will become unstable and starts to oscillate.

K_i is the Integral gain: a larger value will accelerate the settling speed but it causes a larger overshoot.

K_d is the Derivative gain: a larger value will decrease the overshooting amplitude but high frequency noise gets amplified.

Ideally, the PID output will change the system until the measuring point has the same value as the setpoint. Our system used to lock the laser frequency requires only the proportional and integral parts.

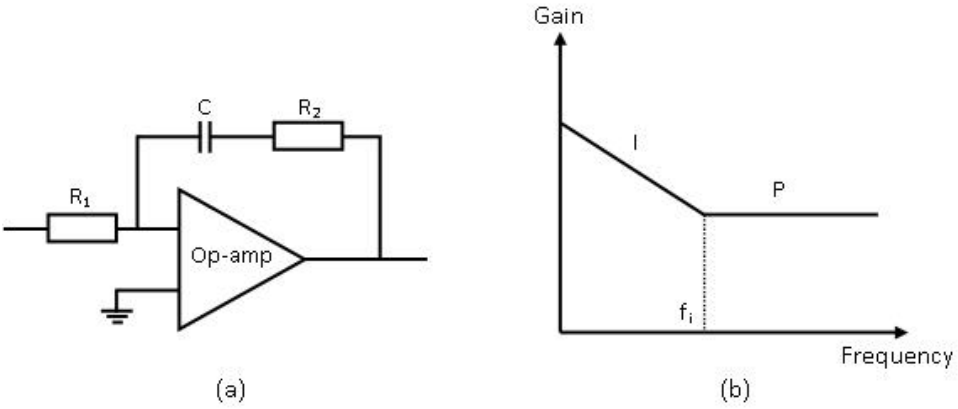

Figure A.1: (a) The PI circuit, (b) The Bode plot of the PI controller

To design the PI controller, the frequency response for the P and I part has to be calculated [100]. It can be seen from the Bode plot in figure A.1(b) that for low frequency, the PI controller acts as an integrator and for high frequency as a proportional amplifier. The connection between the two regions, called PI-corner, is characterised by the cut-off frequency f_i of the PI controller. A PI controller can be made using only one op-amp, the circuit is shown in figureA.1(a). The gain is given by:

$$K = K_p + K_i = \frac{R_2}{R_1}\left(1 + \frac{1}{i\omega R_2 C}\right), \tag{A.2}$$

where the overall gain is $\frac{R_2}{R_1}$ and the feedback factor of the integral part is given by:

$$k = \frac{i\omega R_2 C}{1 + i\omega R_2 C}. \tag{A.3}$$

The gain and the phase shift of the frequency response are given by:

$$\begin{aligned} |A| &= \frac{1}{\sqrt{1+(\omega R_2 C)^2}} \\ \varphi &= -\arctan(\omega R_2 C). \end{aligned} \tag{A.4}$$

The cut off frequency is defined by the -3dB gain or the phase shift of -45°[100] so the cut off frequency or the PI corner can be calculated from equation (A.4). The PI corner is given by:

$$f_i = \frac{1}{2\pi R_2 C}. \tag{A.5}$$

A.2 Electronic design

A.2.1 Photodiode box

The photodiode unit is used to produce the error signal by subtracting the signals from the two photodiodes. The unit consists of two photodiodes[1], two photodiode amplifiers and another op-amp circuit to subtract the two signals. The changing light intensity changes the current which results in a voltage drop over a resistor. Then, this voltage will be inversed and amplified by an IC OP27 circuit which has a variable resistor to adjust its gain. After that, the signals from the two photodiode amplifiers are subtracted by another amplifier circuit (IC AD624). The sign of the resulting signal can be changed with a switch and its amplitude can be changed with a variable resistor.

A.2.2 PI-lock box

To stabilise the laser to the wanted transition, a lock box is needed which can be divided into two parts: the PI-control and the piezo driver.

The PI-control is the important part of the lock box because this part is used to generate the stabilisation signal. The proportional part is used to adjust the settling speed. If it is too high, the signal will oscillate, if it is too low, the signal will easily go out of lock. The integral part which is adjustable via the PI-corner frequency switch is used to compensate slow

[1]VISHAY BPW34 Photodiode

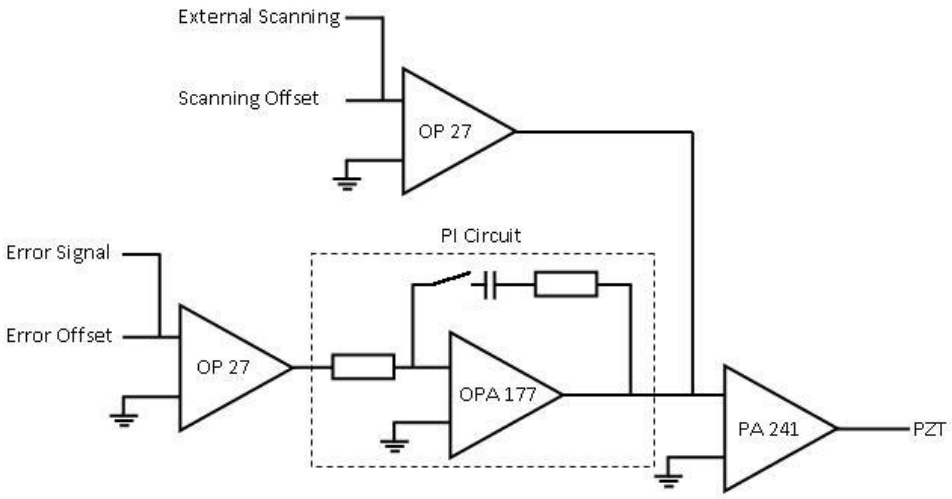

Figure A.2: Circuit diagram of PI-lock box

drifting or constant errors. If this part is too small, the settling time is increased. If it is too big, it causes the overshooting in the system. In the first part of the circuit, an offset is added to the error signal to move the locking point or to compensate for electronic offsets. This signal is then processed by the PI-circuit.

The piezo driver uses a high voltage amplifier (IC PA241) which can operate over a range of 300 volts to drive the piezo. It can be switched between an external ramp signal and the locking signal. Before the high voltage amplifier, the error signal and the scanning signal are combined. When the switch is on the unlock position the PI-control is bypassed so the error signal has no effect on the piezo but the scanning signal can still go through the piezo. After the scanning amplitude is reduced and we switch to the lock position, the error signal part will start to drive the piezo to stabilise the laser.

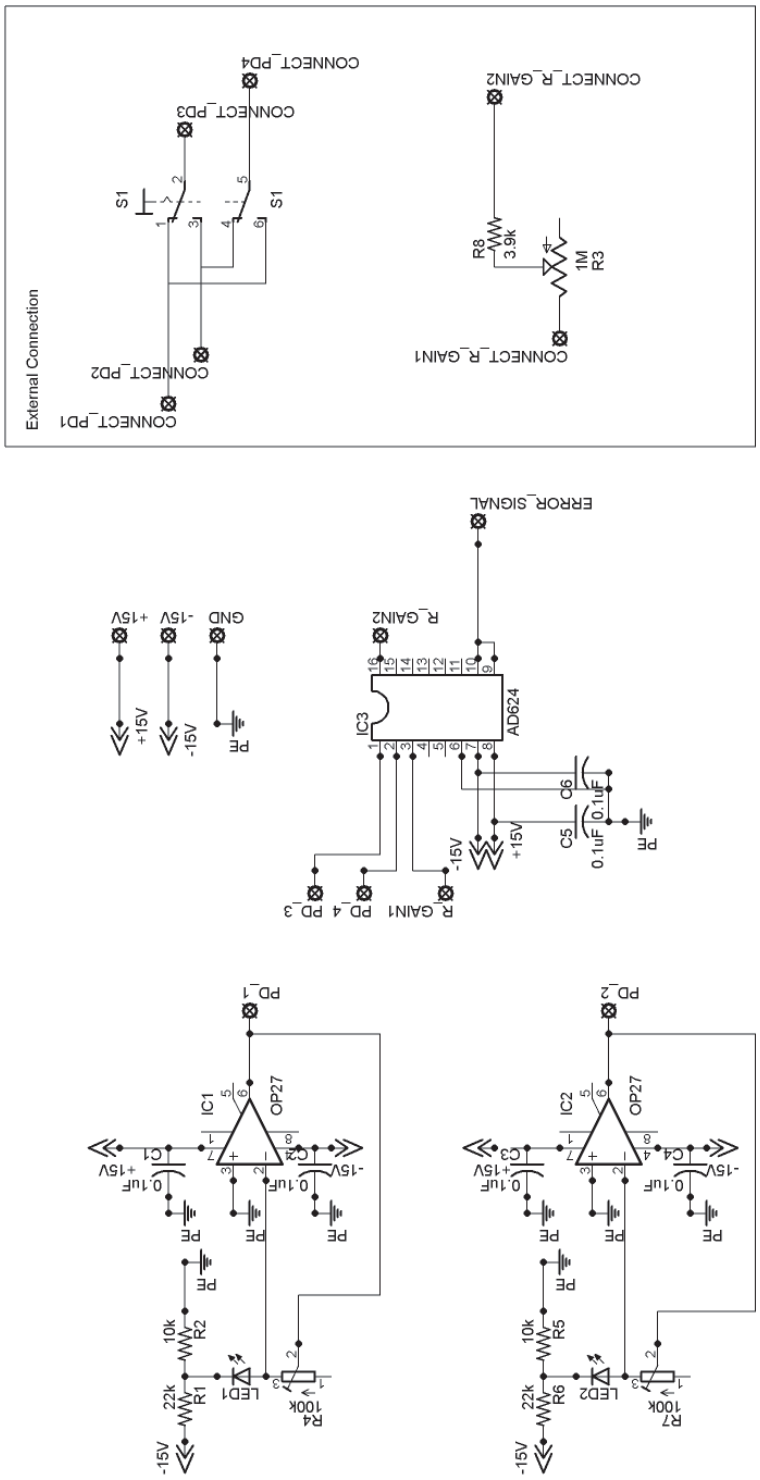

Figure A.3: Schematic for the photodiode with the differential amplifier

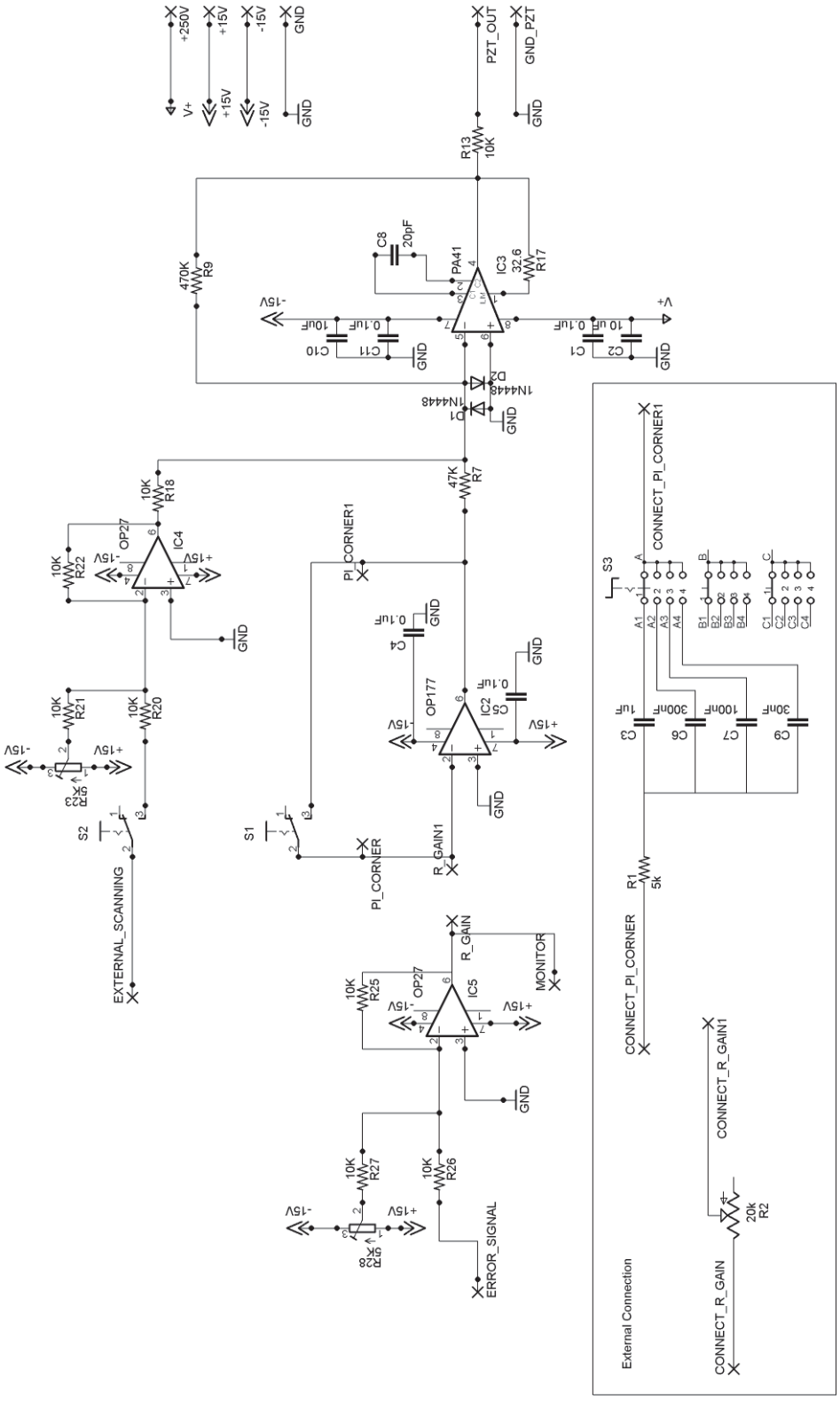

Figure A.4: Schematic for the proportional and integral locking circuit

Appendix B

Phase-locked loop circuit

The electronics for the PLL system is illustrated in figure B.1. The ultrafast photodiode is used to detect the 9.192631770 GHz beat signal between the two lasers to be locked as the local oscillator. The function generator produces the 9.232631770 GHz as the reference frequency. It also provides the 10 MHz reference for another function generator and the spectrum analyser. The signal from the local oscillator and the reference frequency are then mixed down to 40 MHz because the digital phase detector can operate up to the frequency of 200 MHz. Another function generator provides the reference frequency at 40 MHz for the phase detector.

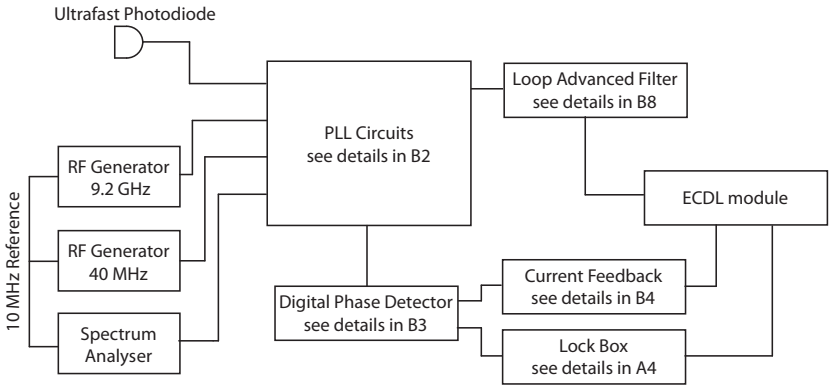

Figure B.1: The connection diagram for the PLL system.

The PLL circuit is shown in figure B.2. This circuit prepares the signal for the digital phase detector shown in figure B.3. The mixed-down frequency from the PLL circuits passes through the loop filter shown in figure B.8 to obtain the fast feedback.

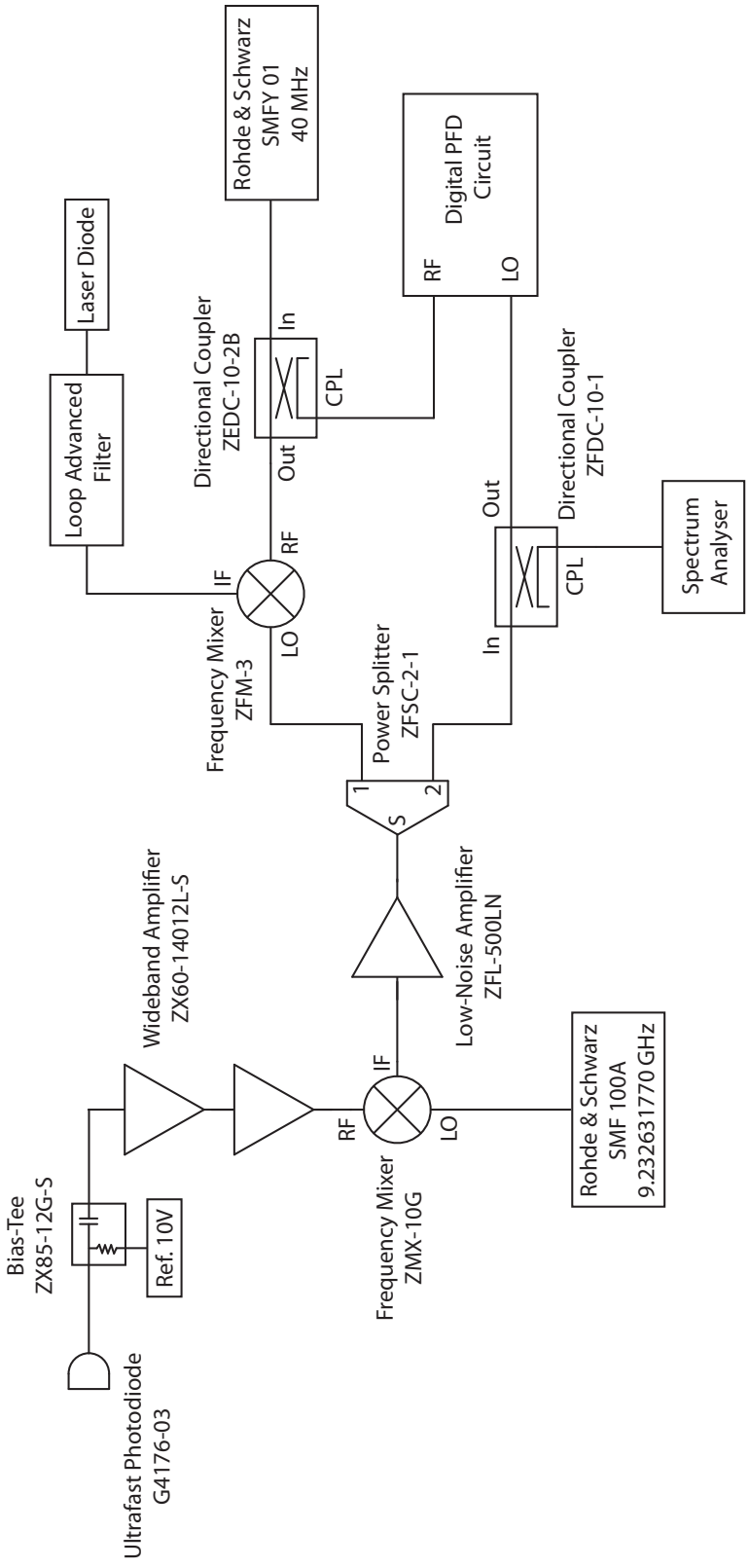

Figure B.2: The RF components for PLL.

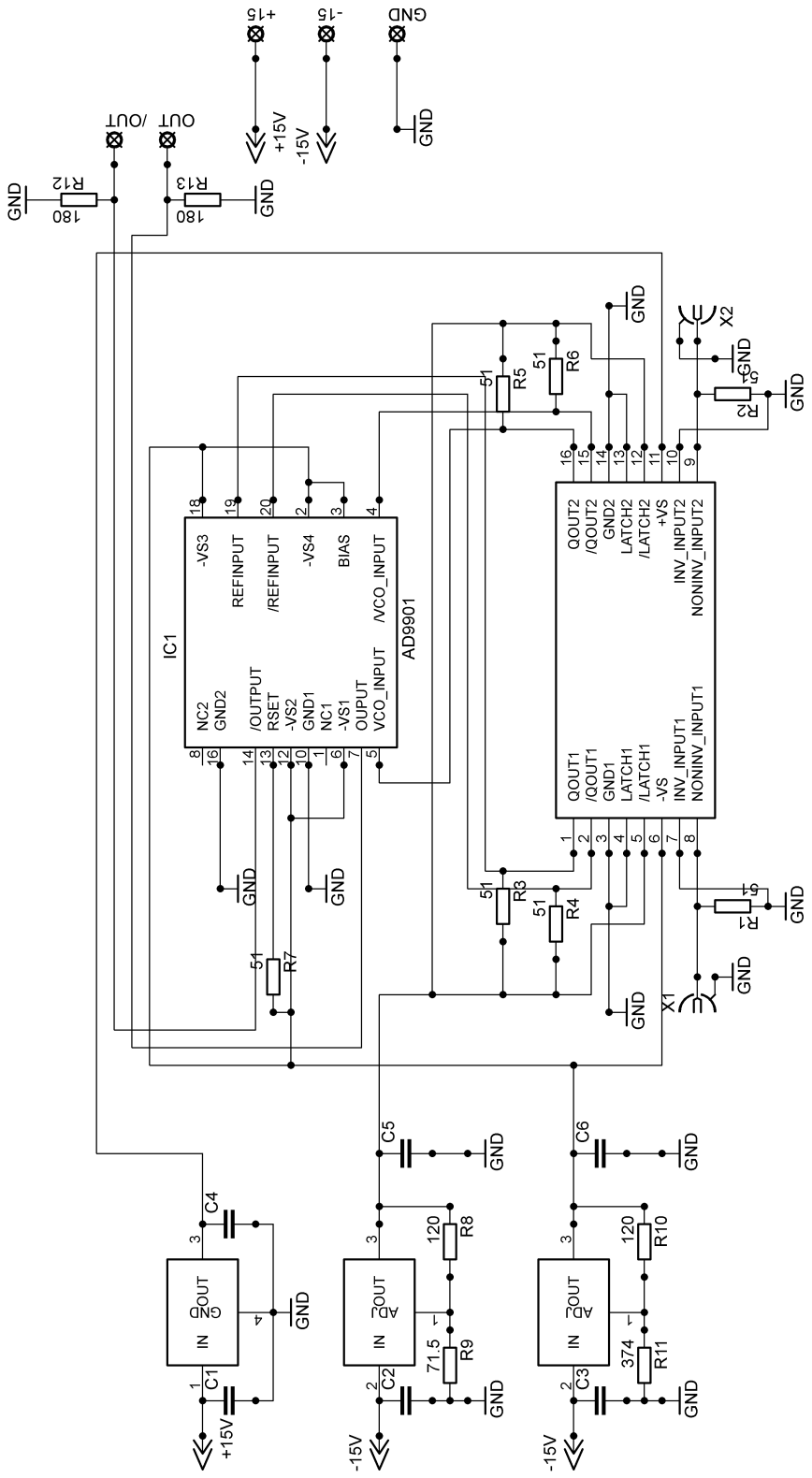

Figure B.3: The digital phase detector circuit.

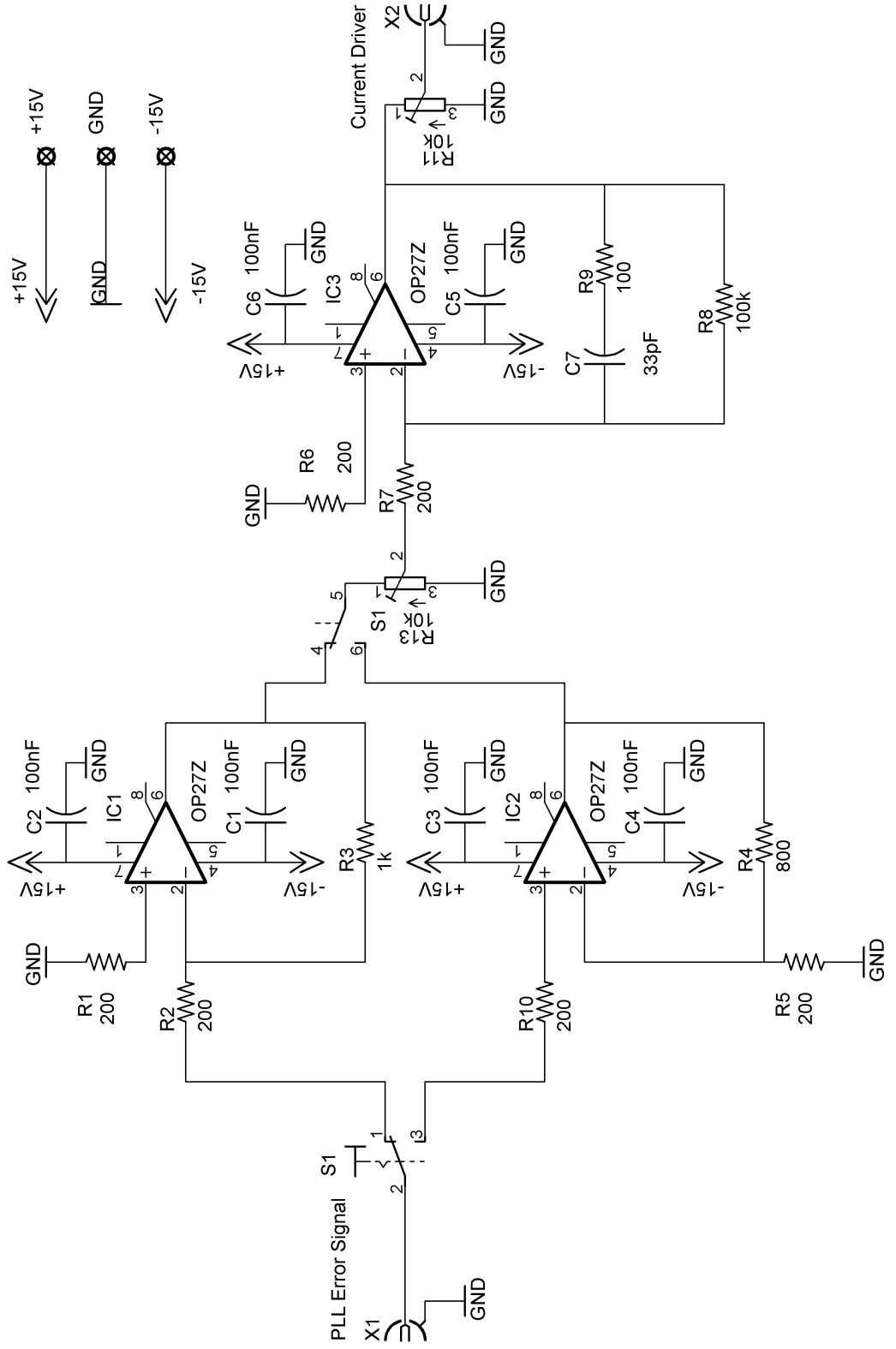

Figure B.4: The PLL feedback circuit.

In order to stabilise the phase of the laser with respect to a reference laser, some feedback loops are required. We use three feedback for the laser: the PZT feedback, the current feedback and the fast current feedback (see figure B.1). The PZT and current feedback are provided by the positive and negative error signal from the digital phase detector circuit.

The negative error signal is fed to the lock box which has the proportional and integral control circuit. This can provide the slow feedback in a range below 100 Hz to the PZT. By maximising the gain for the lockbox, the PZT starts to oscillate at the maximum frequency of the feedback circuit. We obtain the maximum PZT bandwidth around 74 Hz as shown in the red arrow of figure B.5.

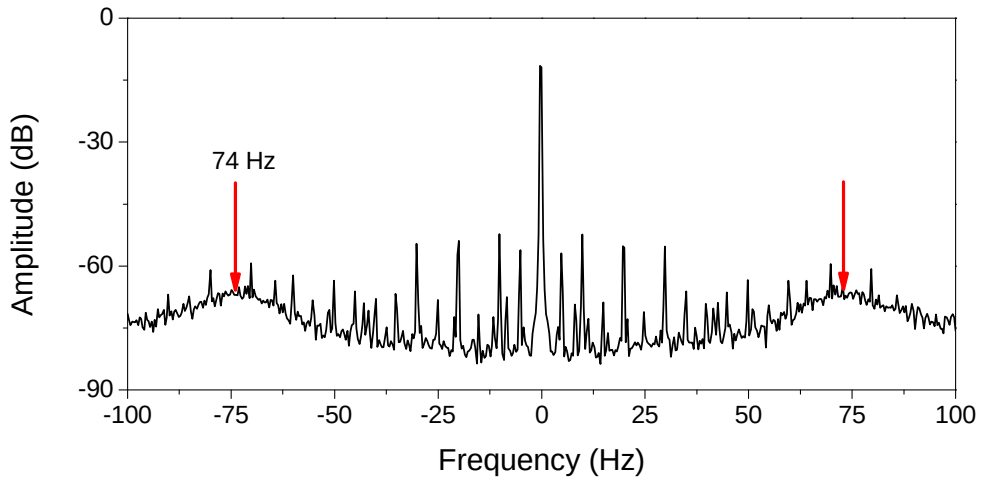

Figure B.5: Spectrum of the optical phase-locked loops indicates the PZT bandwidth pointed by the red arrow. The PZT bandwidth is maximised around 74 Hz.

On the other hand, the positive error signal is used for the current feedback. The current feedback circuit designed in figure B.4 includes a sign selection section and the feedback circuit. The sign selection is made of an inverting and a non-inverting Op Amp with a gain of -5 and 5 respectively. The feedback circuit is the inverting integrator circuit which can be considered as a low-pass filter. The Bode plot of the current feedback circuit in figure B.4 is simulated by PSpice[1]. It shows the low-pass characteristic of the circuit with the cut-off frequency at 1.17 MHz.

[1]ORCAD PSpice Student Version Release 9.1

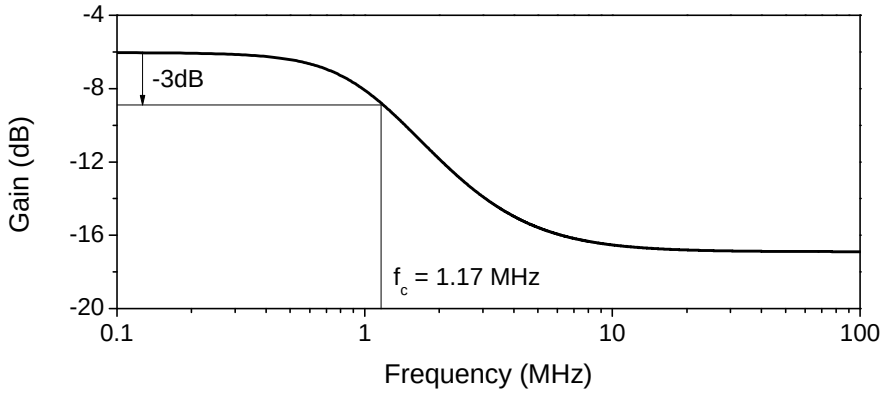

Figure B.6: The Bode plot of the current feedback points out the cut-off frequency at 1.17 MHz.

The current feedback bandwidth is determined in the same way as the PZT bandwidth. The current feedback has a maximum bandwidth of 1.4 MHz as shown in figure B.7.

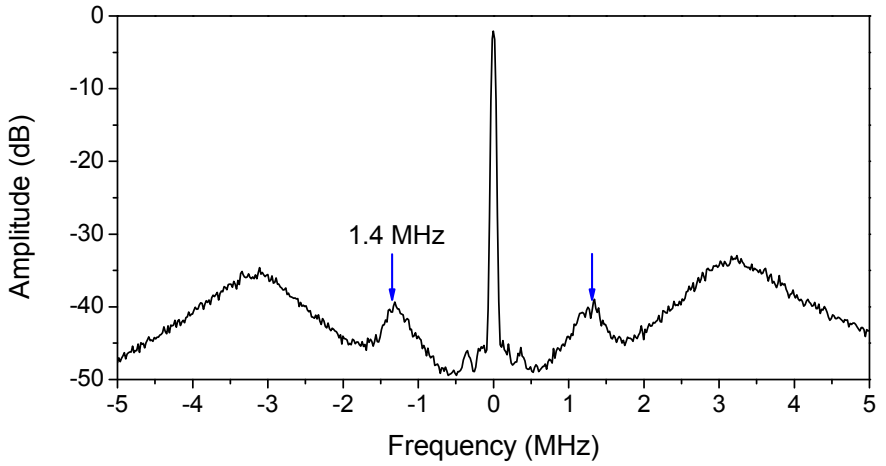

Figure B.7: The current feedback bandwidth of the PLL system.

Another crucial feedback loop is the fast feedback which is used to stabilise the phase difference of two lasers. The main circuit in this feedback loop is called the "$loop\ filter$" which acts as a bandpass filter. The schematic of the loop filter in figure B.8 is adapted from ref. [64].

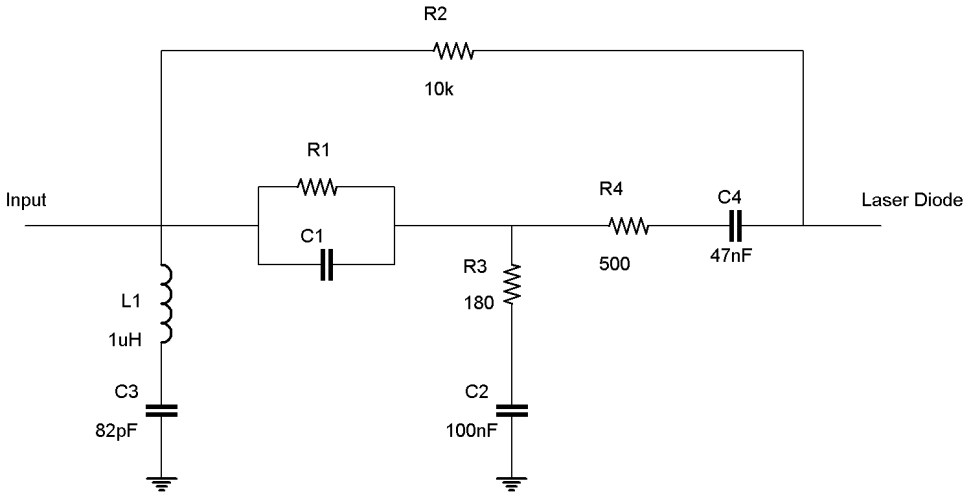

Figure B.8: The loop advanced filter circuit.

The loop advanced filter consists of two main parts: a notch filter and a highpass filter. The notch filter consists of the inductor $L1$ and the capacitor $C3$, and has a frequency block around 50 MHz. This is used to filter the modulation frequency. Next, the highpass filter is the important part of the loop filter which can change the loop bandwidth. By adjusting the value of the capacitor $C1$ and the resistor $R1$ in the schematic B.8, the cut-off frequency of the highpass filter can be changed. The cut-off frequency in table B.1 is simulated from the schematic of the loop filter by PSpice.

Figure	Loop bandwidth	Cut-off frequency	C1	R1
B.9 a)	5.9 MHz	6.9 MHz	1 nF	100 Ω
B.9 b)	5.7 MHz	6.4 MHz	1 nF	5.1k Ω
B.9 c)	4.1 MHz	5.1 MHz	2 nF	100 Ω
B.9 d)	3.4 MHz	4.6 MHz	2 nF	5.1k Ω
B.9 e)	2.2 MHz	3.7 MHz	3 nF	100 Ω

Table B.1: The calculation of the cut-off frequency for the highpass filter is compared to the loop bandwidth from the experiment. The value of the capacitor $C1$ and the resistor $R1$ relates to the schematic B.8.

In our PLL system, the loop bandwidth can be changed in the range of 1.1 to 5.9 MHz. The loop bandwidth is the maximum frequency at which the loop can follow the phase change. This is an indication of the stability of the PLL. We can consider the spectrum signal in figure

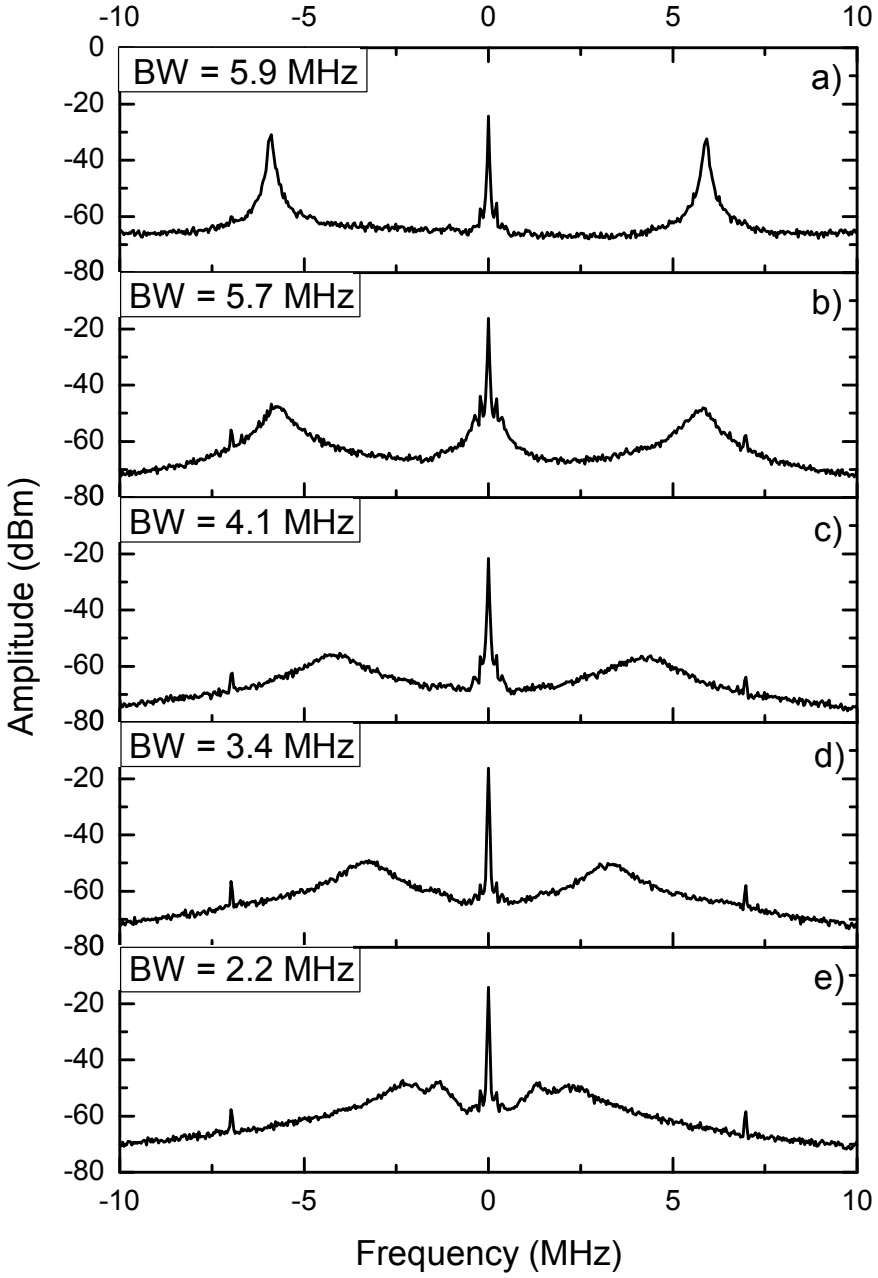

Figure B.9: The loop bandwidth of the PLL system for the different characteristics of the loop filter.

B.9. For a loop bandwidth larger than 4 MHz, the oscillation around the centre frequency becomes larger when the loop bandwidth is increased. As a result of the highpass filter, the small gain for the low frequency oscillation is not enough to stabilise the system. So the signal starts to oscillate as can be seen in figure B.9 b) and c). At the very large loop bandwidth, the PLL becomes very unstable due to the large oscillation at the loop bandwidth as shown in figure B.9 a).

On the other hand, a small loop bandwidth below 2 MHz can lead to an oscillation of the PLL as the loop cannot stabilise the high frequency phase fluctuations. It can be seen from figure B.9 e) that the amplitude of the centre frequency becomes smaller when the loop bandwidth is reduced.

The most stable loop bandwidth of our PLL is around 3.4 MHz in figure B.9 d). The signal-to-noise ratio for the centre frequency is more than 35 dB and the relative linewidth of our OPLL is around 2 Hz.

Bibliography

[1] T. Hänsch and A. Schawlow, Optics Communications **13**, 68 (1975).

[2] D. Wineland and H. Dehmelt, Am. Phys. Soc. **20**, 637 (1975).

[3] D. J. Wineland, R. E. Drullinger, and F. L. Walls, Phys. Rev. Lett. **40**, 1639 (1978).

[4] W. Neuhauser, M. Hohenstatt, P. Toschek, and H. Dehmelt, Phys. Rev. Lett. **41**, 233 (1978).

[5] S. Chu, L. Hollberg, J. E. Bjorkholm, A. Cable, and A. Ashkin, Phys. Rev. Lett. **55**, 48 (1985).

[6] E. Raab, M. Prentiss, A. Cable, S. Chu, and D. Pritchard, Physical Review Letters **59**, 2631 (1987).

[7] V. S. Letokov, *Laser Control of Atoms and Molecules* (Oxford University Press, 2007).

[8] C. J. Foot, *Atomic Physics* (Oxford University Press, 2005).

[9] S. Chu, J. E. Bjorkholm, A. Ashkin, and A. Cable, Physical Review Letters **57**, 314 (1986).

[10] J. D. Miller, R. A. Cline, and D. J. Heinzen, Phys. Rev. A **47**, R4567 (1993).

[11] M. D. Barrett, J. A. Sauer, and M. S. Chapman, Phys. Rev. Lett. **87**, 010404 (2001).

[12] G. K. Campbell, A. D. Ludlow, S. Blatt, J. W. Thomsen, M. J. Martin, M. de Miranda, T. Zelevinsky, M. M. Boyd, J. Ye, S. A. Diddams, et al., Metrologia **45**, 539 (2008).

[13] M. Takamoto, F. L. Hong, R. Higashi, and H. Katori, Nature **435**, 321 (2005).

[14] Z. Barber, Ph.D. thesis, University of Colorado (2007).

[15] G. Reymond, N. Schlosser, and P. Grangier, in *The Expanding Frontier of Atomic Physics*, edited by H. R. Sadeghpour, E. J. Heller, and D. E. Pritchard (2003), pp. 65–72.

[16] D. Schrader, S. Kuhr, W. Alt, M. Müller, V. Gomer, and D. Meschede, Applied Physics B: Lasers and Optics **73**, 819 (2001).

[17] I. Dotsenko, W. Alt, M. Khudaverdyan, S. Kuhr, D. Meschede, Y. Miroshnychenko, D. Schrader, and A. Rauschenbeutel, Phys. Rev. Lett. **95**, 033002 (2005).

[18] D. Frese, B. Ueberholz, S. Kuhr, W. Alt, D. Schrader, V. Gomer, and D. Meschede, Phys. Rev. Lett. **85**, 3777 (2000).

[19] H. Katori, T. Ido, and M. Kuwata-Gonokami, Journal of the Physical Society of Japan **68**, 2479 (1999).

[20] M. Takamoto and H. Katori, Phys. Rev. Lett. **91**, 223001 (2003).

[21] A. Brusch, R. Le Targat, X. Baillard, M. Fouché, and P. Lemonde, Phys. Rev. Lett. **96**, 103003 (2006).

[22] A. Derevianko and H. Katori, Rev. Mod. Phys. **83**, 331 (2011).

[23] Z. W. Barber, C. W. Hoyt, C. W. Oates, L. Hollberg, A. V. Taichenachev, and V. I. Yudin, Phys. Rev. Lett. **96**, 083002 (2006).

[24] L. Yi, S. Mejri, J. J. McFerran, Y. Le Coq, and S. Bize, Phys. Rev. Lett. **106**, 073005 (2011).

[25] R. Santra, K. V. Christ, and C. H. Greene, Phys. Rev. A **69**, 042510 (2004).

[26] N. Lundblad, M. Schlosser, and J. V. Porto, Phys. Rev. A **81**, 031611 (2010).

[27] F. L. Kien, V. I. Balykin, and K. Hakuta, Journal of the Physical Society of Japan **74**, 910 (2005).

[28] J. McKeever, J. R. Buck, A. D. Boozer, A. Kuzmich, H.-C. Nägerl, D. M. Stamper-Kurn, and H. J. Kimble, Phys. Rev. Lett. **90**, 133602 (2003).

[29] M. Fleischhauer, A. Imamoglu, and J. P. Marangos, Rev. Mod. Phys. **77**, 633 (2005).

[30] J. P. Marangos, J. Mod. Opt. **45**, 471 (1998).

[31] B. Kaltenhäuser, H. Kübler, A. Chromik, J. Stuhler, T. Pfau, and A. Imamoglu, Journal of Physics B: Atomic, Molecular and Optical Physics **40**, 1907 (2007).

[32] H. J. Metcalf and P. van der Straten, *Laser Cooling and Trapping* (Springer-Verlag, 1999).

[33] F. Dunning and R. Hulet, *Atomic, Molecular, and Optical Physics: Atoms and Molecules* (Academic Press, 1996).

[34] L. A. Orozco, AIP Conference Proceedings **464**, 67 (1999).

[35] D. A. Steck, *Cesium D Line Data* (2010), URL `http://steck.us/alkalidata`.

[36] D. Budker, D. F. Kimball, and D. P. Demille, *Atomic Physics: An Exploration through Problems and Solutions* (Oxford University Press, 2008).

[37] R. Grimm, M. Weidemüller, and Y. B. Ovchinnikov, Advances in Atomic, Molecular and Optical Physics **42**, 95 (2000).

[38] L. Curtis, *Atomic Structure and Lifetimes* (Cambridge University Press, 2003).

[39] D. Schrader, Ph.D. thesis, University Bonn (2004).

[40] D. J. Griffiths, *Introduction to Quantum Mechanics* (Prentice-Hall Inc., 1995).

[41] B. D. C. Cohen-Tannoudji and F. Laloë, *Quantum Mechanics* (Hermann and John Wiley & Sons. Inc., 2005).

[42] J. J. Sakurai, *Modern Quantum Mechanics* (Addison-Wesley Publishing Company, 1994), revised ed.

[43] M. Fabry and J. R. Cussenot, Can J. Phys **54**, 836 (1976).

[44] J. McKeever, Ph.D. thesis, California Institute of Technology (2004).

[45] P. W. Milonni and J. H. Eberly, *Lasers* (A Wiley-Interscience publication, 1988).

[46] P. Douglas, Ph.D. thesis, University College London (2009).

[47] C. E. Wieman and L. Hollberg, Rev. Sci. Instrum. **62**, 1 (1991).

[48] S. Chu, Rev. Mod. Phys. **70**, 685 (1998).

[49] C. Ye, *Tunable External Cavity Diode Lasers* (World Scientific Publishing Co. Pte. Ltd., 2004).

[50] L. Ricci, M. Weidemiiller, T. Esslinger, A. Hemmerich, C. Zimmermann, V. Vuletic, W. Kijnig, and T. W. Hänsch, Opt. Comm. **117**, 541 (1995).

[51] K. L. Corwin, Z. Lu, C. F. Hand, R. J. Epstein, and C. E. Wieman, Applied Optics **37**, 3295 (1998).

[52] M. Miyabe, M. Kato, M. Oba, I. Wakaida, K. Watanabe, and K. Wendt, Japanese Journal of Applied Physics **45**, 4120 (2006).

[53] *Operators Manual: Single frequency Ti:sapphire laser MBR-110*, Microlase Optical System (1993).

[54] *Service Manual: MBR-110*, Coherent (2002).

[55] L. Lu-Ming, T. Wen-Zhuo, H. Zhen-Yan, and G. Hong, Chinese Physics Letters **25**, 3253 (2008).

[56] R. Wynands and A. Nagel, Appl. Phys. B. **68**, 1 (1999).

[57] A. M. Marino and J. C. R. Stroud, Review of Scientific Instruments **79**, 013104 (pages 8) (2008).

[58] S. E. Park, T. Y. Kwon, and H. S. Lee, IEEE transaction on Instrumentation and Measurement **52**, 277 (2003).

[59] P. Bouyer, T. L. Gustavson, K. G. Haritos, and M. A. Kasevich, Opt. Lett. **21**, 1502 (1996).

[60] W. F. Egan, *Phase-Lock Basics* (A Wiley-Interscience, 1998).

[61] W. F. Egan, *Frequency Synthesis by Phase Lock* (A Wiley-Interscience, 1999).

[62] P. Horowitz and W. Hill, *The Art of Electronics* (Cambridge University Press, 1989).

[63] G. Reehal, Master's thesis, The Ohio State University (1998).

[64] M. Prevedelli, T. G. M. Freegarde, and T. W. Hänsch, Appl. Phys. B. **60**, S241 (1995).

[65] T. Y. Kwon, T. Kurosu, Y. Koga, S. ichi Ohshima, and T. Ikegami, Japanese Journal of Applied Physics **42**, L924 (2003).

[66] W. Alt, Optik **113**, 142 (2002).

[67] *Image Intensifier Unit C9016-2x Series Instruction Manual*, Hamamatsu Photonics (2005).

[68] *IEEE1394 Digital CCD Camera C4742-80-12AG Instruction Manual*, Hamamatsu Photonics (2004).

[69] V. Makarov, A. Anisimov, and S. Sauge, arXiv (2009), URL `http://arxiv.org/abs/0809.3408v2`.

[70] S. Cova, M. Ghioni, A. Lacaita, C. Samori, and F. Zappa, Appl. Opt. **35**, 1956 (1996).

[71] I. Rech, I. Labanca, M. Ghioni, and S. Cova, Review of Scientific Instruments **77**, 033104 (2006).

[72] P. Rosenbusch, S. Ghezali, V. A. Dzuba, V. V. Flambaum, K. Beloy, and A. Derevianko, Phys. Rev. A. **79**, 013404 (2009).

[73] S. Friebel, C. D'Andrea, J. Walz, M. Weitz, and T. W. Hänsch, Phys. Rev. A **57**, R20 (1998).

[74] J. Wu, R. Newell, M. Hausmann, D. J. Vieira, and X. Zhao, J. Appl. Phys. **100**, 054903 (2006).

[75] R. Jáuregui, Physical Review A **64**, 053408 (2001).

[76] S. Balik, A. L. Win, and M. D. Havey, Physical Review A **80**, 023404 (2009).

[77] K. L. Corwin, S. J. M. Kuppens, D. Cho, and C. E. Wieman, Phys. Rev. Lett. **83**, 1311 (1999).

[78] T. A. Savard, K. M. O'Hara, and J. E. Thomas, Phys. Rev. A. **56**, R1095 (1997).

[79] M. E. Gehm, K. M. O'Hara, T. A. Savard, and J. E. Thomas, Phys. Rev. A. **58**, 3914 (1998).

[80] H. C. W. Beijerinck, Phys. Rev. A. **61**, 033606 (2000).

[81] J. Dalibard and C. Cohen-Tannoudji, J. Opt. Soc. Am. B **2**, 1707 (1985).

[82] Y. B. Ovchinnikov, Optics Communications **249**, 473 (2005).

[83] Z. T. Lu, K. L. Corwin, M. J. Renn, M. H. Anderson, E. A. Cornell, and C. E. Wieman, Phys. Rev. Lett. **77**, 3331 (1996).

[84] J. Schoser, A. Batär, R. Löw, V. Schweikhard, A. Grabowski, Y. B. Ovchinnikov, and T. Pfau, Phys. Rev. A **66**, 023410 (2002).

[85] A. M. Steane, M. Chowdhury, and C. J. Foot, J. Opt. Soc. Am. B **9**, 2142 (1992).

[86] J. L. C. Yihan Xiong, Sytil Murphy and K. Repasky, Opt. Eng. **45**, 124205 (2006).

[87] N. Schlosser, G. Reymond, and P. Grangier, Phys. Rev. Lett. **89**, 023005 (2002).

[88] D. Sofikitis, G. Stern, L. Kime, E. Dimova, A. Fioretti, D. Comparat, and P. Pillet, Eur. Phys. J. D **61**, 437 (2011).

[89] J. Weiner, *Cold and Ultracold Collisions in Quantum Microscopic and Mesoscopic Systems* (Cambridge University Press, 2003).

[90] M. Mudrich, S. Kraft, J. Lange, A. Mosk, M. Weidemüller, and E. Tiesinga, Phys. Rev. A **70**, 062712 (2004).

[91] V. I. Yudin, A. V. Taichenachev, Y. O. Dudin, V. L. Velichansky, A. S. Zibrov, and S. A. Zibrov, Phys. Rev. A **82**, 033807 (2010).

[92] C. Andreeva, G. Bevilacqua, V. Biancalana, S. Cartaleva, Y. Dancheva, T. Karaulanov, C. Marinelli, E. Mariotti, and L. Moi, Applied Physics B Lasers and Optics **76**, 667 (2003).

[93] A. Nagel, L. Graf, A. Naumov, E. Mariotti, V. Biancalana, D. Meschede, and R. Wynands, EPL (Europhysics Letters) **44**, 31 (1998).

[94] S. Knappe, R. Wynands, J. Kitching, H. G. Robinson, and L. Hollberg, J. Opt. Soc. Am. B **18**, 1545 (2001).

[95] M. Erhard and H. Helm, Phys. Rev. A **63**, 043813 (2001).

[96] F. Renzoni and E. Arimondo, Phys. Rev. A **58**, 4717 (1998).

[97] A. Wojciechowski, E. Corsini, J. Zachorowski, and W. Gawlik, Phys. Rev. A **81**, 053420 (2010).

[98] M. Koschorreck, M. Napolitano, B. Dubost, and M. W. Mitchell, Phys. Rev. Lett. **104**, 093602 (2010).

[99] Y. Stauffer, Master's thesis, Ecole Polytechnique Fédérale de Lausanne (2004).

[100] U. Tietze and C. Schenk, *Electronic Circuits:Design and Applications* (Springer-Verlag, 1991).